

UTRECHT UNIVERSITY

MASTER'S THESIS

The Properties and Behaviour of Aeolian Streamers

in a narrow sandy beach-dune system

Author:

Jorn BOSMA, BSc

Supervisors:

Prof. dr. Gerben RUESSINK

Dr. ir. Geert STERK



Faculty of Geosciences
Department of Physical Geography
Earth Surface and Water

May 28, 2020

*“Here about the beach I wandered, nourishing a youth sublime.
With the fairy tales of science, and the long result of Time.”*

Lord Alfred Tennyson

UTRECHT UNIVERSITY

Abstract

Faculty of Geosciences
Department of Physical Geography

Master of Science

The Properties and Behaviour of Aeolian Streamers

by Jorn BOSMA

More accurate modelling of aeolian sediment transport in coastal environments is crucial to improving the planning and efficiency around soft coastal protection measures, such as sand nourishments, and a full understanding of the underlying transport mode is key to achieving it. This study aims to contribute to that widely shared purpose by trying to crack the code of the highly dynamically complex aeolian sand streamers. A wide range of different aspects of streamers have been investigated by exploiting at least as wide a range of different both qualitative and quantitative analytical techniques. Amongst others, this report presents a series of spatiotemporal saltation transport maps as well as one of the first known applications of the non-globalised wavelet transform to time series of transport intensity. In October 2017, saltation intensity records were collected at the beach nearby the Dutch town of Egmond aan Zee using three replicas of the newly developed Saltation Detection System (SDS), while co-located ultrasonic anemometers provided synchronised records of 3-D wind measurements. In addition, time-averaged water levels were measured just off the beach and in two cases surface moisture levels were monitored along a transect parallel to the wind field upwind of the SDS. Four sequential streamer patterns were recognised under intensifying transport conditions, in which spatiotemporal variability in saltation intensity is systematically reduced. Individual streamers were found to have a typical head-tail structure, coming up quickly, then slowly dwindle. High-intensity streamers were found having lengths of up to 0.5 m, widths of the order of 0.2 m and centre-to-centre spacings of up to 0.5 m. Neither shear velocity nor turbulence kinetic energy provide deterministic relationships for saltation intensity, but a clear, strong response is recognised of saltation intensity to increasing shear velocity. Coupling between the latter two variables is evident on temporal scales of the order of tens of seconds to minutes, which reflects the sizes of the turbulent eddies associated with streamer formation. Surface moisture greatly inhibits streamer formation if the moisture threshold is exceeded, but given that shear velocities are high enough, just a 10-m length of beach with (slightly) below-threshold moisture levels is sufficient for streamer formation to rapidly recover. Most (intense) streamers were seen on the mid beach, with less forming higher up the beach until some distance close to the dune foot, from where an opposite downwind trend was observed. The SDS was instrumental in gaining a better understanding of the saltation system on narrow beaches under all sorts of circumstances, but really comes into its own in low-energetic environments and under fair-weather conditions. The results of this study can hopefully be used as one more step towards unravelling the mysteries behind streamers, and finding the best methods and analytical techniques for future research to achieve this.

Acknowledgements

First, I kindly thank my supervisor Gerben Ruessink for giving me the opportunity to join his research project. The constructive feedback he provided on a regular basis was also greatly appreciated, as well as his seemingly limitless patience. I also wish to thank my temporary supervisor Jasper Donker for the occasional support in the field, and for sharing his expertise in data processing within the MATLAB environment and his thoughts on some of the results. Geert Sterk is much obliged for his willingness to take on the role of the second supervisor at the last minute. I am grateful to my fellow colleagues in the field, Corinne, Job and Jorn T., with whom I had the pleasure of spending a wonderful and productive time back in Egmond aan Zee. That special period in my studies has left me with very fond memories. I wish to express my gratitude towards the technical team, Arjan van Eijk, Bas van Dam, Marcel van Maarseveen and Mark Eijkelboom, for their assistance in getting all the instruments up and running and also keeping them that way. In particular, I want to acknowledge Bas for his part in the design and construction of the Saltation Detection System and providing me with technical support along the way. Last but not least, thank you, my dear parents, Joni and friends for all of your support and patience over the past years.

Contents

Abstract	iii
Acknowledgements	v
1 Introduction	1
2 Background	3
2.1 Aeolian transport	3
2.1.1 Transport modes	3
2.1.2 Fetch effect	3
2.1.3 Internal boundary layer	4
2.1.4 Moisture effect	5
2.1.5 Aeolian sand streamers	6
2.1.6 Wind forcing	9
Wind turbulence	9
Quadrant analysis	9
Coherent flow structures	11
2.2 Problem description	13
2.2.1 Objective	15
2.2.2 Research questions	15
Hypotheses	15
3 Methods	17
3.1 Site description	17
3.1.1 Morphology	17
3.1.2 Wind and wave climate	17
3.2 Instruments	18
3.2.1 Saltation detection system	19
3.2.2 Ultrasonic anemometer	21
3.2.3 Additional instruments	21
3.3 Data collection	22
3.3.1 Field preparations	22
3.3.2 Saltation and wind data	22
Streamwise set-ups	22
Threshold conditions	23
3.3.3 Soil moisture data	23
3.4 Data preparation	27
3.4.1 Sticky sand	27
3.4.2 Impact sensor malfunctioning	27
3.4.3 Counter box malfunctioning	27
3.4.4 Impact sensor saturation	28
3.5 Formulae and expressions	29
3.5.1 Saltation data	29

Temporal mean	29
Temporal variability	30
Spanwise mean	30
Spanwise variability	31
3.5.2 Wind data	31
Coordinate-system transformation	31
Data smoothing	32
Wind speed and direction	32
Shear velocity	33
Turbulence kinetic energy	33
3.6 Data analysis	33
3.6.1 Transport contour maps	33
3.6.2 Wavelet transform	34
3.6.3 Spanwise variability	35
4 Results	37
4.1 Contour maps	37
4.1.1 Transport patterns	37
Threshold transport	38
Dwindling character	38
Light transport	38
Moderate transport	39
Heavy transport	39
Streamer length scales	40
4.1.2 Saltation and airflow coupling	48
4.2 Wavelet transform	50
4.2.1 Short timescale	50
4.2.2 Long timescale	51
4.3 Trend analysis	55
4.3.1 Conditional statements	55
Incident wind angle	55
Time-averaged water level	55
4.3.2 Saltation and shear velocity	56
Regression analysis	57
Threshold shear velocity	58
4.3.3 Saltation and turbulence	59
Threshold turbulence	60
4.3.4 Spatiotemporal variability	60
Spanwise variability	62
4.3.5 Fetch and surface moisture	63
Fetch	63
Surface moisture	65
5 Discussion	69
5.1 Mapped streamers	69
5.2 Streamers and wind	71
5.3 Streamers and variability	72
5.4 Streamers across the beach	73
5.5 Saltation detection systems	75

6 Conclusion	77
Recommendations	78
A Supplementary figures	79
B Supplementary tables	85
C Supplementary theory	87
C.1 Wavelet theory	87
C.1.1 Continuous wavelet transform	87
C.1.2 Mother wavelet function	88
C.1.3 Wavelet coherence	88
C.1.4 Cone of influence	89
Bibliography	91

List of Figures

1.1 Aeolian streamers on a beach	2
2.1 Sediment transport modes	3
2.2 Fetch terms overview	4
2.3 Internal boundary layer	5
2.4 Streamer patterns	6
2.5 Contour plots of normalised saltation intensity (Safires)	7
2.6 Internal velocity deviations	8
2.7 Spanwise variability in saltation intensity	8
2.8 Quadrant plot	10
2.9 Burst-sweep mechanism	11
2.10 High Reynolds-number boundary layer	12
2.11 Global wavelet power spectra	13
3.1 Study site	18
3.2 IJmuiden wind rose	19
3.3 Instrument set-up	20
3.4 On-site wind rose	24
3.5 IJmuiden wind data	25
3.6 Deployment map of the 11 th and 27 th	26
3.7 Sensor-wiping procedure	27
3.8 Counter box error	28
3.9 Yaw-pitch-roll transformation	31
4.1 Visual determination of streamer velocity	41
4.2 Contour maps, 6 th , 12:54:47 - 12:54:53 MET (streamer dwindling)	42
4.3 Contour maps, 17 th , 13:53:08 - 13:53:14 MET (threshold transport)	43
4.4 Contour maps, 30 th , 16:27:25 - 16:27:30 MET (light transport)	44
4.5 Contour maps, 30 th , 15:02:49 - 15:02:54 MET (moderate transport)	45
4.6 Contour maps, 11 th , 12:52:42 - 12:52:48 MET (heavy transport)	46
4.7 Contour maps, 11 th , 12:44:46 - 12:44:50 MET (detrended)	47
4.8 Contour maps & u , 29 th , 14:08:48 - 14:09:48 MET	49
4.9 CWT (I & u), 29 th , 14:08:58 - 14:09:38 MET	52
4.10 WTC (I & u), 29 th , 14:08:58 - 14:09:38 MET	53
4.11 WTC (I & u), 17 th , 13:23:08 - 14:23:08 MET	54
4.12 $\bar{\mu}_y$ v. u_* (10-min)	56
4.13 $\bar{\mu}_y$ v. u_* (10-min) \Rightarrow regression	57
4.14 $\bar{\mu}_y$ v. u_* (1-min) \Rightarrow u_{*t}	58
4.15 CV v. k (1-s, 1-min, 10-min, 30-min)	59
4.16 CV & CV_y v. k & u_* (10-min)	61
4.17 CV_y v. Δy & u_* (10-min) \Rightarrow regression	62
4.18 $\bar{\mu}_y$ v. u_* (1-min) \Rightarrow fetch	64
4.19 Soil moisture profiles	67

4.20 $\bar{\mu}_y$ & u_* & ζ_{tide} (smoothed)	67
A.1 Sensor sensitivity	79
A.2 Vertical saltation profile	79
A.3 Grain-size distribution	80
A.4 Roughness length	80
A.5 Contour maps, 4 th , 11:36:39 - 11:36:45 MET (light transport)	81
A.6 Contour maps, 4 th , 13:07:26 - 13:07:32 MET (impact overload)	82
A.7 CWT (I & u), 17 th , 13:23:08 - 14:23:08 MET	83

List of Tables

3.1 Deployment overview	24
3.2 Overview of proportions unreliable data	29
B.1 Correlation coefficient (μ_y and u)	85
B.2 Correlation coefficient ($\mu_{p=5:9}$ and k)	85

List of Abbreviations

CI	Confidence Interval
CoI	Cone of Influence
CPD	Coherence Phase Difference
CWT	Continuous Wavelet Transform
KNMI	Koninklijk Nederlands Meteorologisch Instituut
LiDAR	Light Detection And Ranging
TKE	Turbulence Kinetic Energy
MSL	Mean Sea Level
MWAC	Modified Wilson and Cook
NAP	Normaal Amsterdams Pijl
OSSI	Ocean Sensor System, Inc. Wave Gauge
RD	Rijksdriehoek Coordinate System
RTK-GPS	Real Time Kinematic - Global Positioning System
UA	Ultrasonic Anemometer
Safire	Saltation flux impact responder
SDS	Saltation Detection System
WTC	Wavelet Transform Coherence
XWT	Cross (X) Wavelet Transform

Physical Constants

Gravitational acceleration	$g = 9.81 \text{ m s}^{-2}$
Mass-median diameter	$D_{50} = 227 \mu\text{m}$
Roughness length	$z_0 = 1 \times 10^{-3} \text{ m}$
Von Kármán constant	$\kappa = 0.40$

List of Symbols

a	wavelet scale	
b	wavelet translation	
$C(a, b)$	CWT coefficient	
$C_{xy}(a, b)$	XWT coefficient	
CV	coefficient of variation (temporal)	%
CV_y	coefficient of variation (spanwise)	%
CV_k	coefficient of variation (wind speed)	%
d_x	cross-shore distance	m
F	fetch	m
F_c	critical fetch	m
F_m	maximum potential fetch	m
I	instantaneous saltation intensity	cnts s ⁻¹
k	turbulence kinetic energy	m ² s ⁻² (J kg ⁻¹)
$R^2(a, b)$	magnitude-squared coherence	
T	air temperature	°C
u	streamwise velocity component	m s ⁻¹
u_*	shear velocity	m s ⁻¹
U	3-D wind speed	m s ⁻¹
v	streamwise-perpendicular velocity component	m s ⁻¹
w	vertical (wall-normal) velocity component	m s ⁻¹
x	streamwise axis	
y	spanwise axis	
z	vertical (wall-normal) axis	
α	wind incidence angle	° relative to shore normal
ζ_{tide}	time-averaged water level	m +NAP
η	tidal elevation	m +NAP
θ	wind direction	° clockwise from due north
θ_g	gravimetric soil moisture content	%
λ	wavelet pseudo-period	s
μ	time-averaged saltation intensity (1 sensor)	cnts s ⁻¹
μ_y	spanwise-averaged saltation intensity	cnts s ⁻¹
σ	temporal variability in saltation intensity	cnts s ⁻¹
σ_y	spanwise variability in saltation intensity	cnts s ⁻¹
τ_{xz}	Reynolds stress on x - z plane	N m ⁻²
$\phi(a, b)$	coherence phase difference	rad
var'	fluctuating, turbulent part of var	
\bar{var}	temporal mean of var	

1 Introduction

It is common knowledge that the world's densest populated areas are always found in the vicinity of rivers and coasts. In many occasions living in such environments brings along certain hazards that require adaptation in the form of protective measures against flooding and other suchlike issues (e.g., erosion and salt intrusion). Good examples of such measures are found in the low-lying provinces of the Netherlands, where large man-made structures, such as sea dykes and the so-called Delta Works, secure the land from natural threats from the adjacent North Sea. Besides these 'hard' coastal structures, also naturally occurring 'soft' morphological features help guarantee the safety of the country's citizens and agricultural land, most notably in the form of tall, elongated, usually partly vegetated ridges of sand that are found along the coastline. These dunes form a natural barrier between the North Sea and the hinterland and prove their usefulness especially in cases of extreme high water during storm surges. Furthermore, they also provide a source for drinking-water withdrawal and serve various recreational purposes (Luijendijk et al., 2017).

In the course of the past decades, people's appreciation of the more dynamic natural barriers and their advantages began exceeding that of their fixed man-made counterparts. This shift in way of thinking encouraged new research into the properties and evolution of these precious landscape features. Since the survival of the Dutch dunes cannot be taken for granted in times of climate change, knowledge of any factors contributing to their growth or decline, could be useful. Our current situation, with eyes on the accelerated sea-level rise due to enhanced global warming, only amplifies the need for improved insights.

One way in which the Dutch have tried to stimulate both local and regional dune growth is by means of sand nourishments (Kabat et al., 2009), which allow natural build-up of the adjacent beach-dune system through wave-driven accretion and wind transport, thereby minimising human interference. However, little is known about how to exactly quantify and model the transport of sediment from the place of nourishment towards the foredune, complicating the planning and decision making around such operations and compromising their very purpose. It is the complexity of the inter-relationships of all the different components involved (i.e., beach geometry, surface controls and flow forcing) that make this topic hard to fully comprehend. The best way of getting to understand the bigger picture is by dividing it up into smaller researchable bits. Accordingly, in this study the focus is upon one specific aspect of aeolian (i.e., wind-driven) sediment transport across beaches, that is vital to the preservation and growth of the (fore)dunes.

The patterns of such transport as it occurs in natural environments are typically complex and unpredictable. Rather than moving as a uniform sheet over the beach's surface, the transported sand is concentrated in semi-individual, elongated structures that also irregularly meander while advancing (Gares et al., 1996). Because traditional transport models do not fully respect the spatiotemporally variable nature of these moving sand patterns, commonly referred to as aeolian streamers (see Fig. 1.1), they generally tend to overpredict the actual transport rates. However, as both

cost efficiency and environmental protection are highly valued targets in today's society, there is a demand for models that *do* get it right. Successful incorporation of aeolian-streamers dynamics into transport models, albeit simplified to some degree, is key to this and can only be achieved through improved understanding of their formation and behaviour, which underlie the dynamics of the saltation system (Baas and Sherman, 2005).

This thesis is structured as follows: the second chapter provides a comprehensive literature review addressing all important details about what is currently known and unknown about streamers and the saltation system in general, and concludes with the formulation of the research objective and questions resulting therefrom. The following chapter describes the framework of this study by giving details about the four-week fieldwork undertaken near Egmond aan Zee in autumn 2017 and the subsequent handling of the data collected. Moving on, the reader finds three more chapters covering the results, discussion and conclusions, in that order, while any supplementary figures and tables are found in the appendices. This study presents and discusses the results from a combination of relatively new analysis techniques and state-of-the-art measuring devices to provide new insights into the nature of aeolian streamers.



FIGURE 1.1: Contrast-enhanced photograph featuring aeolian sand streamers propagating towards the observer. Location: beach near Egmond aan Zee, the Netherlands.

2 Background

2.1 Aeolian transport

Within the various fields of earth science all processes pertaining to wind activity are indicated by the adjective 'aeolian', derived from the Greek mythical character *Aeolus, Keeper of Winds*. Thus, we speak of aeolian sediment transport when induced by some wind-related force. Transport of sediment through fluid forcing is a topic that has been thoroughly explored, both in laboratories and in the field, on a wide range of scales. Nonetheless, even though the concept may be rather simple, the physics underlying aeolian sediment transport are so complex that only in very rare cases some of the widely accepted equilibrium theories truly apply (Bauer et al., 2009). The more complex the sediment transport system, the more likely that the predicted transport rates deviate from the observed rates. A wide range of factors gives rise to this degree of complexity, amongst which inherently complex phenomena such as turbulence, and landscape factors such as the length of erodible surface and the moisture content of the surface layer.

2.1.1 Transport modes

In beach-dune systems there are different modes of aeolian transport possible, all of which may occur locally in the presence of a supply of (loose) granular material in conjunction with wind-induced shear stresses high enough to uplift and entrain some of these grains (Kok et al., 2012). Particles within the appropriate range of sizes may then participate in a short-term suspension, which is referred to as saltation, the dominant mode of transport. Too small ($\lesssim 20 \mu\text{m}$) and they may instead enter a long-term suspension (Gillette and Walker, 1977). By contrast, particles too big ($\gtrsim 500 \mu\text{m}$) may only do a very short hop, known as 'reptation' (Ellis and Sherman, 2013), or roll along the surface for some distance, called 'creep' (Bagnold, 1936). Figure 2.1 gives a schematic overview of these four modes of transport. Note that the latter three modes (i.e., suspension, reptation and creep) do not fall within the scope of this study.

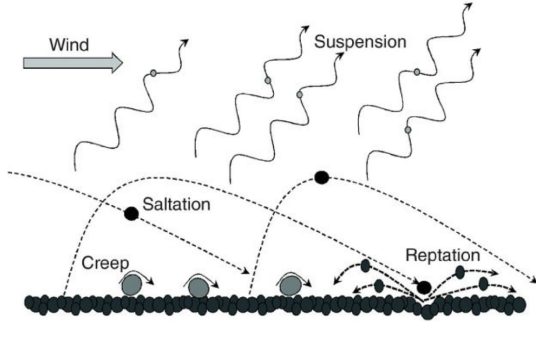


FIGURE 2.1: Schematic of the four modes of sediment transport. Extracted from Livingstone and Warren (2019).

2.1.2 Fetch effect

As airborne particles loose buoyancy and eventually impact the surface bed, they have the potential of dislodging multiple additional particles by transferring part

of their momentum. This mechanism can go on for a considerable downwind distance and is commonly referred to as 'avalanching' (Chepil, 1957) or the 'saltation cascade' (e.g., Bauer et al., 2009). Given that environmental conditions are ideal and sediment supply is unlimited, such a process would lead to an endless exponential increase in transport rate with downwind distance, were it not that each aeolian transport system has a point of saturation, at which the wind simply cannot carry more sediment (e.g., De Vries et al., 2014). This capacity is chiefly a function of wind speed, sediment grain size and moisture content (Bauer and Davidson-Arnott, 2003). However, before that point is reached, the increase in transport rate also effectively increases the aerodynamic roughness of the surface layer (Gillette et al., 1996), which in turn facilitates transport by enhancing the momentum transfer from the saltating particles back to the surface. This feedback mechanism is termed the 'Owen effect' (Gillette, Hardebeck, and Parker, 1997) and, together with the avalanche mechanism, forms the basis of the 'fetch effect' (Anthony, 2008), where fetch (also fetch distance or length) stands for the length of erodible surface over which the wind exerts a shearing force.

Beach geometry (W, L) and wind incidence angle (α) are important factors controlling the fetch effect (Fig. 2.2), as they determine the fetch (F) (Delgado-Fernandez, 2010). On beaches, oblique winds naturally give rise to longer fetches than do cross-shore winds, while the fetch can be considered infinite for perfectly alongshore winds. The maximum potential fetch (F_m) on a beach is the total distance from the leading sand edge (i.e., upwind boundary) to the dune line parallel to the wind. By contrast, the critical fetch (F_c) is the minimum distance necessary for the sediment transport system to achieve equilibrium (or saturation) and is predominantly controlled by the capacity of the wind to entrain sediment (Bauer and Davidson-Arnott, 2003). The limited transport capacity of the wind, which depends on its velocity, is usually also responsible for the stagnation of the initial rapid increase in sediment flux (Delgado-Fernandez, 2010, & references therein). Beyond the critical fetch, sediment transport rates tend to stabilise, which is why the process behind its establishment is often referred to as a self-balancing mechanism. However, downwind modification of the near-surface airflow (see 2.1.3) often reduces the wind's capacity to transport sediment, making a constant equilibrium (or steady) state unlikely (Bauer et al., 2009).

2.1.3 Internal boundary layer

Where fetch generally has a transport facilitating effect, a closely connected, often synchronous process counteracts this. Change of surface properties, such as roughness (e.g., during rising transport intensities), moisture content or temperature along the flow path of air, gives rise to a layer of modified airflow downwind of the discontinuity (x_0 in Fig. 2.1.3) (Garratt, 1990), which has also been observed immediately

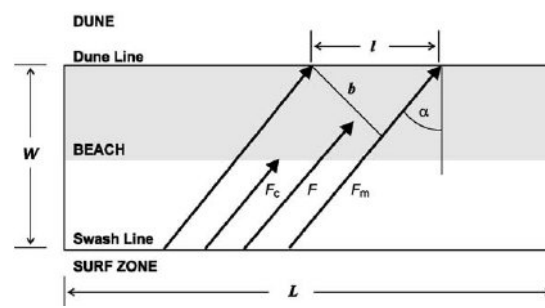


FIGURE 2.2: Schematic of beach-dune system $W \times L$ with the fetch terms discussed in the text. F is the actual fetch at a given point, while the subscripts c and m denote the critical and maximum fetch, respectively. Furthermore, α is the wind incidence angle relative to shore normal and l is an alongshore distance, so that $b = l \cos \alpha$. Copied from Bauer and Davidson-Arnott (2003).

downwind of the ocean-beach transition (Bauer et al., 1990). Such a transitional layer, termed an aerodynamic internal boundary layer (IBL), is bound to the surface and tries to adapt its new properties. Downwind vertical expansion of the IBL causes thinning of the total shear stress distribution, resulting in diminishing transport competency of the airflow from the foreshore towards the foredune (Bauer et al., 2009).

Due to the implications its development has on near-surface transport competency of the wind and the eddies advancing through (Hunt and Morrison, 2000), it may play an important role in the process of saltation, hence streamers. In fact, Baas and Sherman (2006) already suggested the possibility of a relation between spanwise transport variability and the IBL, through turbulent eddies that scale with the product of the local IBL depth and the Von Kármán constant (Stull, 1988).

The depth of the IBL (δ_i in Fig. 2.1.3) tends to increase with downwind distance and can be approximated by solving the following model from Panofsky and Dutton (1984):

$$\frac{\delta_i}{x} \left[\ln \frac{\delta_i}{z_0} - 1 \right] = B\kappa \quad (2.1)$$

where δ_i is the IBL depth (m), x the fetch (m), z_0 the roughness length (m), κ the Von Kármán constant and $B = 1.25$. Care must be exercised when choosing the value for z_0 , since under transport conditions the effective surface roughness may easily increase by an order of magnitude (Hsu, 1971; Sherman, 1992) as the result of the aforementioned Owen effect (see 2.1.2).

2.1.4 Moisture effect

Moisture stored inside the top layer of a soil may strongly modify the soil's susceptibility to entrainment through wind shear by strengthening the cohesive forces acting between the particles (Chepil, 1958). This so-called 'moisture effect' generally causes substantial reduction of transport or may even lead to a total shutdown when raising the entrainment threshold velocity sufficiently (Arens, 1996; Bauer et al., 2009). A commonly proposed threshold of (gravimetric) moisture content, above which transport ceases, is 10 % (e.g., Davidson-Arnott et al., 2005). However, besides the considerable uncertainty in this threshold value, it is also not yet clear how values below this threshold affect transport rates (Delgado-Fernandez and Davidson-Arnott, 2011).

Environmental factors controlling local moisture levels on a beach include precipitation, humidity, wave run-up and the groundwater table. Whereas tides and waves are evidently most significant on the foreshore, atmospheric humidity and rainfall (or other forms of precipitation) are generally more important factors on the backshore (Bauer et al., 2009). In the case of rainfall, Van Dijk, Stroosnijder, and De Lima (1996) found that the primary effect of soil moisture may be overcome through the transfer of momentum from raindrops at the moment of impact on the beach

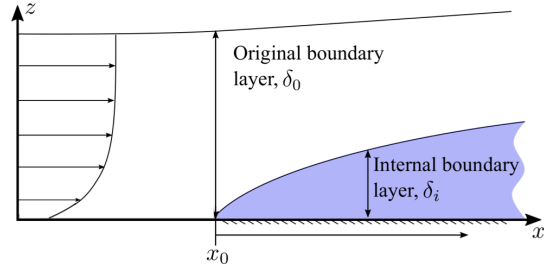


FIGURE 2.3: Schematic of a developing internal boundary layer depth (δ_i) over fetch x starting from the sea-beach transition (x_0). On the left side a logarithmic wind profile inside the original boundary layer (δ_0). Adapted from Mogeng et al. (2018).

surface. This can cause surface grains to violently dislodge based on the same principle as the saltation cascade, and is ultimately expressed in an *increase* in transport rate. Moreover, raindrop impacts may also cause the ejected (saltating) particles to travel higher and farther than they would have under typical dry conditions (Erpul, Norton, and Gabriels, 2002). Nonetheless, such transport enhancing effects generally last only a short period of time, after which the surface sand quickly becomes too wet and cohesive (Arens, 1996).

2.1.5 Aeolian sand streamers

On beaches saltation is commonly observed as highly intermittent, snake-like features (see Fig. 1.1) advancing in a streamwise fashion (i.e., in the mean direction of the wind shear) (e.g., Gares et al., 1996), while also shifting laterally (e.g., Baas and Sherman, 2005). These so-called '(aeolian) streamers' are the display of complex and dynamic transport patterns that are found to vary in both time and space on scales of 0.1 s and 0.1-1 m (spanwise; wind-normal), respectively (Baas, 2008). Such spatiotemporal dynamics could explain spatial variations in transport rate commonly observed in field studies. For example, Gares et al. (1996) acquired from an along-shore set-up of vertical sand traps, spatial variations in transport rate ranging from 20 % (0–5 m) to 45 % (0–50 m) about the mean, which they attributed to the irregularity of streamers across the beach. Traditional aeolian saltation transport models do not encapsulate the spatiotemporally variable nature of the aeolian-streamer phenomenon and tend to oversimplify the overall transport mechanism to a temporally steady and spatially uniform saltation sheet (Baas, 2008), and being a deterministic function of the time-averaged shear velocity (see 3.19). This approach usually leads to substantial discrepancies between predicted transport rates and those observed in the field (Ellis et al., 2012), as the intermittent character of streamer transport effectively reduces the amount of time over which transport takes place (Davidson-Arnott and Bauer, 2009).

Probably the most extensive past research on aeolian streamers was conducted by Baas (2003) and elaborated in a series of subsequent papers. He monitored the saltation fluxes with a sampling frequency of 20 Hz at two different field sites in California, USA, on top of a coastal sand dune (Guadalupe) and an arid sand mound (Windy Point), using horizontal wind-normal arrays of saltation flux impact responders (Safires). In a case study in which streamers were observed over a homogenised surface, he found that bed surface control (e.g., differentiation in moisture content, grain size, or microtopography) does not play a crucial role in the formation of streamers. However, he did recognise that the properties of streamers may vary from site to site, depending on the amount, distribution and properties of the erodible material at the surface.

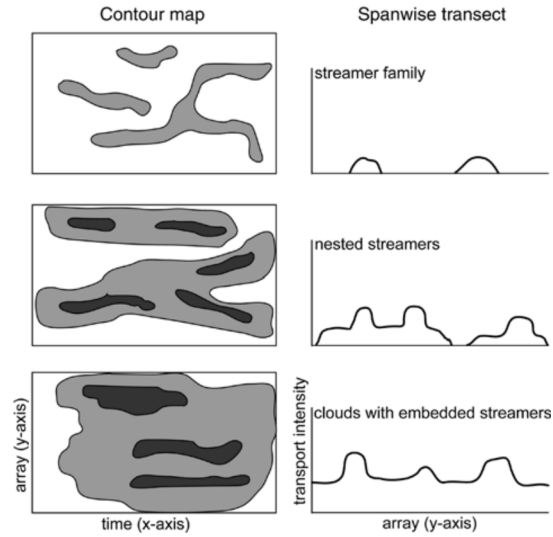


FIGURE 2.4: Schematic of streamer pattern characteristics. Areas (left) represent low-intensity base-level clusters (grey) and more intense nested or embedded clusters (black). Copied from Baas and Sherman (2005).

Baas and Sherman (2005) produced contour maps from the Safire data from the Windy Point experiment (see examples in Fig. 2.5) in an attempt to reveal streamer dimensions and behaviour. They distinguished three mutually exclusive, though non-exhaustive, saltation transport patterns on a qualitative basis: streamer families, nested streamers and clouds with embedded streamers (Figs. 2.4 and 2.5), respectively occurring under low-, intermediate- and high-intensity transport conditions. They computed a series of statistics on two relatively short (\sim 15-min) measurement runs at Windy Point, focusing on the occurrence of saltation clusters, which were defined as adjacent arrays of at least two Safires measuring transport. From the low correlations between the number and width of embedded clusters (identified as streamers) and the different types of transport intensity (i.e., (1) average over the Safire array, (2) base-level spanwise cluster and (3) average embedded cluster) they concluded that streamers have an independent and consistent size and mutual spacing. These (relatively intense) clusters were found to have a mean width of 0.12 m (at 0.04 m above the bed) and on average occur 0.9 times per lateral (or spanwise) metre. In addition, a time-lag analysis on the time series of a co-located streamwise orientated array of Safires revealed the saltation-clouds to propagate on average with a velocity of $3.6 \pm 2.5 \text{ m s}^{-1}$ ($R = 0.68$).

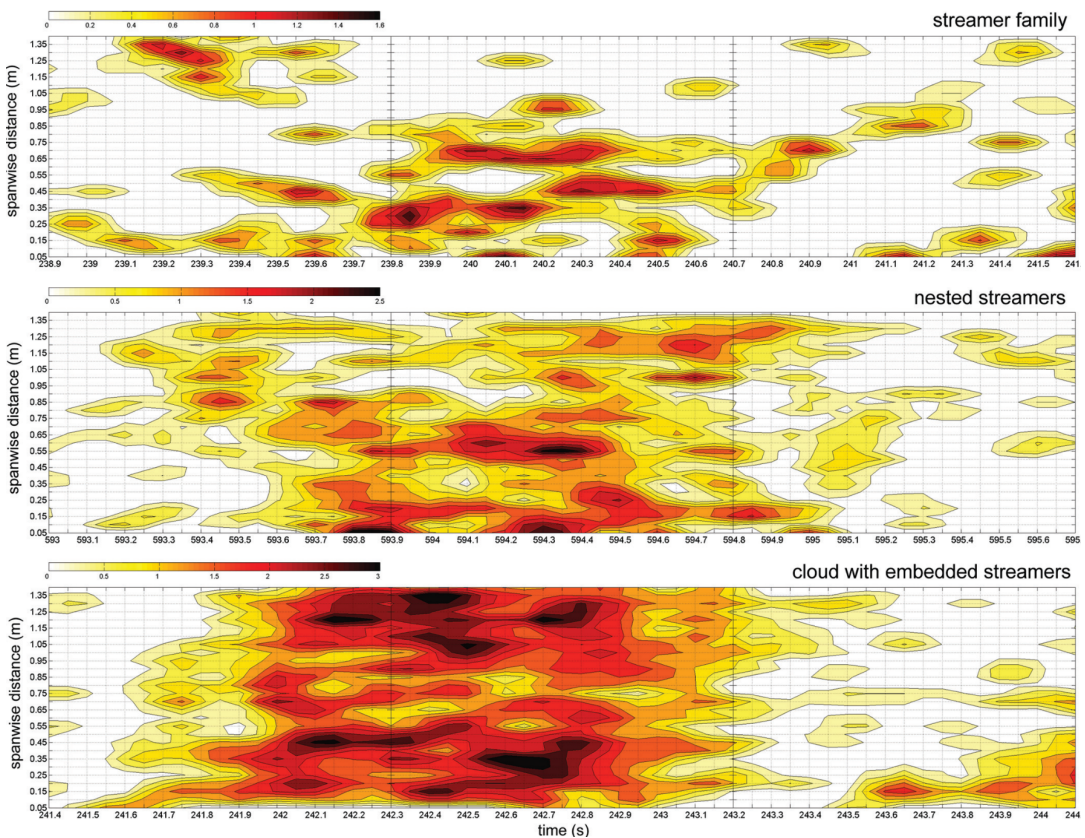


FIGURE 2.5: Contour plots (smoothed) of normalised saltation intensity acquired from a wind-normal array of 29 Safires with a mutual spacing of 0.05 m and measuring at 0.04 m from the bed. Top, middle and bottom panels display different streamer patterns that occur under low-, intermediate- and high-intensity transport conditions, respectively. Copied from Baas and Sherman (2005).

The fact that streamers are ever undulating transport phenomena, which intertwine, merge and split apart at the same time, make them hard to successfully and truthfully capture with a Eulerian approach (Sherman et al., 2013). A fundamental assumption in the creation of these transport contour maps is Taylor's frozen turbulence hypothesis (Taylor, 1938). In the field, streamers are actually observed to change shape over relatively short timescales, which is an indication of varying internal migration speeds across the pattern itself (conceptualised in Fig. 2.6), compromising the hypothesis to at least some extent.

In contrast to the study by Baas (2003), which relied on Eulerian measurements, a later study by Sherman et al. (2013) used a more Lagrangian-based approach by conducting time-exposure videography on the foreshore of a beach near Jericoacoara, Ceará, Brazil. Their preliminary results revealed typical flow-parallel length scales of streamers to be on the order of 10s of metres, centre-to-centre spacings from 0.6 to 1 m and gaps between individual streamers of approximately 0.2 m. Despite the different environmental settings (i.e., intertidal sand flat v. arid sand mound), these results are in line with results and observations in Baas and Sherman (2005).

Baas and Sherman (2006) also examined the effect of sand movement in streamer patterns, as illustrated in Fig. 2.5, on the spatial variability in saltation intensity. They used the Safire data from the Guadalupe experiment (7x 15-min measurement runs on a coastal sand dune) to generate the graphs shown in Fig. 2.7. Coefficients of variation (or relative standard deviations) were computed over all Safires contained within lateral (or spanwise) distances ranging from 0.1 to 4.0 m with 0.1-m increments. This procedure was carried out for multiple time-averaging periods of the data set ranging from 1 to 120 s. They found that the average variability in saltation intensity ranged from 29 % for the smallest spanwise and largest temporal scale to 266 % for the largest spanwise and smallest temporal scale, while variability also seemed to stabilise beyond a distance of roughly 3 m for most time-averaging periods (Fig. 2.7). Ellis et al. (2012) found values of similar order of magnitude using hose-style sand traps, and ascribed the decrease in variability with increasing sample duration and transport intensity to the streamers smoothing variability through lateral migration.

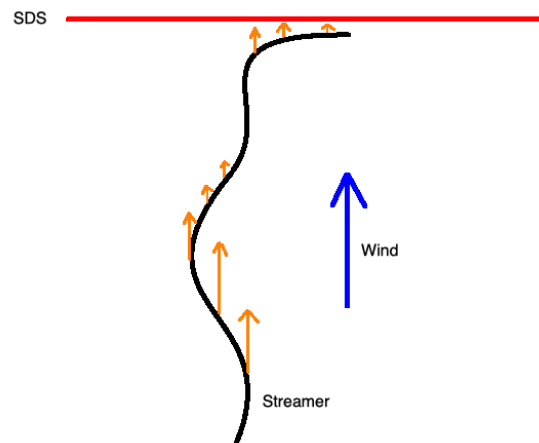


FIGURE 2.6: Schematic representation of internal variations in migration speed of a streamer, effectively compromising Taylor's hypothesis. Lengths of orange arrows denote the local velocity magnitude.

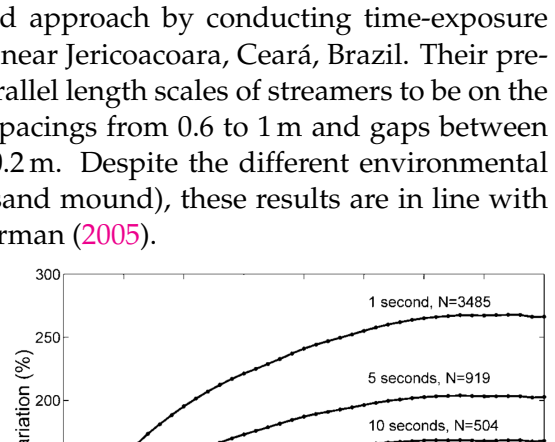


FIGURE 2.7: Coefficient of variation of saltation intensity as a function of spanwise scale for different averaging periods. N is the corresponding number of time averages involved. Copied from Baas and Sherman (2006).

These results again highlight the potential impact of streamer transport on the inherent error margins of many numerical saltation transport models that rely on extrapolation. Important to note, however, is that Baas and Sherman (2006) also recognised that the varying sensitivity thresholds among the Safires restricted the analysis to only cover grains with diameters greater than 4×10^{-4} m, thereby disregarding possibly deviating trends of finer fractions.

2.1.6 Wind forcing

The dependency of saltation mass flux on wind speed is commonly described as a 3rd-power relation, even though De Vries et al. (2014) found that under supply-limited conditions this dependency is more likely to be linear. Other factors controlling this dependency include variations in precipitation intensity, tide level and wind direction (Bauer et al., 2009), as they are related to the mechanisms described in 2.1.2 to 2.1.4. The latter two terms especially apply to narrow beaches, since in those cases the fetch typically fails to reach its critical value ($F_m < F_c$) for the majority of wind directions, hence does not allow maximum transport rates ever to be achieved (Delgado-Fernandez, 2010). All the same, Bauer et al. (2009) suggest that even if the critical fetch were exceeded, transport may, paradoxically, even decrease with downwind distance due to the development of an internal atmospheric boundary layer directly downwind of the sea-beach transition, as was explained in 2.1.3.

Wind turbulence

Wind forcing is neither uniform nor steady under natural conditions (Wyngaard, 1992), which is often reflected in transport variability (e.g., Bauer et al., 1998) manifested as, for instance, aeolian streamers (2.1.5). Even to date, turbulence remains a largely unsolved problem of classical physics because of its inherent complexity (Smits and Marusic, 2013). When in the vicinity of a solid confining surface featuring roughness elements (e.g., the beach) so-called wall-bounded turbulence becomes particularly complex. Yet, it is the physics within this near-wall region, where turbulent eddies might interact with the surface grains, that could be conclusive in solving the problem of streamer formation and behaviour.

As stated before, aeolian streamers are widely thought to arise from gusts associated with wind turbulence acting close to the bed (e.g., Baas and Sherman, 2005; Stout and Zobeck, 1997). Whenever the shearing force of air exceeds the threshold of motion (i.e., the point where surface grains can no longer resist the imposed forces), horizontal momentum is transferred and the grains become incorporated into the airflow (Leenders, Boxel, and Sterk, 2005). The momentum gained by individual saltating grains is contained even during airflow accelerations/decelerations, giving rise to saltation inertia (Spies, McEwan, and Butterfield, 2000; Mayaud et al., 2017). This behaviour appears most evident during velocity decelerations, as was demonstrated by wind-tunnel experiments by Butterfield (1993), which revealed that transport rates often lag 1–2 s behind velocity decelerations, whereas responding close to instantaneously to accelerations.

Quadrant analysis

In the past, multiple studies have tried to relate various turbulent flow signatures to sediment flux by means of the so-called quadrant-analysis technique (e.g., Sterk, Jacobs, and Van Boxel, 1998; Bauer et al., 1998; Schönfeldt and Löwes, 2003; Leenders,

Boxel, and Sterk, 2005; Wiggs and Weaver, 2012). This technique revolves around a quadrant chart, which is basically a scattergram divided into four equal quadrants (Fig. 2.8). First, the measured 3-D wind vector must be decomposed into its three orthogonal components:

$$\begin{aligned} u &= \bar{u} + u' \\ v &= \bar{v} + v' \\ w &= \bar{w} + w' \end{aligned} \quad (2.2)$$

where u , v and w are the streamwise, streamwise-perpendicular and vertical (wall-normal) velocity components, respectively, and the overbar and prime symbol respectively denote their mean and fluctuating part (with zero mean). By plotting u' and w' against each other, the contributions of each quadrant (i.e., velocity-fluctuation product) to the Reynolds stress ($\tau_{xz} = -\rho\bar{u}'\bar{w}'$, where ρ is the fluid density) or the kinematic stress (τ_{xz}/ρ) can be determined (Wallace, 2016). Each of the quadrants represents a distinct momentum-exchange structure: Q1 ($+u', +w'$), Q2 ($-u', +w'$), Q3 ($-u', -w'$), and Q4 ($+u', -w'$) described as 'outward interaction', 'burst/ejection', 'inward interaction' and 'sweep/gust', respectively, where both Q2 and Q4 contribute positively to the Reynolds stress generation by definition (Chapman et al., 2012). The majority of these studies also included a so-called 'Hole' (blue area in Fig. 2.8) in their quadrant plots, which is defined by the set of hyperbolas in each quadrant: $|u'w'| \geq H|\bar{u}'\bar{w}'|$, where $\bar{u}'\bar{w}'$ is the mean value of this product for a given distance from the wall and H a magnitude-filtering (threshold) parameter (Wallace, 2016). In those cases only the values outside the Hole were considered in the analysis as a way to dispose of background noise. Literature provides no fixed value for H , but an often picked threshold is one standard deviation of $\bar{u}'\bar{w}'$ (e.g., Sterk, Jacobs, and Van Boxel, 1998; Wiggs and Weaver, 2012; Leenders, Boxel, and Sterk, 2005).

Using this technique, Sterk, Jacobs, and Van Boxel (1998) found for two field experiments that Q2 motions contributed 39.7 % and 36.9 % of the total kinematic Reynolds stress, while Q4 motions contributed 61.5 % and 45.1 %, respectively. These findings are similar to those reported in Bauer et al. (1998), even though their measurement environment and instrumentation differed considerably. Furthermore, they both also found relatively small contributions of Q1 and Q3 motions, which were usually less than 15 %.

Sterk, Jacobs, and Van Boxel (1998) found no well-defined relationship between time series of instantaneous kinematic stress ($\bar{u}'\bar{w}'$) and sediment flux ($R < 0.15$). After having assigned all instantaneous saltation flux measurements to their corresponding quadrant signatures, it became clear that Q1 (outward interaction) and Q4 (sweep/gust) motions by far account for the largest mean saltation fluxes. It must be noted, however, that any conclusions about the corresponding kind of motion or event are based on the assumption that these quadrant signatures

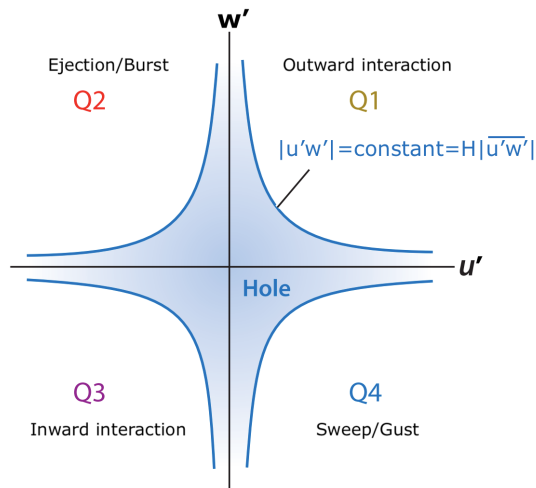


FIGURE 2.8: Quadrant plot for turbulent velocity fluctuations in the streamwise (u') and wall-normal (w') components of the wind vector. Adapted from Wallace (2016).

are indeed associated with coherent flow structures, even though that may not actually be the case (Bauer et al., 2013). Nonetheless, both these signatures have in common a positive u' (i.e., an instantaneous acceleration imposed on the mean horizontal wind velocity), which highlights its importance in provoking and sustaining saltation, hence streamer formation. Schönenfeldt and Löwes (2003) and Leenders, Boxel, and Sterk (2005) conducted similar analyses and came to the same conclusion that horizontal velocity fluctuations (u') are much more essential to the sediment flux than are vertical velocity fluctuations (w') or the kinematic stress. Yet, caution must be exercised with interpretations regarding the vertical velocity component, since most of these studies measured at several metres above the ground, thereby running the risk of capturing different eddies than the ones that are actually acting in the near-surface region (Boxel, Sterk, and Arens, 2004).

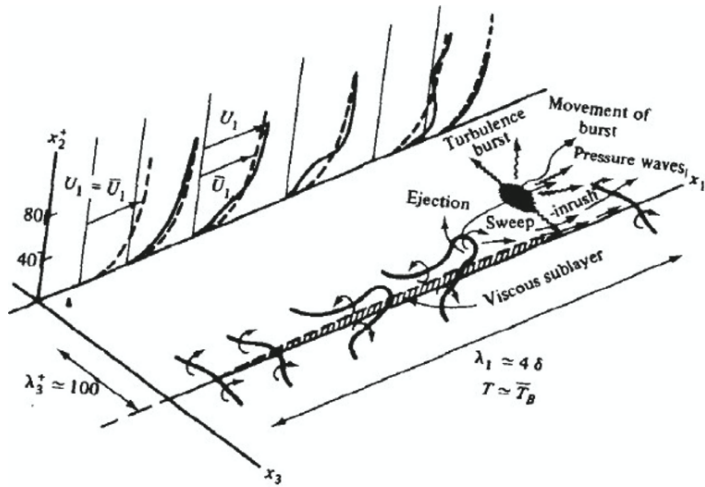


FIGURE 2.9: Schematic of the burst-sweep mechanism showing the topology of the evolving roller vortex and corresponding velocity profile down the centre line. Copied from Hinze (1975).

Coherent flow structures

It is a popular idea that the properties (and appearance) of saltation 'events' are governed by coherent flow structures embedded in the flow field of the wind (Bauer et al., 2013). As stated previously, there have been various types of turbulent flow structures associated with the generation of streamers, usually bottom-up mechanisms such as hairpin vortices shed by burst-sweep events (Fig. 2.9), which are sequences of the Q2 and Q4 motions in Fig. 2.8, or Taylor-Görtler vortices. However, to date no evident correlations have been found between structural (e.g., burst-sweep) events in winds across the beach and transport events (e.g., Bauer et al., 1998). In a more recent proposal, Baas and Sherman (2005) suggested a link between the initiation and intensification of saltation rates (in the form of streamers) and a top-down structure introduced by Hunt and Morrison (2000), in which down-sweeping eddies produce locally increased shear stresses as they skim the surface (see Fig. 2.10). The idea of large-scale eddying motions giving rise to the streamer topology by continuously exciting saltation in their wake (red outlined region in Fig. 2.10) while propagating downstream seems plausible, as it fits the time and space scales of streamers and is also supported by a recent model study by Wang et al. (2019).

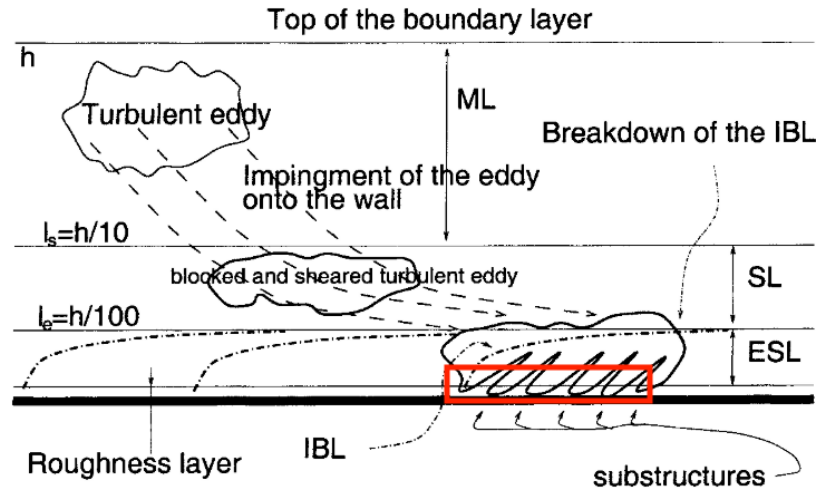


FIGURE 2.10: Schematic of a top-down structure in a boundary layer: a turbulent eddy from higher up travels downward and imposes a shearing force on the surface on impact and continues to do so while propagating in downwind direction. Red frame marks the region where streamers might be formed. Furthermore, $h = 1\text{--}2\text{ km}$, $l_s = 100\text{--}200\text{ m}$ and $l_e = 10\text{--}20\text{ m}$. Adapted from Hunt and Carlotti (2001).

In addition to the analyses discussed previously in 2.1.5, Baas (2006) analysed synchronous time series of saltation intensity (from Safires) and streamwise wind speed (from hot-film probes) using the wavelet transform technique. This technique offers a robust alternative to the traditional Fourier transform in cases of intermittent, non-Gaussian distributed time series (see Appx. C for a detailed description on its application). The produced global wavelet power spectra (Fig. 2.11a) show two peaks in the spectrum of streamwise wind speed at periods (read: 'event' durations) of about 60 s and 19 s, and a well-defined and less pronounced peak in the spectrum of saltation intensity at periods of about 6–7 s and 50 s, respectively. Furthermore, for periods shorter than about 0.4 s and between 0.9–2 s the respective spectra of streamwise wind speed and saltation intensity appear to trend toward a Kolmogorov inertial subrange ($T^{5/3}$ -slope), which is a possible reflection of the breakdown of dynamically unstable turbulent eddies into progressively smaller ones (Smits and Marusic, 2013). According to Baas (2006), the longest periods (60 s and 50 s) may be a reflection of the time-averaged wind shear in the IBL driving long-term sand transport, whereas the intermediate periods (19 s and 6–7 s) may be linked to gusts by some of the largest eddies in the IBL initiating relatively short episodes of saltation. In both cases he ascribed the duration discrepancies to the threshold shear velocity. Lastly, the shortest periods, say, of the order of 1 s and below, may reflect the formation of streamers by their individually associated eddies in the energy cascade. The now opposite duration discrepancy he attributed to saltation inertia. Baas (2006) only found strong correspondence between the wavelet power spectra of streamwise wind speed and saltation intensity (Fig. 2.11b) at periods longer than 60 s with an optimum lag of the order of seconds. For shorter periods correlation was clearly less evident.

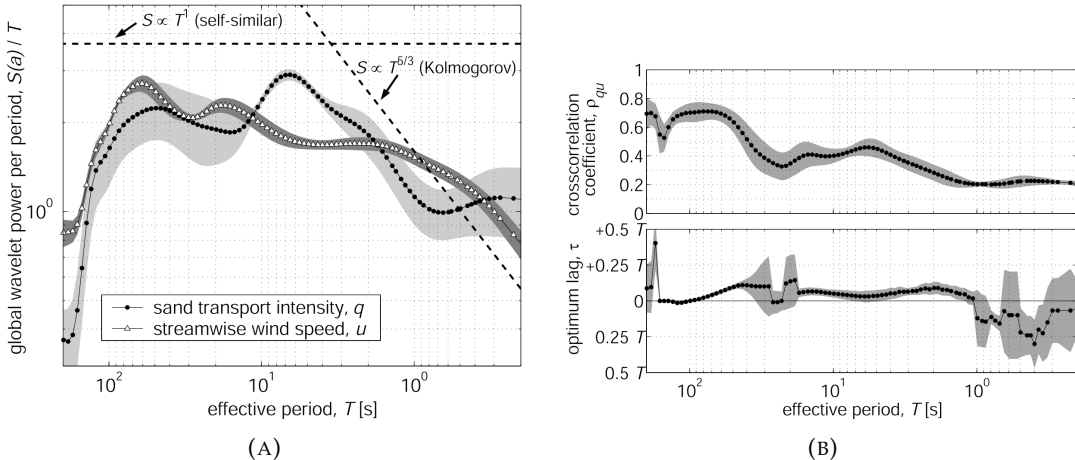


FIGURE 2.11: (A) Global wavelet power spectra of streamwise wind speed and saltation intensity and (B) maximum cross-correlation coefficient (top) at an optimum temporal lag (bottom) between the instantaneous wavelet transform power functions. Based on data from 6 co-located pairs of Safires and hot-film probes. Shaded areas indicate ± 1 standard deviation about the mean. Copied from Baas (2006).

2.2 Problem description

From the literature discussed above we now know that aeolian sand streamers are elongated patterns of continuously prompted saltation that account for much of the spatiotemporal variability in sediment transport in the field. Individual streamers typically have widths of tenths of metres, lengths of metres to tens of metres and spacings to adjacent streamers of the order of 1 m as seen from their centre lines. They are presumably the momentary footprints of large turbulent eddies (Fig. 2.10) that locally generate accelerations in surface-parallel wind velocity (i.e gusts) superimposed on the mean flow, thereby exceeding the entrainment threshold of the surface grains. Thus, these eddies travel downstream, leaving streamers in their wake once they ‘hit’ a mobile sandy surface. As flow (hence shear) velocities increase, it may take some time before surface grains are put into motion, as first the threshold shear velocity must be exceeded. Conversely, streamers may persist beyond the actual window of enhanced flow velocity due to saltation inertia. Furthermore, neither the instantaneous Reynolds nor kinematic stress have appeared suitable predictors of saltation rates, hence streamer intensity, whereas the horizontal wind speed *did*. Besides, no convincing evidence has been found as of yet associating (bottom-up) coherent structures such as hairpin vortices (Fig. 2.9) with fluid excursions and, therefore, saltation.

When it comes to investigating saltation characteristics, and particularly concerning aeolian streamers, there are many different factors that must be taken into consideration. Where this is already important for experiments conducted in a laboratory, which are relatively easy to control, it becomes even more relevant to studies based on field measurements. In order to gain valuable insights into streamer dynamics under purely natural conditions, one has to ideally obtain multiple high-frequency records of both saltation and airflow on a sufficient spatial resolution. The inherent challenges in collecting such data, however, are largely responsible for the low number of suchlike field studies as of yet (e.g., Baas and Sherman, 2005). For example, streamwise response of saltation to fluctuations in airflow is thought to be

of the order of 1 Hz. In addition to that, fluctuations at fixed points may also occur in the spanwise direction due to meandering (sideways migrating) behaviour of streamers, even further complicating matters.

In the past, already a number of different instrument set-ups have been deployed in the field with the capability of measuring saltation and airflow synchronously (e.g., Sterk, Jacobs, and Van Boxel, 1998; Schönenfeldt and Löwes, 2003; Leenders, Boxel, and Sterk, 2005), each with their own benefits and shortcomings. It can be assumed that in all cases an important trade-off had to be made between costs and quality, which obviously does not help in overcoming the accompanying challenges. Furthermore, at least as many different analysis techniques have been applied to this particular field of study; a popular example being the quadrant analysis technique (e.g., Sterk, Jacobs, and Van Boxel, 1998; Schönenfeldt and Löwes, 2003; Leenders, Boxel, and Sterk, 2005). However, partly due to inherent error margins, individual studies utilising this technique sometimes ended up with conflicting results. Another big contributor to this could be the measurement height, as the shear stresses at metres above the surface and close to the surface do not correlate well.

Previous studies that primarily focused on characterising aeolian streamers (Baas and Sherman, 2005; Sherman et al., 2013) did this in varying environments with different morphological features and compositions of the sediment. However, no research has been conducted yet focusing on aeolian streamers as they occur along the Holland coast, which typically comprises a fine-grained narrow beach with tidal influences —thus where soil moisture plays an important role— and a steep, high foredune. Even though some of the findings by Baas and Sherman (2005) (arid sand mound; $D_{50} = 0.5 \mu\text{m}$) and Sherman et al. (2013) (broad foreshore; $D_{50} = 0.3 \mu\text{m}$) corresponded to a certain extent, it is not yet enough evidence to assume that streamers actually behave the same everywhere else. Besides, their interpretations, as well as those of many other studies involving synchronous wind and saltation measurements, are based on relatively short measurement periods (usually of the order of 10 min), thereby restricting the range of weather and transport conditions covered.

The principle instrument set-up used in this study mostly resembles the one used by Baas and Sherman (2005) as well. The Safires were known to show considerable variation in sensitivity, both depending on where exactly grains hit the sensitive impact surface (they contained a 'sweet spot') and, perhaps more importantly, among the sensors constituting the same array (Baas, 2004). Some of the direct consequences were that measurements had to be normalised and filtered down to the equivalent of the least sensitive sensor. In the end, only grains larger than 0.4 mm could be detected and the detection range was limited to 200 cnts s^{-1} . Furthermore, neither Baas and Sherman (2005) nor anyone else have also obtained high-resolution spatiotemporal saltation data as a function of height above the bed, which might reveal typical streamer properties and behaviour in that dimension.

Lastly, Baas (2006) already pioneered in the application of the wavelet transform technique to time series of sand transport and streamwise wind speed, but did not exploit the technique's full potential by sticking to the global energy density, which basically resembles the outcome of a traditional Fourier analysis. Thus, there still remains a practically unexplored opportunity in which to focus on the time history of 'local' energy density instead, with the potential of revealing characteristic time-varying fluctuations. Additionally, Baas (2006) did not analyse the cross-wavelet coherence in search of relationships between saltation and wind data, which, at the time, he ascribed to "its problematic computation".

2.2.1 Objective

This study aims to examine the properties and behaviour of aeolian sand streamers on beaches as they are typically found along the Dutch (or Holland) coast and possible relations to several attributes of the wind (e.g., velocity magnitude and turbulence intensity). Many of the shortcomings of the previously mentioned Safire set-up, which substantially complicated processing and analyses, are overcome through the use of a more sophisticated instrument: the Saltation Detection System (Winter et al., 2018). First, streamer patterns (both horizontally and vertically) are investigated on a qualitative basis by analysing contour maps of instantaneous saltation intensity. This part will be expanded by assessing the spatiotemporal saltation patterns as a function of specific wind attributes. Then, the wavelet transform technique is applied on time series of saltation intensity and specific wind attributes to find typical fluctuations, analyse how these vary in time, and to help elucidate on their mutual coupling. Thereafter, an appropriate time-averaging period is chosen with which to further evaluate the relationships between various saltation and wind characteristics. Finally, the (relative) effects of fetch and soil moisture on streamer intensity are examined in detail.

2.2.2 Research questions

Aeolian sand streamers are ubiquitous, but their exact appearance and consequences for sediment transport may differ from site to site, depending on morphology and other environmental factors. More independent research into streamers at a variety of different sites will yield a better understanding of this specific sediment transport phenomenon. Bearing that in mind and now focusing on a narrow sandy beach-dune system, the central question in this study is formulated as:

What are the properties and behaviour of aeolian sand streamers in a typical Dutch beach-dune system and how do these depend on the local transport conditions?

A number of naturally arising sub-questions are:

1. What streamer patterns and length scales occur under which transport conditions?
2. How are streamers related to the wind?
3. How are streamers reflected in the spatiotemporal variability of the saltation system?
4. How do fetch and surface moisture content control streamer formation across the beach?

Hypotheses

1. Streamer patterns are expected to be qualitatively similar to those presented in Baas and Sherman (2005) and length scales to be of a similar order of magnitude as those reported in Sherman et al. (2013) and Baas and Sherman (2005) (see 2.1.5).

2. If coherent turbulent flow structures, such as the large down-sweeping eddies (Hunt and Morrison, 2000) advanced by Baas and Sherman (2005), and associated gusts are indeed the primary drivers of streamer formation, an evident positive relation is expected between turbulence and saltation intensity.
3. Streamers are expected to contribute greatly to the spatiotemporal variability of the saltation transport on the beach (Davidson-Arnott and Bauer, 2009), its magnitude depending on the transport conditions.
4. From the water line towards the foredune, the increasing fetch is expected to be reflected in an increase in streamer formation/intensity (Anthony, 2008), while the inhibiting effect of surface moisture (by tidal inundation) is expected to contribute to this trend (Arens, 1996).

3 Methods

Field experiments were conducted from 2 October to 3 November 2017 on an almost daily basis at the beach near Egmond aan Zee, the Netherlands. This was done as part of an overarching field campaign going by the name of AEOLEX-II (a combination of 'aeolian' and 'experiment'), following an earlier edition (AEOLEX-I) held in 2015. A blog providing some more details on the expedition can be found on <http://geoblog.weebly.com/expedition-aeolex-ii>. The aim of the field campaign was to collect data on the local wind, wind-driven sand transport, surface moisture, ground water, vegetation properties and morphology from the low-tide line to the crest of the foredune. In this thesis the focus is mainly upon the measured wind and the associated sand transport, but in a few cases surface moisture is also considered.

3.1 Site description

3.1.1 Morphology

The study site was situated in a part of a beach-dune system roughly 3 km south of the town Egmond aan Zee in the Netherlands (Fig. 3.1). All data were collected within an area of about 150×80 m (alongshore \times cross-shore) centred at $52^{\circ}35'28''N$ $4^{\circ}36'51''E$. The coastline stretches almost north to south with only a slight clockwise rotation of $\sim 7.2^{\circ}$ (Google Earth Pro, 2019). Because the beach is confined by the North Sea on its west side and a steep ($\sim 22^{\circ}$ or $\sim 1:2.5$), ~ 22 -m high foredune front on its east side, it is relatively narrow with a maximum potential cross-shore fetch varying between 30 and 100 m, depending on the tide. Furthermore, it has a relatively gentle slope of $\sim 1.6^{\circ}$ or $\sim 1:36$ (determined from RTK-GPS data acquired on 11 October 2017) and its surface layer is composed of well-sorted quartz sand ($D_{50} \approx 227 \mu\text{m}$, see A.3) with shell fragments. The foredune is partially vegetated by predominantly Marram grass (*Ammophila arenaria L.*) (Winter et al., 2020) and runs continuously parallel to the beach, separating it from the hinterland. Other morphological features present in the area included an intertidal bar and trough and a series of up to ~ 1 -m high, vegetated embryo dunes located on the upper (dry) beach against the dune foot (~ 3 m above mean sea level).

3.1.2 Wind and wave climate

A wind rose from a nearby weather station (Fig. 3.2) indicates the regional wind conditions over the 10 years preceding the fieldwork period (i.e., 2008-2017). The dominant wind direction is southwest to south-southwest (i.e., oblique-onshore). In that same time period the annual mean wind speed was $7.2 \pm 3.7 \text{ m s}^{-1}$, and the maximum 10-min value reached was 27 m s^{-1} .

The site knows a semi-diurnal tide with a micro-tidal range between 1.2 (neap tide) and 1.8 m (spring tide) (Donker, Maarseveen, and Ruessink, 2018). Waves arriving at the wave-dominated beach are predominantly generated on the North Sea



FIGURE 3.1: Location of the study site indicated on a map adapted from <https://d-maps.com> and a south-facing drone image of the beach-dune system slightly north of the actually studied beach segment, taken during low tide on 22 September 2017 by Shore, The Hague.

(Winter, Gongrip, and Ruessink, 2015). Offshore in 20-m deep water, the significant wave height and period are 1.2 m and 5 s, respectively (Hage, Ruessink, and Donker, 2018). The large fetch of the North Sea basin enables northwesterly storms to produce especially large offshore wave heights of more than 7 m and periods of the order of 12 s (Winter, Gongrip, and Ruessink, 2015). Associated surges may well exceed 1 m (Winter et al., 2020), posing a serious threat to the survival of the intertidal bars and embryo dunes.

3.2 Instruments

During the entire field campaign a wide variety of instruments was deployed, of which only those relevant to this study are mentioned below. This particular study primarily relied on instruments capable of measuring saltation intensities and wind characteristics synchronously. A series of additional instruments were deployed in order to collect soil moisture data, footage of sand transport on the beach and determine various boundary conditions.

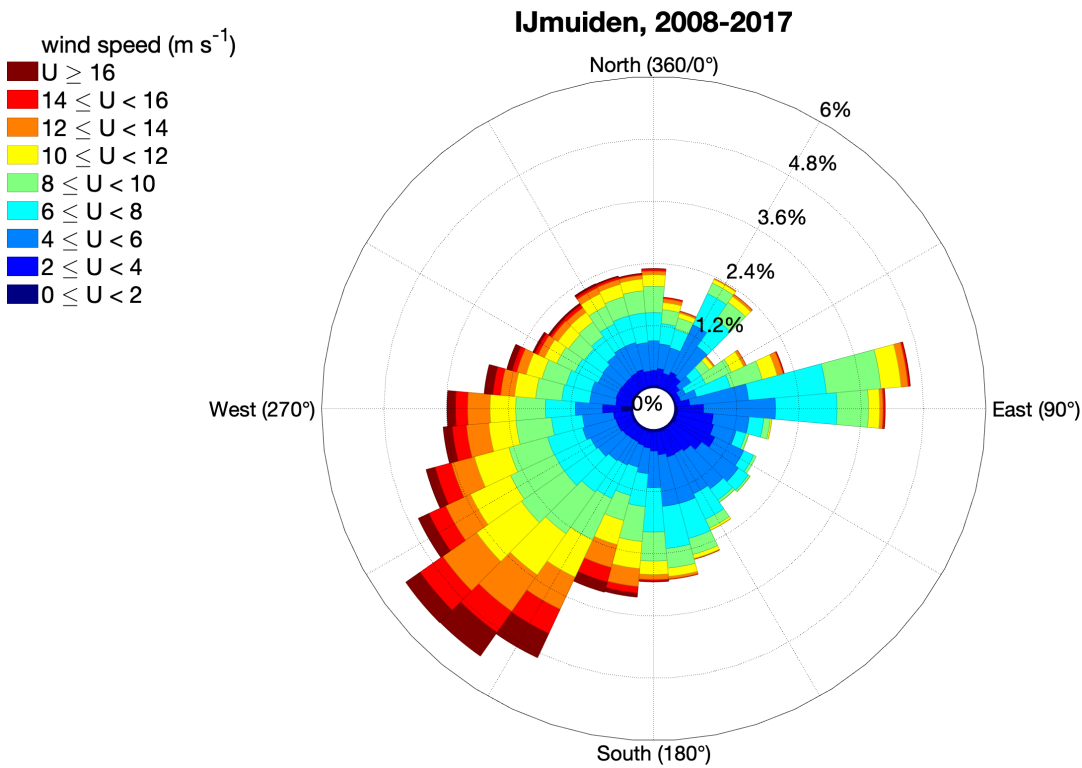


FIGURE 3.2: Wind rose from weather station IJmuiden (#225) of the Royal Netherlands Meteorological Institute (KNMI), located roughly 15 km south of the study site. Based on 10-minute data measured at a height of 10 m from 1 January 2008 up to and including 31 December 2017, downloaded from <https://projects.knmi.nl>.

3.2.1 Saltation detection system

Capturing the properties and behaviour of aeolian streamers requires a measuring devices capable of sampling at high frequency and operating at a high spatial resolution. In the past, multiple field-based designs of saltation impact sensors have been developed, one proving more successful than the other (e.g., Sherman et al., 2011; Barchyn and Hugenholtz, 2010). Nevertheless, the majority of these sensor designs failed to either partly or fully meet the following list of desired qualities:

- equal sensitivity to grain impacts amongst the deployed sensors;
- omnidirectional sensitivity;
- linear response to increasing/decreasing saltation intensity;
- a momentum threshold low enough to detect low rates of saltation, while still capable of disregarding noise from wind gusts, rain drops or insects;
- small (or narrow) enough to be deployed closely together;
- potential to translate output to mass flux (for quantitative analysis);
- serve as a low-cost solution.

Recently, a new instrument set-up was developed, the Saltation Detection System (henceforth abbreviated as SDS), which has been thoroughly tested in the lab and scored well for the majority of the above-listed qualities (Winter et al., 2018).

Saltation intensity (or impact rate) was measured using a total of three identical Saltation Detection Systems (SDS₂, SDS₃ and SDS₄; SDS₁ was out of service). Each SDS (Fig. 3.3) consisted of two oblong metal frames (or bars) attached to each other at right angles. The horizontal bar carried 32 impact sensors with a constant spacing of 0.10 m over a 3.10-m span, while the vertical carried 8 sensors that were mutually spaced in a logarithmic-ish fashion from bottom to top at 0.055, 0.065, 0.055, 0.065, 0.065, 0.245 and 0.140 m. The horizontal array spanned in wind-normal direction and was set to a height at which the underside of all sensitive sensor heads, insofar as possible, reached 0.10 m from the beach surface. The (midpoint of the) lowest sensor attached to the vertical bar had a fixed initial position at 0.035 m from the bed. However, this might not have stayed true for the entire length of the measurement run during periods with high deposition rates due to accumulation of sand underneath.

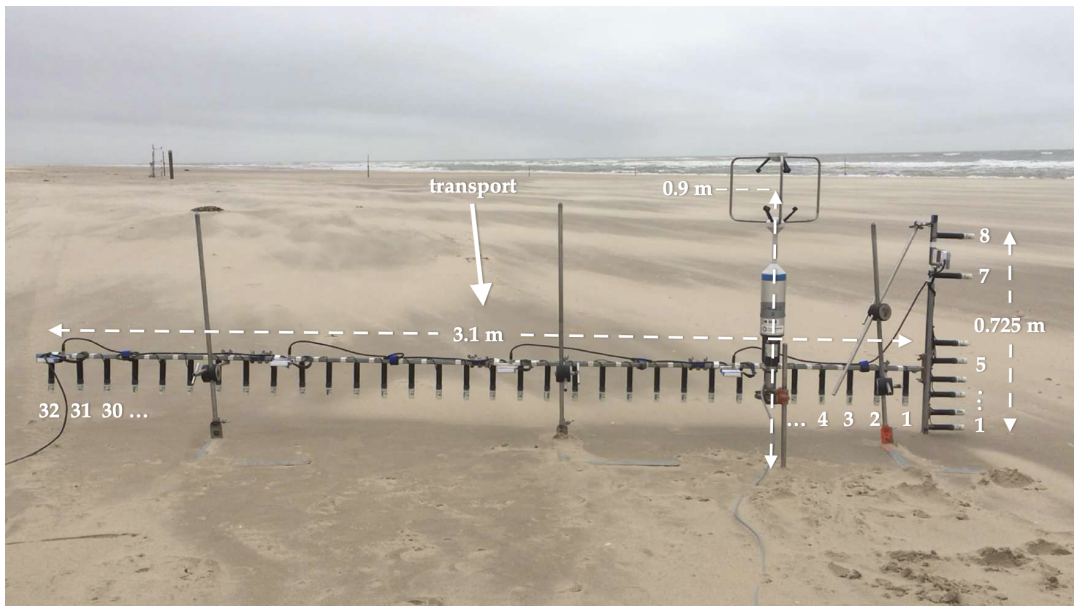


FIGURE 3.3: Typical set-up of a Saltation Detection System - Ultrasonic Anemometer combination: 32 horizontally and 8 vertically arranged impact sensors provide a high spatial resolution for the detection of saltation, while the anemometer provides a synchronous record of airflow. The whole system measures at 10 Hz.

Sensitive piezoelectric elements were contained inside the sensor heads, which had a curved surface area with a height of 0.034 m and an outer diameter of 0.020 m, resulting in a (curved) frontal sensing area of approximately $1.07 \times 10^{-3} \text{ m}^2 = 10.7 \text{ cm}^2$ (Winter et al., 2018). Each element generated an analogue voltage signal that was updated according to the number of grain impacts detected during every 0.1-s time step (i.e., at a rate of 10 Hz). Every 8 sensors in an array together formed a separate series connected to a counter box, which in turn transmitted the signal bundle to a data logger. One fully functioning SDS thus delivered a total of ($32 + 8 =$) 40×10 -Hz time series of grain impact rate (i.e., saltation intensity) in unit counts ($\text{s}/10$)⁻¹. A more in-depth description of the SDS and how it operates electronically, can be found in Winter et al. (2018).

Despite the fact that the collected data are not directly interchangeable with traditional absolute transport rates, they *do* provide a consistent measure of relative

saltation intensity. Wind tunnel experiments indicated a maximum of 9 % variability in the sensitivity to grain impacts amongst the SDS sensors, obtained at low saltation intensities (Winter et al., 2018). After additional evaluation of the mutual sensitivity in the field (Fig. A.1) this was deemed sufficiently equal. Nevertheless, saltation intensity variations amongst the impact sensors below this threshold variability of 9 % cannot be ascribed with complete certainty to variations in the saltation process itself.

3.2.2 Ultrasonic anemometer

Airflow characteristics were captured with ultrasonic anemometers (UA) (Young Model 81000RE), which provided 10-Hz time series of the three orthogonal components (u, v and w) of the wind vector (accuracy: $\pm 0.1\% \text{ rms} \pm 0.05 \text{ m s}^{-1}$) and sonic temperature (accuracy: $\pm 2^\circ \text{C}$), derived from the transit times of ultrasonic acoustic signals between the sensor heads (Boxel, Sterk, and Arens, 2004). For this study a total three UAs (UA₂, UA₃ and UA₄) were repeatedly deployed, each corresponding to their equally labelled SDS counterpart. Co-located, the SDS and UA (henceforth SDS-UA) constituted the main instrument set-up (Fig. 3.3) in this study. The fact that these instruments were able to measure with the same high sampling frequency allowed for convenient synchronisation and hence correlation of their measurement records.

The UA was systematically positioned directly behind the SDS – yet not so close that it would potentially interfere with the saltation process in front of the SDS – in line with the observed saltation field and close to the vertical sensor array. Its measuring height was consistently set to 0.90 m from the surface as to capture the airflow as close as possible to the height at which the saltation transport was monitored by the SDS, for the sake of reliability of correlations, while minimising the risk of damage by saltating grains. During these height adjustments, a bubble level placed on top of the UA was used to establish its horizontal plane. Finally, the UA's inner coordinate system was established by aligning a look-through scope, placed against its 0° and 120° sensor radii, with a distant reference beach pole, of which the exact coordinates were known.

3.2.3 Additional instruments

In addition to the SDS-UA combination, a number of supplemental instruments were also deployed. A Delta-T ThetaProbe (type HH2) was used to capture the gravimetric soil moisture content of the top layer of the beach. By inserting its four 2-cm stainless steel rods into the soil and sending through an electrical signal, its sensors could detect changes in the soil's apparent dielectric constant. The resulting voltage could then be converted to soil moisture content by means of a calibration curve. For the exact calibration procedure and the resulting curve, together with a more detailed description of how the device works, the reader is referred to Tuijman (2018).

A weather station (referred to as meteo-station) located within a radius of some 50 m and equipped with several different measuring devices recorded a series of meteorological variables, including temperature, humidity, air pressure, rainfall, wind speed and direction, and incoming and outgoing solar radiation. These variables were sampled at 5-s intervals and averaged over 10 min (as in Arens (1996)). Furthermore, two cup-anemometer towers were deployed to measure the vertical wind profile and wind direction near the high-water line and at the foot of the foredune

with a sampling period of 1 min. Beach and foredune topography were acquired by terrestrial LiDAR and RTK-GPS, of which the latter was also used to measure the coordinates of all instrument deployments and measurement locations. Time-averaged time history of the water level just off the beach was derived from pressure records from an on-site installed wave gauge (OSSI-010-003B) measuring just landward of the low-tide level ($-0.273\text{ m} +\text{NAP}$) with a sampling frequency of 5 Hz.

Additionally, during the fieldwork period multiple video recordings were made and countless pictures taken using the cameras of either an iPhone or GoPro device. Some footage proved suitable for qualitative investigation of streamers and streamer motion. For instance, by setting up reference points and using a stopwatch when eyeballing streamers features visible in the recording, the velocity of streamers at certain wind speeds could be estimated.

3.3 Data collection

3.3.1 Field preparations

Efforts were made to reduce disturbances of the beach surface at the site to a minimum. At the time of the expedition, which took place in autumn, the touristic high season had already passed. Also, the study site was located several kms away from the most popular and crowded parts of the coast. Nevertheless, it remained impossible to completely prevent the occasional people on a stroll, patrolling lifeguard, bikers and even some horse riders from passing by during measurement periods. A number of precautionary measures that were taken, included setting up a perimeter with ribbon around the saltation field under observation and placing informative/warning signs.

3.3.2 Saltation and wind data

Sediment transport and wind data were collected with the SDS-UA combination during a total of 19 measurement runs of varying duration, at varying locations and under very diverse weather conditions (see Table 3.1). Coordinates of the UA and either end of the SDS's horizontal span were determined by means of an RTK-GPS device. Harsh weather conditions together with limited availability of time and dry beach surface were factors restricting the number and duration of deployments on most days.

Streamwise set-ups

Only two measuring days (the 11th and the 27th) lent themselves to the deployment of all three SDS-UA combinations at the same time, during which they were arranged in a more or less streamwise fashion (see Fig. 3.6). Both days featured light showers every now and then, but on the 11th they were slightly more prolonged. On 11 October the regional wind direction, as measured by the weather station at 4.15 m above the bed, was persistently southwest with speeds ranging from 10 to 14 m s^{-1} . On 27 October the wind direction was more variable, but came predominantly from the north-northwest with speeds ranging from 6 to 11 m s^{-1} . Since the tides controlled the available beach surface area, and assembling all the instrument components was a time-consuming job, the lengths of the measurement records sometimes varied greatly between the SDS-UA deployments. Therefore, only data collected

from the final deployment until the first disassembly were used in the subsequent streamwise-specific analyses.

Threshold conditions

Two other measuring days were particularly suitable for investigating threshold saltation transport. Both 17 and 25 October featured seemingly perfect threshold transport conditions, i.e., moderate wind, no rain and low soil moisture levels (i.e., $\theta_v \approx 2\%$ upwind of the SDS). For instance, on the 25th the regional wind speed steadily decreased from about 8.2 m s^{-1} at the start of the measurement run down to about 4.8 m s^{-1} at the end, accompanied by a gradual change in wind direction from some 260° to about 315° , with both variables measured by the on-site weather station at 4.15 m above the bed. Furthermore, SDS-UA₄ was deployed just on the high-water line, while SDS-UA₂ was positioned slightly seaward of the embryo dunes. At times the wind was only just strong and gusty enough to occasionally trigger streamer formation. Seaward of the high-water line, however, the soil moisture content suddenly increased up to 14 %, also being reflected by the fact that virtually no transport was detected by SDS-UA₄ all day long. Conditions on the 17th were very similar but with SDS-UA₂ and SDS-UA₃ both deployed high up the upper beach.

3.3.3 Soil moisture data

On 11 October, a series of soil moisture measurements were taken using the Delta-T ThetaProbe along transects aligned with the saltation field in front of SDS-UA₃ and SDS-UA₄, i.e., perpendicular and adjacent to their horizontal spans (cyan dots in Fig. 3.6). The transects were divided into a series of measurement locations (or markers) spaced at more or less equal (streamwise) intervals of $\sim 2 \text{ m}$, with the first one positioned in line with the SDS's horizontal span. Also here an RTK-GPS device was used to determine each marker's location. At each of these markers, groups of 5 measurements were taken at a time – usually well within a minute of time – and subsequently averaged to account for small-scale spatial variability. Measurement rounds were carried out approximately every half hour and covered a total time period of about 7.5 h and 3.5 h at SDS-UA₄ (mid beach) and SDS-UA₃ (upper beach), respectively.

TABLE 3.1: Overview of all SDS-UA deployments during the field campaign. From left to right: deployment number, day number in October 2017, deployment period, deployed SDS-UA, relative location on beach, (inter)cardinal wind direction, mean wind speed (as measured by the UA) and highest experienced rain intensity.

#	Day	Time (MET)	SDS-UA _i	Location	Dir	\bar{U} (m s ⁻¹)	Rain
1	4 th	11:00:00 – 13:54:33	4	mid beach	W	7.91	-
2	5 th	11:21:17 – 14:06:50	4	upper beach	NW	9.07	moderate
3	6 th	11:30:00 – 13:36:06	4	upper beach	NW	8.79	moderate
4 ¹	11 th	10:41:05 – 16:17:00	3	upper beach	SW	9.51	light
5 ¹	11 th	11:25:47 – 17:03:58	4	mid beach	SW	10.3	light
6	11 th	14:21:31 – 16:43:33	2	dune foot	SW	9.07	light
7 ²	17 th	10:42:57 – 15:49:09	2	dune foot	SW	5.61	-
8 ²	17 th	12:33:25 – 16:15:08	3	upper beach	SW	5.91	-
9	20 th	10:45:32 – 13:42:46	2	intertidal bar	SSW	10.4	heavy
10	20 th	11:46:22 – 13:29:50	3	mid beach	SSW	10.6	heavy
11	22 nd	12:32:34 – 15:00:00	3	mid beach	W	7.31	moderate
12	24 th	15:45:50 – 16:47:01	3	mid beach	SW	8.05	-
13 ²	25 th	10:19:27 – 14:53:54	2	upper beach	W	4.11	-
14 ²	25 th	11:17:55 – 14:20:53	4	mid beach	W	4.70	-
15	27 th	10:27:04 – 16:30:08	4	upper beach	NW	6.14	light
16	27 th	11:00:09 – 16:18:59	3	upper beach	NW	6.92	light
17	27 th	12:14:52 – 16:44:34	2	upper beach	NW	6.94	light
18	29 th	14:00:28 – 16:39:31	4	upper beach	NNW	9.13	moderate
19	30 th	15:00:00 – 17:37:16	4	upper beach	NNW	4.99	light

¹ Soil moisture measurements along transport-parallel transect.

² Ideal threshold-transport conditions.

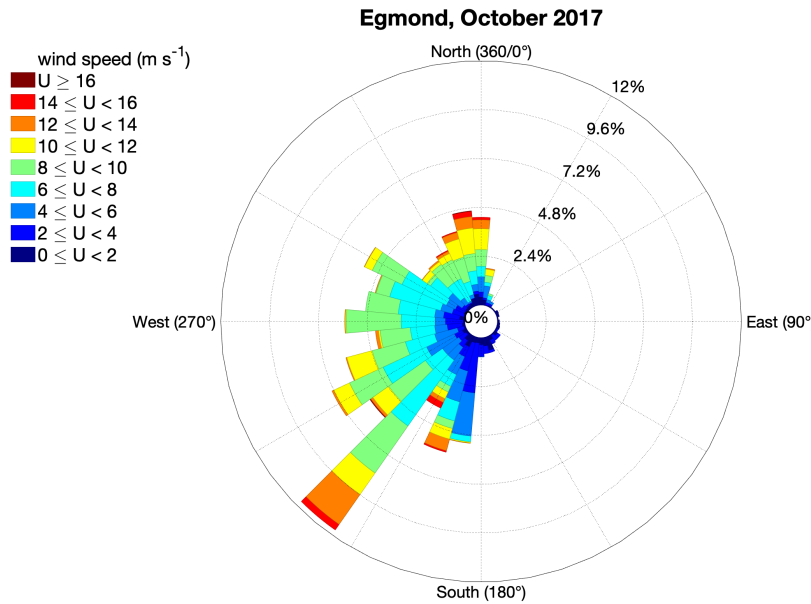


FIGURE 3.4: Wind rose from the on-site weather station. Based on 10-minute data measured at 4.15 m from the bed from 3 October, 16:00 MET to 30 October, 18:00 MET.

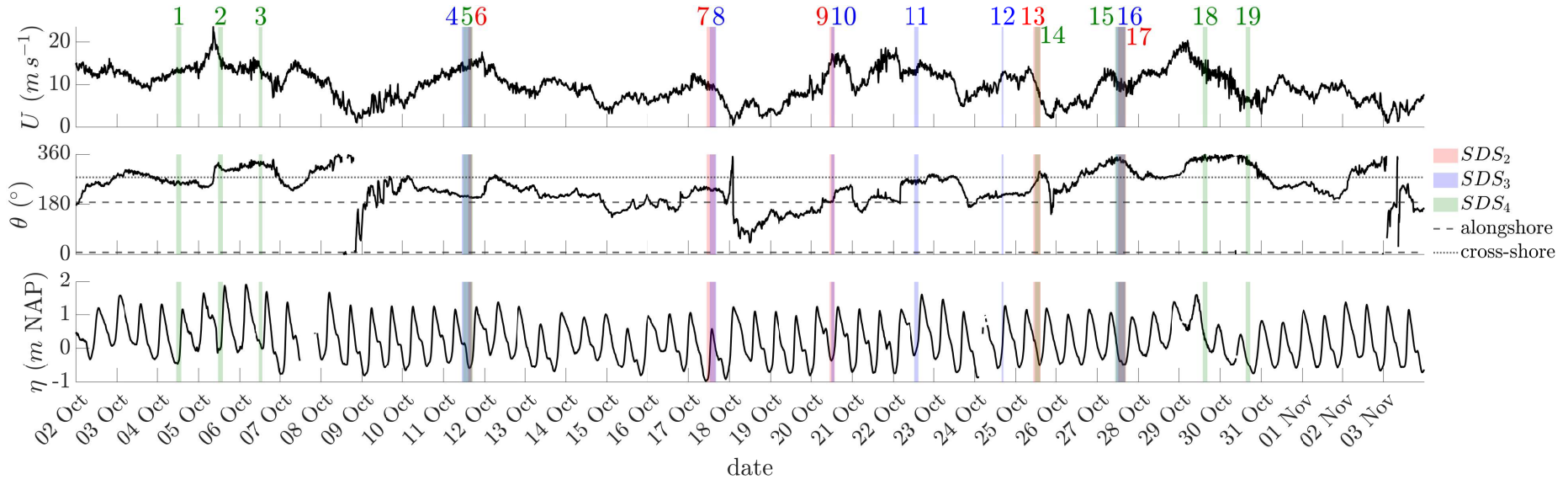


FIGURE 3.5: Offshore wind speed (top panel) and direction (middle panel), and tidal elevation (bottom panel) as measured by the IJgeul stroommeetpaal, IJmuiden, during the field campaign in 2017. Data downloaded from <https://waterinfo.rws.nl>. Coloured areas indicate SDS-UA deployments with their corresponding deployment numbers listed on top, which correspond to the numbers in Table 3.1.

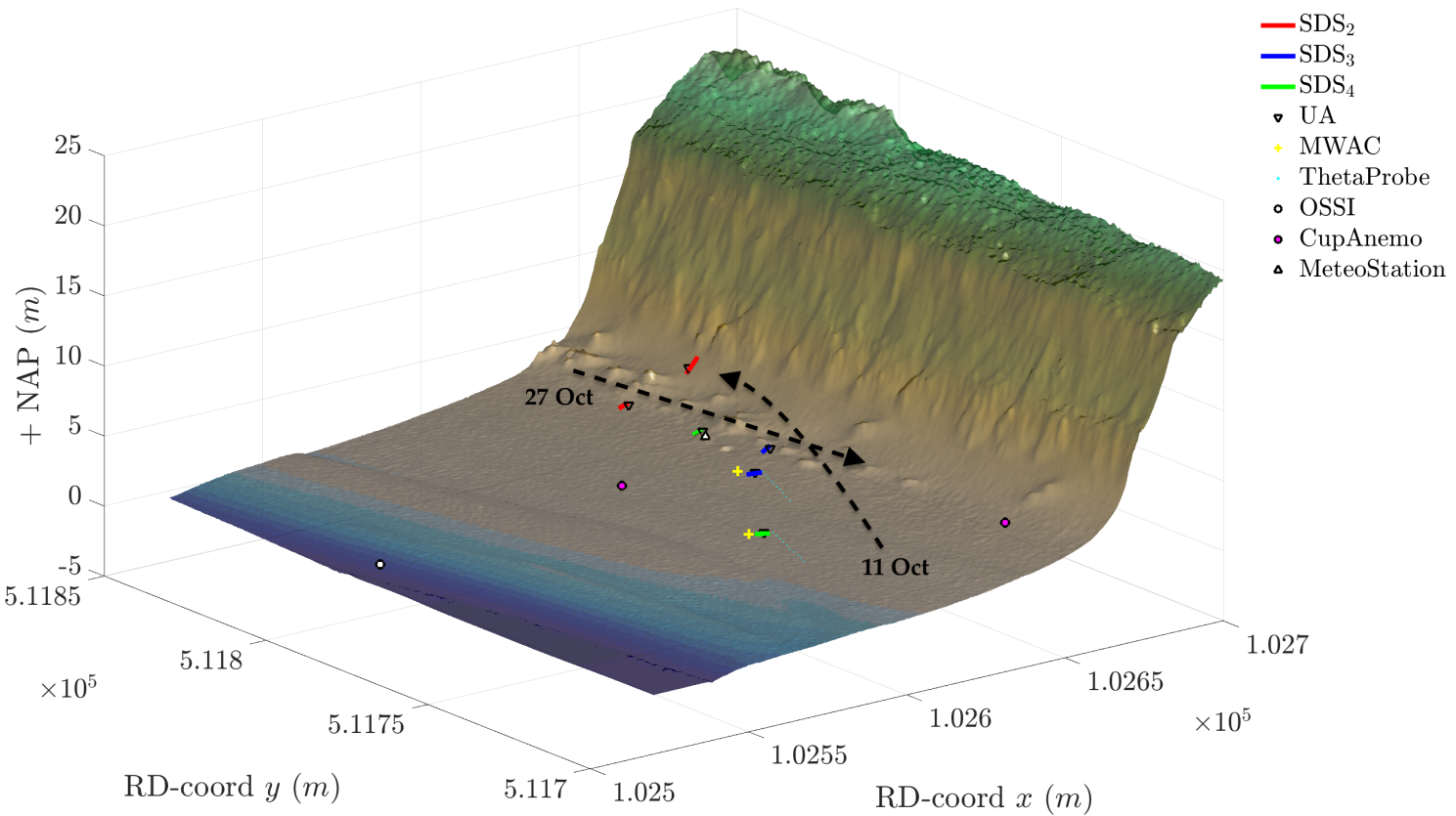


FIGURE 3.6: Map depicting the locations of the deployments and measurements on 11 and 27 October 2017. Black dashed arrows indicate downwind direction parallel to the SDS-UA alignment on that day. Coordinate system: RD2008 (Rijksdriehoek). Shown locations may have a slight offset from actual locations with respect to the elevation model, as the former were measured with RTK-GPS, whereas the latter was acquired from a LiDAR survey.

3.4 Data preparation

Measuring saltation intensities in the field with the SDS is not straightforward. The delicate components of its impact sensors in combination with the sometimes rough transport conditions unavoidably leads to complications. Therefore, a series of measures had to be taken to secure a good-quality data set to work with at the start of the analysis phase.

3.4.1 Sticky sand

Sometimes during an SDS-UA deployment, heavy rainfall could cause sand to become sticky and accumulate onto the sensitive parts of its sensors, compromising their ability to detect grain impacts, hence their reliability. Such conditions required periodic cleaning of the sensor heads (Fig. 3.7), which was done by gently wiping them off with paper towel without disturbing the beach surface upwind of the instrument. Every time during such procedure the exact time was registered, so that later on the data recorded within a couple of minutes from that time could be removed.



FIGURE 3.7: Impact sensors being wiped clean after having become clogged with sticky wet sand during a period of intense rainfall.

3.4.2 Impact sensor malfunctioning

At the conclusion of the data collection phase, a thorough quality check revealed symptoms of sensor malfunctioning in several parts of the data set, of which some had been overlooked during the interim checks. These symptoms may have been caused by temporarily or permanently defect impact sensors or by the transport conditions for instance leading to severe sticky-sand situations. Examples of impact sensors exhibiting malfunctioning behaviour consistently throughout the field campaign were:

- SDS₂: sensors 25 and 27 copied each other's output
- SDS₃: sensor 15 produced no realistic output (only zeroes)

Such resulting outputs had to be corrected for in ways that would still allow for proper analyses, which was achieved by either omitting the suspected erroneous data or by making use of smoothing methods. The former method was used primarily in the case of finding the threshold values and other relations between parameters (4.3 and 4.2), whereas the latter was only used in the case of generating contour maps (4.1).

3.4.3 Counter box malfunctioning

Another symptom of malfunctioning counter boxes was the sudden eight-fold output of zeroes at one or two timesteps for a group of eight sensors (coupled to the same counter box) directly followed by a timestep with strong outliers (see Fig.

3.8). The fact that these symptoms only occurred during periods of intense transport suggests that the counter box in question experienced a sudden saturation of electronic signals needing to be processed in one timestep. Presuming that impact counts of one timestep were instead added to the next – those numbers were consistently about twice as large as the subsequent timestep – this was solved by replacing the eight zeroes and the outliers in the following timestep by the mean over the two timesteps. In the much less frequent case of two consecutive timesteps with zeroes, the mean was taken over all three timesteps. Data from the horizontal and vertical sensor arrays were handled the same way.

	14	15	16	17	18	19	20	21	22	23	24	25	26
9	190	180	270	230	120	100	150	140	210	180	200	170	180
10	180	170	120	180	140	100	120	220	200	230	230	150	220
11	130	150	170	140	90	80	100	150	220	190	160	180	170
12	150	210	140	150	50	70	130	220	220	180	190	190	200
13	110	140	160	160	100	130	160	160	160	270	190	150	200
14	140	240	170	60	40	90	200	190	260	210	180	110	180
15	120	250	140	90	30	40	210	220	140	130	170	170	120
16	120	180	190	90	170	120	50	170	180	150	190	70	120
17	200	190	140	150	190	170	150	160	270	170	110	130	170
18	100	120	170	190	180	150	270	150	240	160	90	100	100
19	220	140	170	140	170	180	180	150	200	170	110	110	180
20	200	180	150	140	130	200	210	180	150	230	150	180	190
21	220	200	210	200	170	170	180	150	190	160	190	210	270
22	110	160	220	200	190	190	150	120	190	150	130	210	260
23	140	200	190	170	140	150	130	170	140	160	210	200	260
24	150	200	140	130	70	130	130	180	170	160	220	180	220
25	200	190	140	0	0	0	0	0	0	0	0	140	180
26	120	150	150	330	360	470	390	320	280	380	350	190	160
27	150	130	180	150	210	210	220	170	200	220	170	210	140
28	150	100	170	170	120	190	190	200	160	200	120	110	160
29	170	200	120	0	0	0	0	0	0	0	0	150	170
30	130	220	160	390	290	440	410	290	380	370	360	220	160
31	160	210	160	140	150	120	230	180	160	190	170	140	170
32	190	220	240	190	160	180	200	130	190	190	180	160	180
33	160	200	170	150	190	170	230	130	170	210	170	120	180
34	190	160	180	170	180	180	150	170	240	160	130	170	220
35	160	170	160	150	160	180	270	220	180	180	190	200	180
36	100	140	140	140	160	160	220	230	170	140	220	180	170

FIGURE 3.8: A typical output (in cnts s^{-1}) of part of the horizontal array of an SDS featuring two examples of the counter box error described in the text. Rows denote the 0.1-s timesteps and columns the array of impact sensors in that order. Zeroes and subsequent outliers are highlighted in yellow and red, respectively.

3.4.4 Impact sensor saturation

In the final part of the quality control phase, data from the vertical sensor array of the SDS were used to infer whether the impact sensors of the horizontal array (measuring at 0.1 m above the ground) had probably experienced saturation symptoms, which were not already solved by the measures described above. In such case their measurements could not be considered reliable. Therefore, for each timestep the corresponding sample (i.e., array of contemporaneous data) was marked unreliable and omitted from the data set if it showed at least one of the following symptoms:

- the UA record displays an error code (\rightarrow no correlation possible)
- $I > 400 \text{ cnts s}^{-1}$
- $I_{V2} = \text{NaN}$
- $I_{V3} - I_{V2} \geq 50 \text{ cnts s}^{-1}$

- $I_{V2} < I_{V4}, I_{V5} \dots I_{V8}$

where I_{V1} and I_{V8} indicate the saltation intensities measured at the lowest and highest sensor positions of the vertical array, respectively (see Fig. 3.3). Sensor V2 (0.09 m) instead of sensor V1 (0.035 m) was taken as a reference, since the latter was positioned much closer to the bed than the impact sensors of the horizontal array, which were most relevant to this study. The latter two conditions were based on the assumption that saltation intensity generally decreases with vertical distance. Where the data displayed the opposite trend, chances were high that the lower sensor – and any sensor at a comparable height – was either saturated or clogged with wet sand. An arbitrary threshold of 50 cnts s⁻¹ was taken for the fourth condition to prevent samples from being needlessly marked unreliable if, by chance, only a few counts less were detected by the lower sensor (especially in the case of light transport conditions). In addition, the second condition states that if any of the impact sensors had measured more than 400 cnts s⁻¹, that timestep was also wholly disregarded, as the accuracy of counted with respect to observed saltation rates rapidly declines beyond that point (see the results of sensitivity analysis presented in Fig. 11 in Winter et al. (2018)). Details on the number of samples showing which symptoms are given in Table 3.2. In the end, on average about 20 % of the data had to be disregarded, mostly due saturation issues.

TABLE 3.2: Frequency of occurrence of samples showing saturation/malfunctioning symptoms per SDS-UA system. Total number of samples are given between brackets behind each system name. All positive encounters were removed from the data set, except for the counter box errors, which were handled as explained in 3.4.3.

	SDS-UA₂ (701772)	SDS-UA₃ (713126)	SDS-UA₄ (1000037)
UA error code	1666 (0.2%)	175 (0.0%)	37 (0.0%)
$I > 400 \text{ cnts s}^{-1}$	17941 (2.6%)	9583 (1.3%)	18838 (1.9%)
$I_{V2} = \text{NaN}$	25353 (3.6%)	107277 (15.0%)	33318 (3.3%)
$I_{V3} - I_{V2} \geq 50 \text{ cnts s}^{-1}$	75066 (10.7%)	58095 (8.1%)	86237 (8.6%)
$I_{V2} < I_{V4}, I_{V5} \dots I_{V8}$	11504 (1.6%)	6649 (0.9%)	45760 (4.6%)
Counter box error	3154 (0.4%)	4093 (0.6%)	7089 (0.7%)
Total encounters	134684 (19.2%)	185872 (26.1%)	191279 (19.1%)
Total emitted	131530 (18.7%)	181779 (25.5%)	184190 (18.4%)

3.5 Formulae and expressions

This section provides the equations that were used to obtain all of the expressions representative of the saltation system and corresponding wind conditions.

3.5.1 Saltation data

Temporal mean

For the purpose of improving correlation and finding long-term relationships between wind characteristics and saltation intensity, temporal means were taken from

the data in the following manner:

$$\mu = \frac{1}{N} \sum_{t=1}^N I_t = \frac{I_{t=1} + I_{t=2} + \cdots + I_{t=N}}{N} \quad (3.1)$$

where μ is the temporal mean saltation intensity over a specified time interval, N the number of observations within that time interval and I_t the instantaneous saltation intensity at timestep t (where $t=1$ is the first observation). In this study, the following temporal scales were considered in addition to the instantaneous scale (i.e., 0.1 s):

- 1 s ($N = 10$)
- 1 min ($N = 60$)
- 10 min ($N = 600$).

Temporal variability

Variability in saltation intensity can be expressed by the (sample) standard deviation. Temporal variability was calculated with respect to the mean of each time interval (Eq. 3.1):

$$\sigma = \sqrt{\frac{\sum_{t=1}^N (I_t - \mu)^2}{N - 1}} \quad (3.2)$$

where σ is the temporal standard deviation of saltation intensity. However, variability expressed as the standard deviation often gives a biased impression, for it must be regarded in context of the mean. Therefore, when examining causality between, for instance, temporal variability in wind speed (expressed by gustiness or turbulence) and saltation intensity, it is convenient to consider a standardised measure:

$$CV = \frac{\sigma}{\mu} \cdot 100 \% \quad (3.3)$$

where CV is the temporal coefficient of variation (or relative standard deviation) of saltation intensity.

Spanwise mean

For the sake of convenience, in many occasions the data were spatially averaged over the span of the horizontal sensor array, which generally counted 32 sensors:

$$\mu_y = \frac{1}{32} \sum_{p=1}^{32} I_p = \frac{I_{p=1} + I_{p=2} + \cdots + I_{p=32}}{32} \quad (3.4)$$

where μ_y is the instantaneous spanwise-mean saltation intensity measured over the horizontal sensor array and I_p the instantaneous saltation intensity measured at individual sensor position p . Here, $p=1$ indicates the impact sensor located closest to the vertical sensor array (see Fig. 3.3).

Spanwise variability

In addition to temporal variability, the instantaneous variability in the spanwise dimension (i.e., over all impact sensors of the horizontal array) can be computed as

$$\sigma_y = \sqrt{\frac{\sum_{p=1}^{32} (I_p - \mu_y)^2}{32 - 1}} \quad (3.5)$$

where σ_y is the spanwise standard deviation of saltation intensity. Based on the same principle as for Eq. 3.3, a standardised measure is given by

$$CV_y = \frac{\sigma_y}{\mu_y} \cdot 100 \% \quad (3.6)$$

where CV_y is the spanwise coefficient of variation (or relative standard deviation) of saltation intensity.

3.5.2 Wind data

Coordinate-system transformation

For the sake of accuracy as well as convenience, the UA's intrinsic coordinate system was transformed into an orthogonal system in which the positive x -axis runs parallel to the beach surface in the direction of the mean flow, the positive y -axis with a 90° angle to the right parallel to the surface and the positive z -axis upward perpendicular to the surface (or wall). This transformation was achieved by invoking three sets of equations presented in Boxel, Sterk, and Arens (2004), which perform the so-called yaw, pitch and roll rotations (Fig. 3.9) on the instantaneous 3-D wind velocity data. Boxel, Sterk, and Arens (2004) recommend these rotations in the case of level UAs on sloping terrain like the beach surface in this study, as otherwise slope errors of about 9 % and 4 % per degree of slope can undesirably be introduced in the computations of the Reynolds stress and shear velocity, respectively.

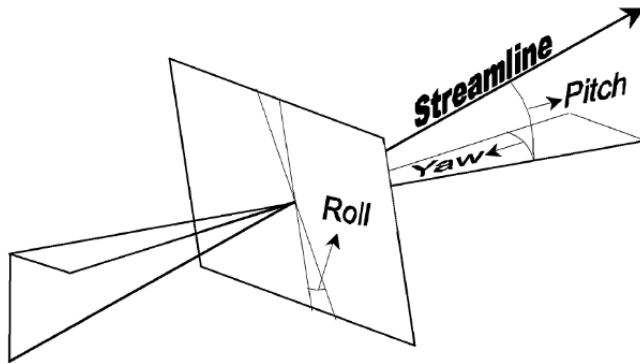


FIGURE 3.9: Schematic of the three rotations required to correctly orientate the frame of reference of the UA with respect to the stream surfaces. Copied from Kaimal and Finnigan (1994).

Yaw rotation:

$$\theta = \tan^{-1} \frac{\bar{v}_0}{\bar{u}_0} \quad (3.7)$$

$$u_1 = u_0 \cos \theta + v_0 \sin \theta \quad (3.8)$$

$$v_1 = -u_0 \sin \theta + v_0 \cos \theta \quad (3.9)$$

$$w_1 = w_0 \quad (3.10)$$

where θ is the time-averaged flow angle, u_0 , v_0 and w_0 are the instantaneous velocity components of the wind as locally observed by the UA and u_1 , v_1 and w_1 the resulting components after yaw rotation. Note that this rotation does not affect the vertical velocity component.

Pitch rotation:

$$\phi = \tan^{-1} \frac{\bar{w}_1}{\bar{u}_1} \quad (3.11)$$

$$u_2 = u_1 \cos \phi + w_1 \sin \phi \quad (3.12)$$

$$w_2 = -u_1 \sin \phi + w_1 \cos \phi \quad (3.13)$$

$$v_2 = v_1 \quad (3.14)$$

where ϕ is the time-averaged streamline slope (Fig. 3.9) and u_2 , v_2 and w_2 are the resulting instantaneous velocity components after yaw and pitch rotation. Note that this second rotation does not affect the streamwise-perpendicular velocity component.

Roll rotation:

$$\psi = \frac{1}{2} \tan^{-1} \frac{2 \bar{v}_2 \bar{w}_2}{\bar{v}_2^2 - \bar{w}_2^2} \quad (3.15)$$

$$v = v_2 \cos \psi + w_2 \sin \psi \quad (3.16)$$

$$w = -v_2 \sin \psi + w_2 \cos \psi \quad (3.17)$$

$$u = u_2 \quad (3.18)$$

where ψ is the time-averaged roll-rotation angle (Fig. 3.9) and u , v and w are the resulting instantaneous velocity components after yaw, pitch and roll rotation. Note that this third rotation does not affect the streamwise velocity component. Now, the new u , v and w components run parallel to the above-mentioned x -, y - and z -axes, respectively.

Data smoothing

In order to reduce the spikiness of the wind data, for most analysis procedures the instantaneous velocity components were smoothed in advance using a 3-s moving-average filter, which is a method commonly applied by the Dutch national weather service, KNMI. Only for the computation of the turbulence kinetic energy (Eq. 3.20) and generation of wavelet transform scalograms the unsmoothed data were used.

Wind speed and direction

The mean horizontal (or surface-parallel) wind speed is represented by \bar{u} , since the means of the orthogonal components, \bar{v} and \bar{w} , are (close to) zero by definition. The mean wind direction with respect to north was computed with Eq. 3.7. Corrections were made for the UA's orientation in the field through the application of Pythagorean theorem to its alignment relative to a reference beach pole, which included a 30°-angle adjustment accounting for the orientation of the look-through scope relative to the UA's internal axes.

Shear velocity

An analogous version of the shear stress in units of velocity is the shear (or wall-friction) velocity. Assuming a vertical logarithmic velocity profile, this term was approximated by

$$u_* = \bar{u}_z \kappa \left[\ln \left(\frac{z}{z_0} \right) \right]^{-1} \quad (3.19)$$

where u_* has unit m s^{-1} , \bar{u}_z is the mean horizontal wind speed (m s^{-1}) at height z (m), κ the Von Kármán constant and z_0 the roughness length (m). In a few cases the instantaneous version of u_* is approximated by substituting \bar{u}_z with the instantaneous record of u_z . Prior to the computation of the shear velocity, the roughness length (z_0) was determined from logarithmic fitting through the velocity profiles (Prandtl-Von Karman law-of-the-wall) of the two on-site cup-anemometer towers (Fig. A.4). Due to the discrepancy between the values for z_0 acquired at the upper and lower beach, it was decided to set its value to an in-between value of 1×10^{-3} m, which is common for fine-grained (smooth) surfaces.

Turbulence kinetic energy

A computationally practical expression of turbulence intensity is the kinetic energy of turbulent fluctuations, also 'turbulence kinetic energy' (TKE). Whereas the mean of the turbulent deviations (u' , v' and w') is zero by definition, their variance is not and can be used as an indication of the magnitude, or intensity, of TKE (Schönenfeldt and Löwis, 2003). The corresponding time-averaged equation is derived from the Navier-Stokes equations and is in literature frequently referred to as the 'k-equation' (Schlichting and Gersten, 2017):

$$k = \frac{1}{2} \left[\overline{(u')^2} + \overline{(v')^2} + \overline{(w')^2} \right] \quad (3.20)$$

where k has unit $\text{m}^2 \text{s}^{-2}$ (or J kg^{-1}) and u' , v' and w' represent the unsmoothed 3-D fluctuating components about the mean flow (see Eq. 2.2). The coefficient of variation of (or turbulence intensity relative to) the wind speed is defined as

$$CV_k = \frac{\sqrt{k}}{\bar{U}} \cdot 100 \% \quad (3.21)$$

where \bar{U} is the mean (3-D) wind speed (m s^{-1}) defined as

$$\bar{U} = \sqrt{\bar{u}^2 + \bar{v}^2 + \bar{w}^2}. \quad (3.22)$$

3.6 Data analysis

In this section the analysis procedures which are thought to require some extra explanation are more extensively described.

3.6.1 Transport contour maps

Spatiotemporal maps of saltation intensity were generated by lining up the time series of all impact sensors from both the horizontal and vertical arrays. In theory, by invoking Taylor's (1938) frozen turbulence hypothesis, time may substitute for the

streamwise x -direction, as long as the timescale of advection is short enough with respect to that of the internal evolution of the flow. However, the scaling of the x -axis relative to the (spanwise) y -axis requires knowledge of the propagation speed of the saltation concentrations, which is hard to estimate and is likely to be highly unsteady and probably non-uniform as well. Since this is unaccounted for, the produced transport maps are not to scale. Nonetheless, they still provide a reasonable qualitative display of the various length and timescales of streamers. Streamwise length scales could still be estimated by adopting, for example, the characteristic saltation-cloud propagation speed of 3.6 m s^{-1} reported by Baas and Sherman (2005). Furthermore, the majority of contour maps were produced from data acquired by SDS₄, for this specific instrument exhibited the least malfunctioning symptoms throughout the fieldwork period, hence was considered most reliable. As an exception to the second rule in 3.4.4, intensities exceeding 400 cnts s^{-1} were this time allowed, since that specific condition did not compromise the purpose of these contour maps. Lastly, all contour maps were subjected to a Gaussian filter (*window* = 5) in the time domain (x -axis) in order to reduce the inherent noise of instantaneous data.

3.6.2 Wavelet transform

Previous studies already demonstrated the difficulty of relating sediment transport flux to a single flow parameter such as wind speed or kinematic shear stress by using simple correlation analysis in the time domain alone. However, classic Fourier analysis is not appropriate for the intermittent and non-Gaussian-distributed nature of streamers. Therefore, an attempt was made to use wavelets instead. More extensive background information on the application of wavelets is given in Appx. C.

A MATLAB routine was developed in which a series of selections of the time series of instantaneous saltation intensity (I) and horizontal wind speed (u) were analysed by means of the wavelet transform. In order to allow for a more meaningful comparison between the energy spectra of different time series, both were normalised (i.e., zero mean, unit variance) prior to the application of the wavelet transform. The (standard) z -scores were calculated as

$$z = \frac{x - \bar{x}}{\sigma} \quad (3.23)$$

where x is a random variable, \bar{x} the population mean and σ the population standard deviation. Thereafter, the individual 1-D continuous wavelet transform (CWT) coefficients were computed following Eq. C.1 and subsequently inspected for the appearance of notable (quasi-)consistent energy-density distributions. Similar to the case of the transport contour maps, the restrictions imposed by the rules listed in 3.4.4 were ignored by exception, as these would leave too many holes in the data records, while such symptoms did not necessarily compromise the purpose of these kind of analyses.

From the impressive list of analysing wavelet functions, the generalised Morse wavelet was chosen for the continuous wavelet transform (CWT) for its flexibility and availability from the MATLAB package. It allows for easy tweaking of two parameters controlling the time and frequency spread to have it more closely match the behaviour of the signal anticipated on. In most cases the wavelet parameter γ was set to 3, because for that value the wavelet is perfectly symmetric in the frequency domain and has zero skewness. Either increasing or decreasing that value would lead to positive or negative skewness, respectively. The number of voices per octave

ν was set to 48, the finest possible discretisation of the scale parameter a , which enables higher-fidelity signal analysis. In order to ensure the oscillatory components with equal amplitudes but at different scales actually produced equal magnitudes in the CWT, the wavelet was L1-normalised, resulting in a more accurate representation of the signal. This is opposite to L2 normalisation, in which high-frequency amplitudes are reduced with respect to low-frequency amplitudes.

Time-localised common oscillatory behaviour in the two time series were identified using wavelet transform coherence (WTC), produced from Eq. C.6. In contrast to the CWT, the wavelet coherence was computed using the analytic Morlet wavelet, for it was the only available option provided by MATLAB at the time. All the same, this was not expected to be a problem. A threshold was set for the phase display, so the black arrows projected on the scalograms are only visible for areas where the magnitude-squared coherence exceeds 0.75. The lead-lag relationship between the two signals at moments of high correlation was determined using the wavelet cross-spectrum (Eq. C.5). Plotting the circular phase, obtained from Eq. C.7, for (pseudo-)periods (or scales) of interest (denoted by λ), revealed the corresponding time evolution of relative lag between the two signals.

Following the $1/e$ rule from Torrence and Compo (1998), for the analytic Morlet wavelet the cone of influence (CoI) is explicitly expressed by $\sqrt{2}a$, where a represents the scale. For the default Morse wavelet the expression changes to $a\sigma$, where σ is the time-domain standard deviation (Lilly, 2017). Since the majority of measurement runs produced at least several h of data, any potential inaccuracies imposed by the CoI, especially for larger periods (or scales) of interest, could be simply overcome by increasing the time span under consideration.

3.6.3 Spanwise variability

The relative variability of saltation intensity as a function of spanwise (i.e., lateral) distance (CV_y) and shear velocity (u_*) was determined following a procedure similar to the ones described in Gares et al. (1996) and Baas and Sherman (2006). First, the coefficient of variation was computed in essentially the same manner as in Eq. 3.6, but instead of taking the standard deviation over the whole array at once, the CV_y was computed for every possible spanwise distance interval. Since the majority of values of Δy allowed for multiple possible combinations, the procedure was repeated for all permutations. Note that for $\Delta y = 0.1$ m there were 31 alternative combinations, whereas for $\Delta y = 3.1$ m there was only one. After CV_y was determined for all spanwise distances ($\Delta y = 0.1, 0.2, \dots, 3.1$ m), the mean was calculated over all permutations per spanwise distance. The obtained mean values of CV_y were then plotted against the corresponding values of the Δ and u_* , after which a was locally-weighted-smoothing linear (plane) regression was generated through the resulting point cloud in 3-D space.

4 Results

In this chapter the results of this study are presented, which are used to answer the research questions in the same order as stated in 2.2.2. Firstly, contour maps of saltation intensity are presented with the main focus on detecting recurring streamer patterns and their dependence on the transport conditions. Not only the collective behaviour of streamers but also that of individual streamers is closely inspected. Secondly, wavelet transform scalograms of instantaneous saltation intensity and horizontal wind speed are presented with the principle aim of identifying common time-varying fluctuations (or variability). The third section covers both uni- and multivariate plots of time-averaged, time-synchronised time series of saltation and airflow characteristics in order to examine their behaviour and potential relationships on a timescale of minutes. Lastly, the relative position on the beach and upwind soil moisture contents are coupled to the saltation and airflow intensities as well as their mutual relationship.

4.1 Contour maps

This section presents a series of spatiotemporal maps of saltation intensity (I) with both horizontal and vertical coverage. These maps are generated from the SDS records following the method described in 3.6.1. They provide the time history of I as recorded by the horizontal sensor array, at 0.1 m from the bed, and by the vertical sensor array, at specified heights stacked above the bed at a single horizontal location (adjacent to the horizontal array; see Fig. 3.3).

4.1.1 Transport patterns

From the vast collection of data, a small selection of short time intervals were selected that roughly cover four different levels of observed transport intensity, ranging from the first detection of saltating grains to the point just before grain impact rates exceeded the processing capacity of the measuring system. Figures 4.3, 4.4, 4.5 and 4.6 present a series of 5.5-s intervals, each featuring more intense transport conditions than the previous, and have been labelled accordingly as *threshold*, *light*, *moderate* and *heavy* transport, respectively. In these figures, the top panel systematically shows a plan view of the saltation system as captured by the horizontal sensor array, while the bottom panel shows a side view of the same system (at the same point in time) as captured by the vertical sensor array. In addition to the information regarding the mean wind conditions measured over the considered time period by the UA, which is provided on top of the upper panel, the total mean of saltation intensity (μ), the spanwise mean of temporal variability (σ) and the temporal mean of spanwise variability (σ_y) for the upper panel are given in the figure caption. It is important to note that the examples discussed below are not directly one-to-one comparable, as most data were acquired on different days and –even throughout the same day– many environmental factors were impossible to be kept constant.

Threshold transport

Driven by a mean horizontal wind speed of just under 7 m s^{-1} , the vertical record (bottom panel) of the first time interval (Fig. 4.3) clearly displays multiple consecutive pulses of saltating sand grains confined to the lowest regions just above the bed. Each of these pulses lasted between 1.2 s and 1.7 s. Together they constituted a relatively thin saltation layer that only occasionally reached the measuring height of the horizontal sensor array (green dotted line), resulting in what appears as a series of low-intensity ($<55 \text{ cnts s}^{-1}$) saltation patches scattered across the map in the top panel. The observed pattern is also reflected in the computed mean values for saltation intensity, as both the temporal and spanwise standard deviations are nearly double the overall mean. Some patches appear isolated, whereas others seem sideways connected to neighbouring patches, which indicates they are either the footprints of a single sideways-migrating saltation cluster or those of shorter multiple contiguous saltation clusters that migrated perfectly streamwise.

Dwindling character

The height evolution of the individual saltation clusters responsible for the patchy appearance in the upper panel of Fig. 4.3 seems to progress in a more or less consistent fashion: a steep increase followed by a much more gradual decline. The first 4.5 s in the bottom panel display three consecutive examples of this behaviour. However, a more clear example of it is shown in Fig. 4.4, which exhibits the passage of a single saltation cluster, whose height development is outlined by the 50-cnts s^{-1} contour. The cluster lasted a total of about 4.5 s and reached its maximum height after just 1.7 s (i.e., 38 % of its lifespan), after which it slowly dwindled over the course of 2.8 s (i.e., 62 % of its lifespan). It must be noted, however, that the base line is taken here at 0.035 m, which is the measuring height of the lowest positioned impact sensor. Actual values with respect to the surface may, therefore, deviate slightly from those presented here. In that case, the leftmost and rightmost angles of the rising and falling part, respectively, suggest that their time distribution may be even more skewed.

Light transport

Slightly more intense transport conditions, driven by a mean wind speed of just over 7 m s^{-1} , are displayed in Fig. 4.4. The bottom panel shows a considerably more developed saltation layer than the one in Fig. 4.3. At the location of the vertical sensor array this layer almost continuously reached the measuring height of the horizontal sensor array marked by the green dotted line. However, the top panel also reveals that this was definitely not the case everywhere along the horizontal span of the SDS. Only right in the middle of the horizontal span a saltation pattern is visible that would be expected from the shown vertical profile. This either implies that only a couple of well-developed and well-isolated streamers incidentally crossed the measuring set-up during the depicted time period, or they were the result of, e.g., dry sand strips or preferential flow paths upwind of the SDS. Spatiotemporal maps of antecedent and subsequent time periods (not shown) do occasionally hint at the possible existence of the latter at the time, as some fixed spots tended to receive more intense saltation pulses more frequently than others. This suspicion was supported by a comparison between the long-term signal means amongst all the impact sensors, which clearly revealed multiple contiguous outliers.

Nevertheless, the overall change of character of saltation transport with respect to the threshold-transport example is evident (Fig. 4.3). The mean values of saltation intensity reveal that the mean and both the variability in temporal and spanwise sense were of equal magnitude, which indicates a relative decrease in variability with respect to the mean with intensifying transport conditions. Furthermore, the previously observed dwindling character of individual saltation pulses is not readily identified in the current example. The saltation layer appears much more continuous with now and then small bumps that do not directly remind of the steep rise/gentle fall recognised previously. Such bumps occasionally resulted into the detection by a single impact sensor of up to 190 cnts s^{-1} at 0.1 m above the bed for up to about 0.3 subsequent seconds.

Moderate transport

Another step up in terms of transport magnitude is captured in Fig. 4.5, which was driven by a mean wind speed of just over 9 m s^{-1} . Depicting another time interval from the same day as the one in Fig. 4.4, environmental conditions were not much different other than the wind speed. Perhaps most striking is that saltating grains (at intensities $\geq 30 \text{ cnts s}^{-1}$) were detected most of time by the majority of horizontally configured impact sensors, which clearly hints at the development of a more consistent saltation cloud. Only now and then a couple of impact sensors did not detect any saltating grains for periods usually no longer than 0.5 to 1 s. In addition, saltation clusters of up to 260 cnts s^{-1} and maintaining that intensity for up to 1 s at 0.1 m above the bed were not uncommon.

The change in saltation transport pattern is again reflected in the mean saltation values, which, apart from being significantly higher (96 cnts s^{-1} v. 26 cnts s^{-1}), show relative variability to have decreased even further. In the case of temporal variability this is towards half the value of the overall mean saltation intensity, whereas the spanwise variability remained slightly higher, possibly for the same reasons mentioned earlier regarding preferential flow paths.

Also in this example the dwindling character of individual saltation pulses exhibited in Fig. 4.2 is mostly not apparent. Yet, a distinct example can be seen after about 0.8 s and lasting about 1 s. The saltation layer also reached greater heights of up to 0.24 m above the bed at some points in time, but on average the difference to the previous example (i.e., Fig. 4.4) was negligible.

Heavy transport

Figure 4.6 shows an example of what a saltation transport pattern looked like under very potent transport conditions. The saltation cloud appears fully developed, occupying the full detection field inside the given time interval. Just as in the previous two examples (i.e., Figs. 4.4 and 4.5) clusters of relatively high saltation intensity were found superimposed on or embedded in the broader saltation cloud. Again, variability shows a further drop relative to the mean saltation intensity, as is revealed by the mean saltation values, which is in accordance with the overall picture visible in the upper panel. At the measuring height of the horizontal sensor array the saltation intensity never dropped below 50 cnts s^{-1} , while more intense saltation clusters marked by intensities exceeding 200 cnts s^{-1} lasted up to 1.3 s.

Remarkably, while the type of saltation transport pattern clearly seems to depend on the mean wind speed, this is, rather paradoxically, not necessarily true for the rate of saltation, as can be concluded by comparing Figs. 4.6 and A.5. Even though the

transport pattern shown in the upper panel of Fig. A.5 appears very similar to the one in Fig. 4.6 (heavy transport), the intensity of the underlying transport conditions is much more like in Fig. 4.4 (i.e., light transport).

It also becomes clear that these transport conditions mark the limit as to what saltation intensity the SDS was still able to properly resolve. Even more extreme conditions, such as depicted in Fig. A.6 ($\bar{U} > 10 \text{ m s}^{-1}$), unavoidably led to severe overload symptoms at the impact sensors occupying the lowest positions, among which the ones at the crucial observation height of the horizontal sensor array, thereby seriously compromising the reliability of the acquired data.

Streamer length scales

One approach to identifying relatively intense saltation clusters (or streamers) embedded in a large saltation cloud was by detrending a generated saltation-intensity contour map. An example of such is given in Fig. 4.7, which displays the original and detrended versions of the same contour map in top and bottom panel, respectively. Transport conditions were similar to those in Fig. 4.6, as it concerns a time interval of just 8 min earlier. The use of a dynamic threshold, defined here as the sum of the spanwise mean and half the spanwise standard deviation, appeared a convenient way of outlining the relatively intense parts of the saltation cloud that may be interpreted as embedded streamers.

Visual examination of the outlined saltation clusters reveals that, at 0.1 m from the bed, their widths ranged from 0.1 to 0.3 m, while sometimes lasting up to 1.8 s. It must be noted here that, as could be seen from Fig. 4.2, below the detection range of the horizontal sensor array streamers were likely to extend beyond these timescales. Nonetheless, there is quite a differentiation in sizes of the outlines, which are most notable in the x -direction. Some of the clusters appear to have lasted considerably longer, hence be of much greater length, than others.

Within the span of 3.1 m up to about 8 individual streamers can be observed side by side simultaneously, which means that embedded streamers occurred approximately every 0.39 lateral metre. The centre-to-centre spacing between two neighbouring streamers varied between zero (i.e., they were touching) and 0.5 m. Yet, the most common observable spacings are 0.3 m and 0.2 m, of which the latter occurs when out of three adjacent impact sensors only the middle one receives no threshold-exceeding signal (i.e., the minimum spacing resolvable by the measuring set-up). The outlines also clearly show that streamers do not necessarily follow perfect streamlines, but instead may move laterally up to 0.8 m over the course of less than 1 s as, for instance, can be seen from the streamer that appeared after 2.5 s (see bottom right corner of Fig. 4.7). This degree of mobility probably also occasionally led to the merging and separation of (neighbouring) streamers resulting in some of the visible arch-like outlines.

In order to associate length scales to the streamer timescales found by examining these contour maps, the migration velocity of streamers must be known. Given the lack of more sophisticated measuring equipment to determine true velocities, a simple technique including the tracking, tracing and timing of a passing streamer was used to obtain a decent estimation. The slightly wet conditions on 11 October allowed for easier visual inspection of streamers and streamer motion due to the enhanced contrast between the transport phenomena and the beach surface over which they flow. Two time intervals capturing the starting and end point of the trajectory of the tail of an individual streamer are shown in Fig. 4.1. Between 15:20:00 MET and 15:28:00 MET the mean wind speed, as measured by the lowest cups (at 0.20 m

from the bed) of the cup-anemometer tower positioned closest to the shore line, was $8.49 \pm 0.62 \text{ m s}^{-1}$. The groundwater pole and cup-anemometer tower, respectively serving as starting and end point, were distanced 10.90 m from each other, as determined from GPS data. The streamer's tail clocked in at a little over 4 s to cover that interval. Disregarding any potential stretching or retardation of the streamer body, that equates to a streamwise streamer velocity of approximately 2.73 m s^{-1} , which matched the wind speed at 0.078 m from the bed, acquired by extrapolating the green log wind profile in Fig. A.4.

By using the migration speed derived from Fig. 4.1, the streamer timescales derived from Fig. 4.7 can be translated into length scales. For example, the length at 0.1 m from the bed of the longest (embedded) streamers then turns into $(1.8 \text{ s} \times 2.73 \text{ m s}^{-1}) = 4.9 \text{ m}$, while some of the shortest were just $(0.2 \text{ s} \times 2.73 \text{ m s}^{-1}) = 0.5 \text{ m}$. For estimations of these lengths at the height of the bed their values might even be extrapolated using the form factor of the saltation cluster displayed in Fig. 4.2. In addition, the individual saltation pulses displayed in the vertical profile in Fig. 4.3 would each obtain a length of about $(1.5 \text{ s} \times 2.73 \text{ m s}^{-1}) = 4.1 \text{ m}$ seen from 0.035 m from the bed. However, the migration speed and therefore length scales are merely tentative values, for they are subject to a considerable degree of uncertainty due to the rough estimation of the former. Therefore, they should only be considered as approximations of their true order of magnitude. Extrapolation using a form factor, which has not yet been validated for other transport conditions, would only further increase the error margin.

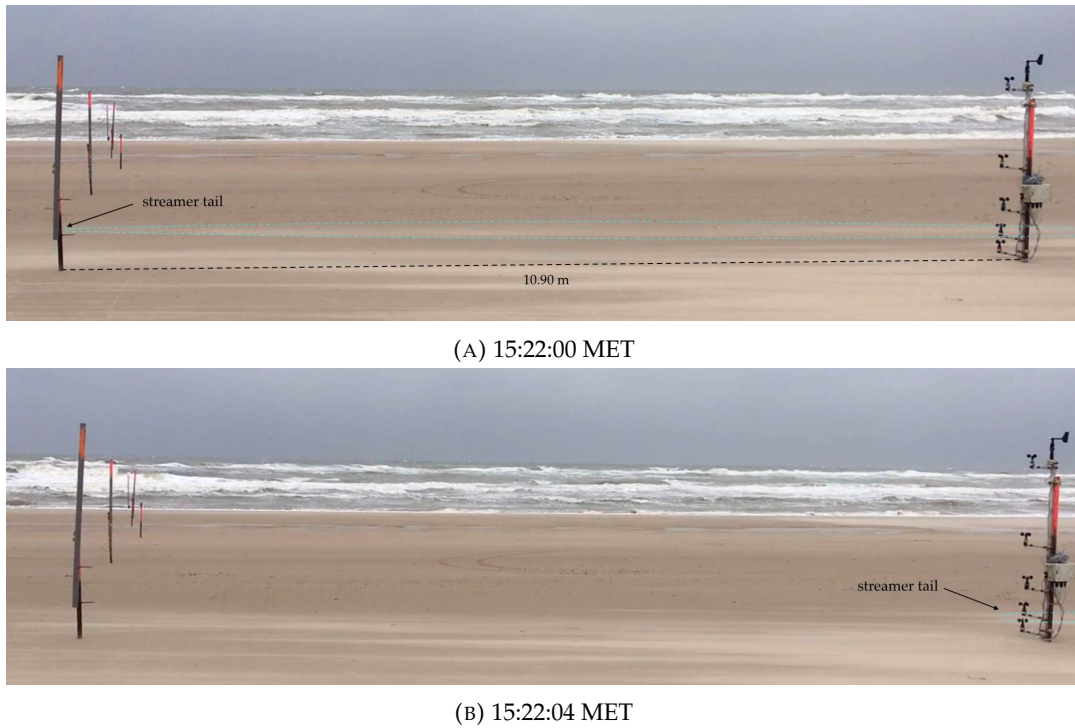


FIGURE 4.1: Snapshots from footage of a passing streamer (delineated by cyan dashed lines) propagating from left to right at (A) 15:22:00 MET and (B) 15:22:04 MET (MET). The distance between the reference points is 10.90 m, as determined from GPS measurements.

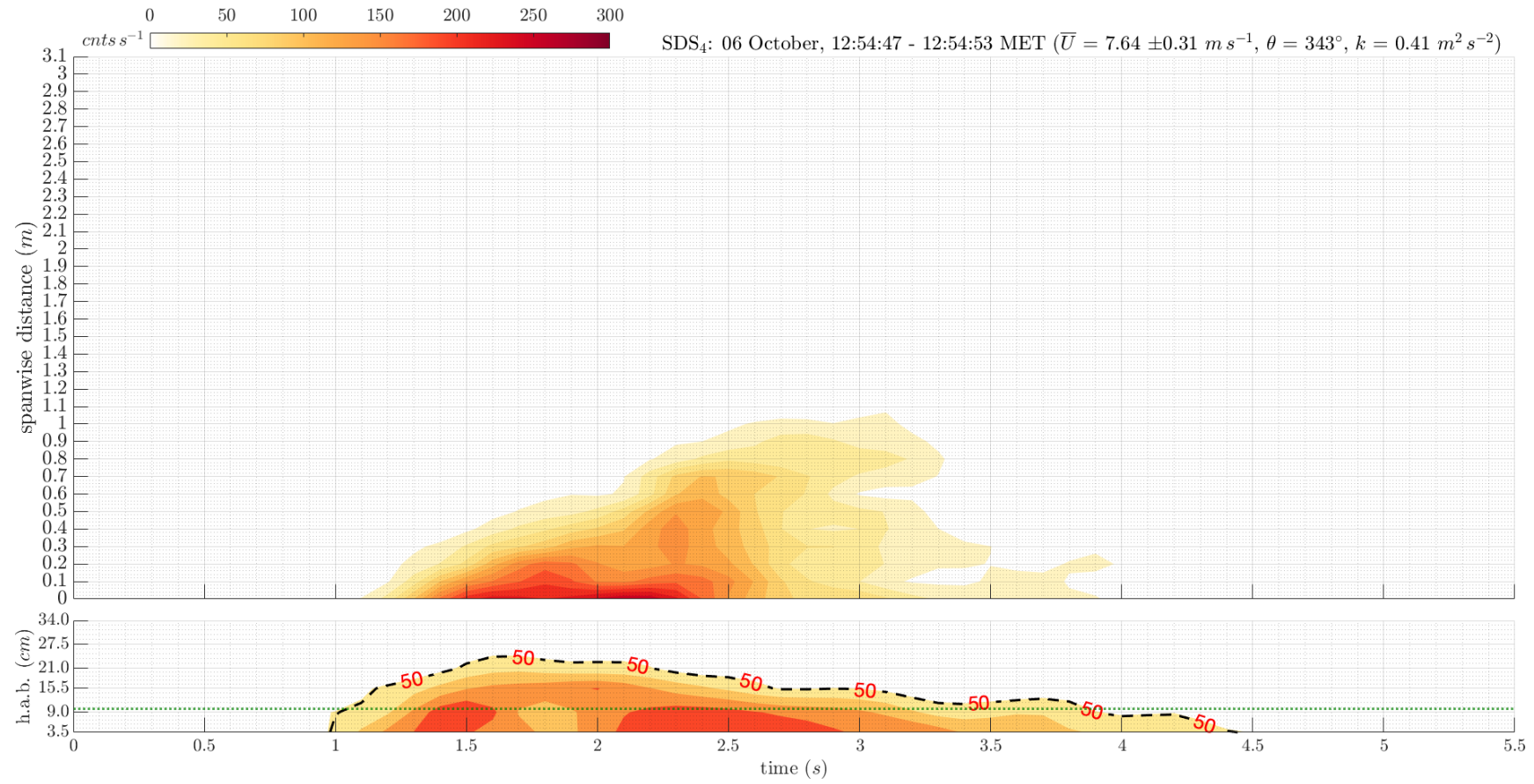


FIGURE 4.2: Contour maps of saltation intensity as recorded by the (top) horizontal and (bottom) vertical sensor arrays of SDS₄. Maps have been smoothed using a Gaussian filter ($window = 5$) in the time domain. Horizontal green dotted line in the lower panel denotes the lower detection-height limit of the impact sensors of the horizontal array. Black dashed line denotes the 50- cnts s^{-1} contour. Metadata and UA data are listed on top.

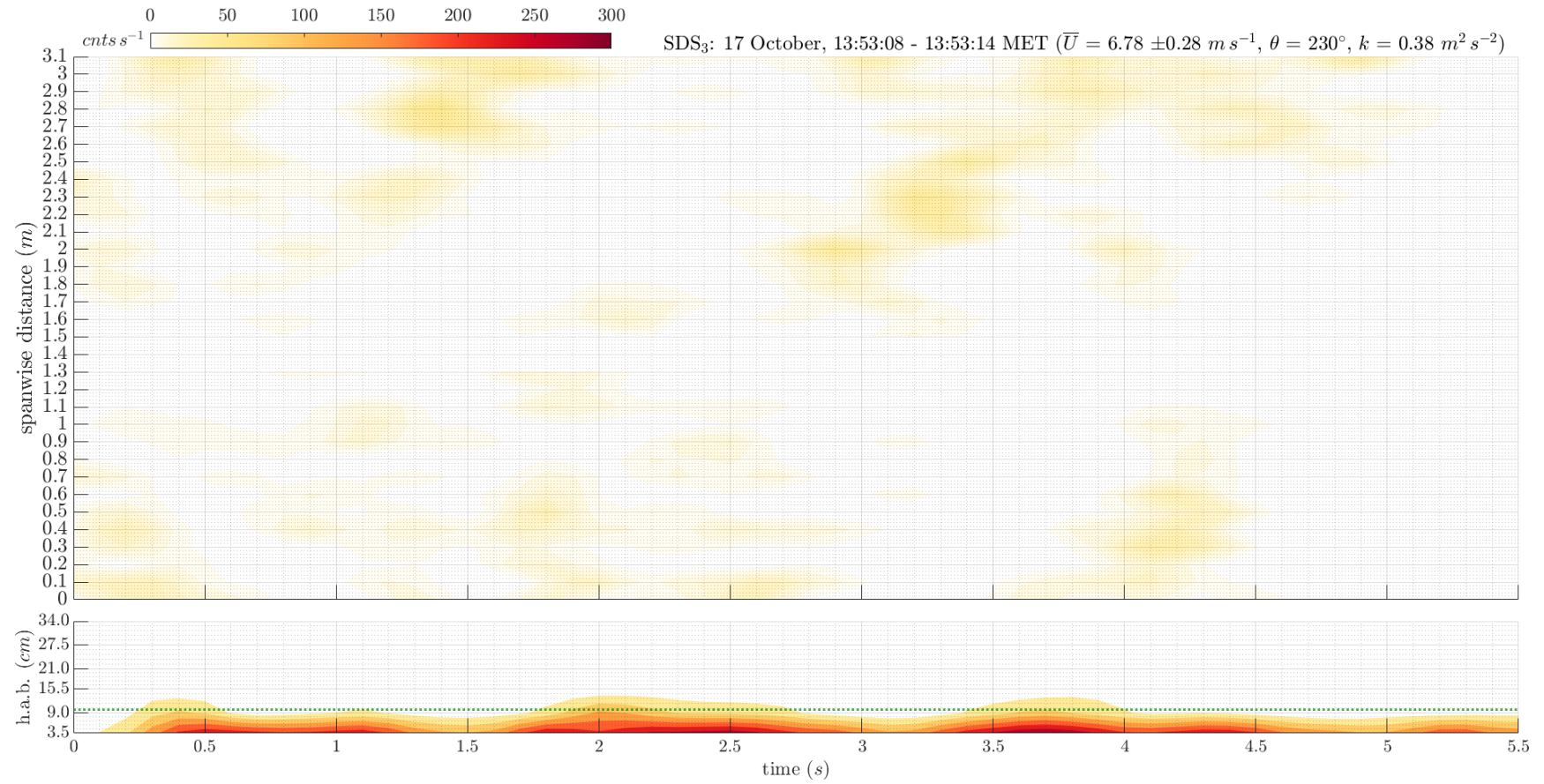


FIGURE 4.3: Contour maps of saltation intensity as recorded by the (top) horizontal and (bottom) vertical sensor arrays of SDS₃. Maps have been smoothed using a Gaussian filter (*window* = 5) in the time domain. Horizontal green dotted line in the lower panel denotes the lower detection-height limit of the impact sensors of the horizontal array. Metadata and UA data are listed on top. Mean saltation values: $\mu = 5 \text{ cnts s}^{-1}$, $\sigma = 9 \text{ cnts s}^{-1}$ and $\sigma_y = 9 \text{ cnts s}^{-1}$. Note the defective sensor (#15) at 1.4 m.

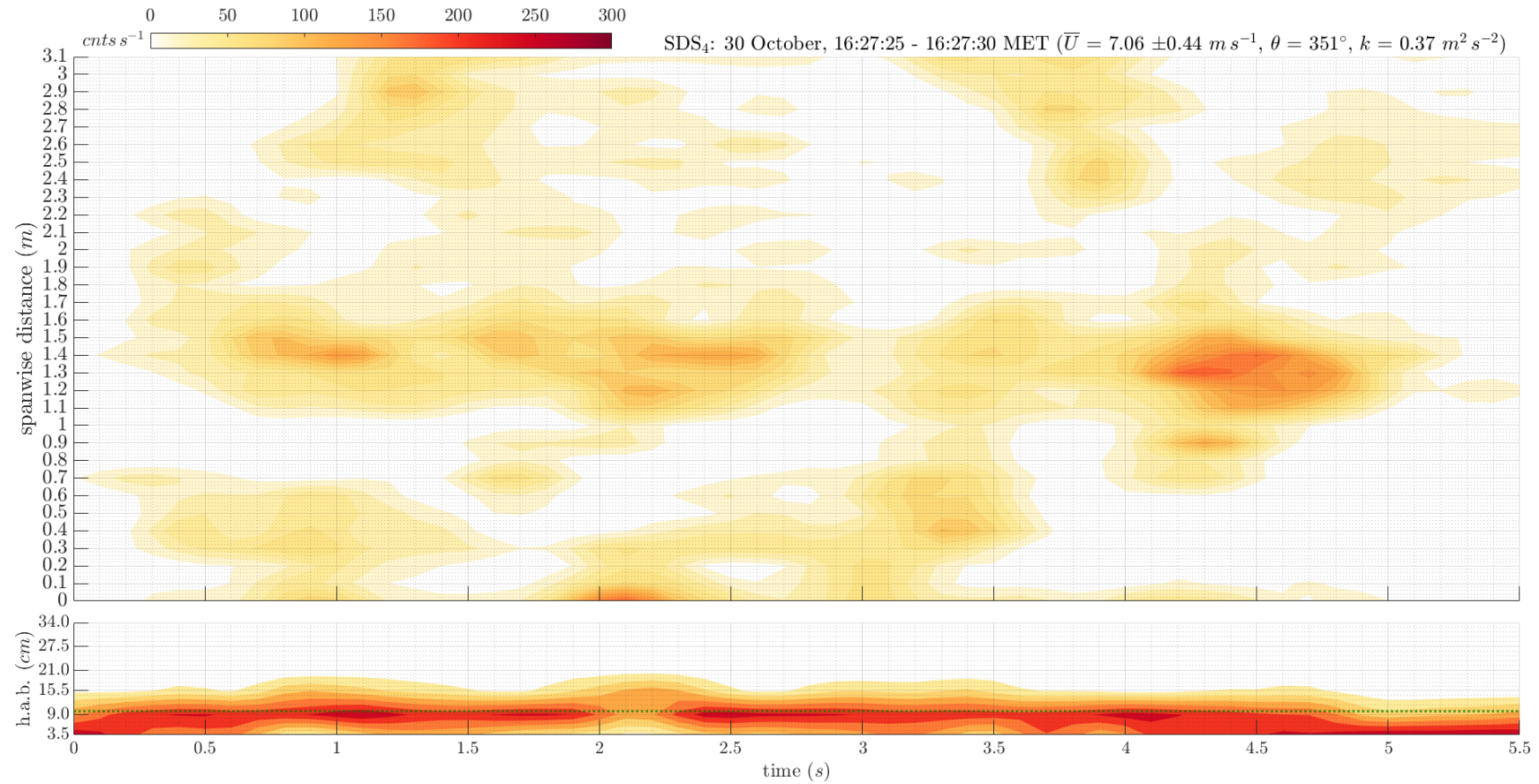


FIGURE 4.4: Contour maps of saltation intensity as recorded by the (top) horizontal and (bottom) vertical sensor arrays of SDS4. Maps have been smoothed using a Gaussian filter (*window* = 5) in the time domain. Horizontal green dotted line in the lower panel denotes the lower detection-height limit of the impact sensors of the horizontal array. Metadata and UA data are listed on top. Mean saltation values: $\mu = 26 \text{ cnts s}^{-1}$, $\sigma = 27 \text{ cnts s}^{-1}$ and $\sigma_y = 29 \text{ cnts s}^{-1}$.

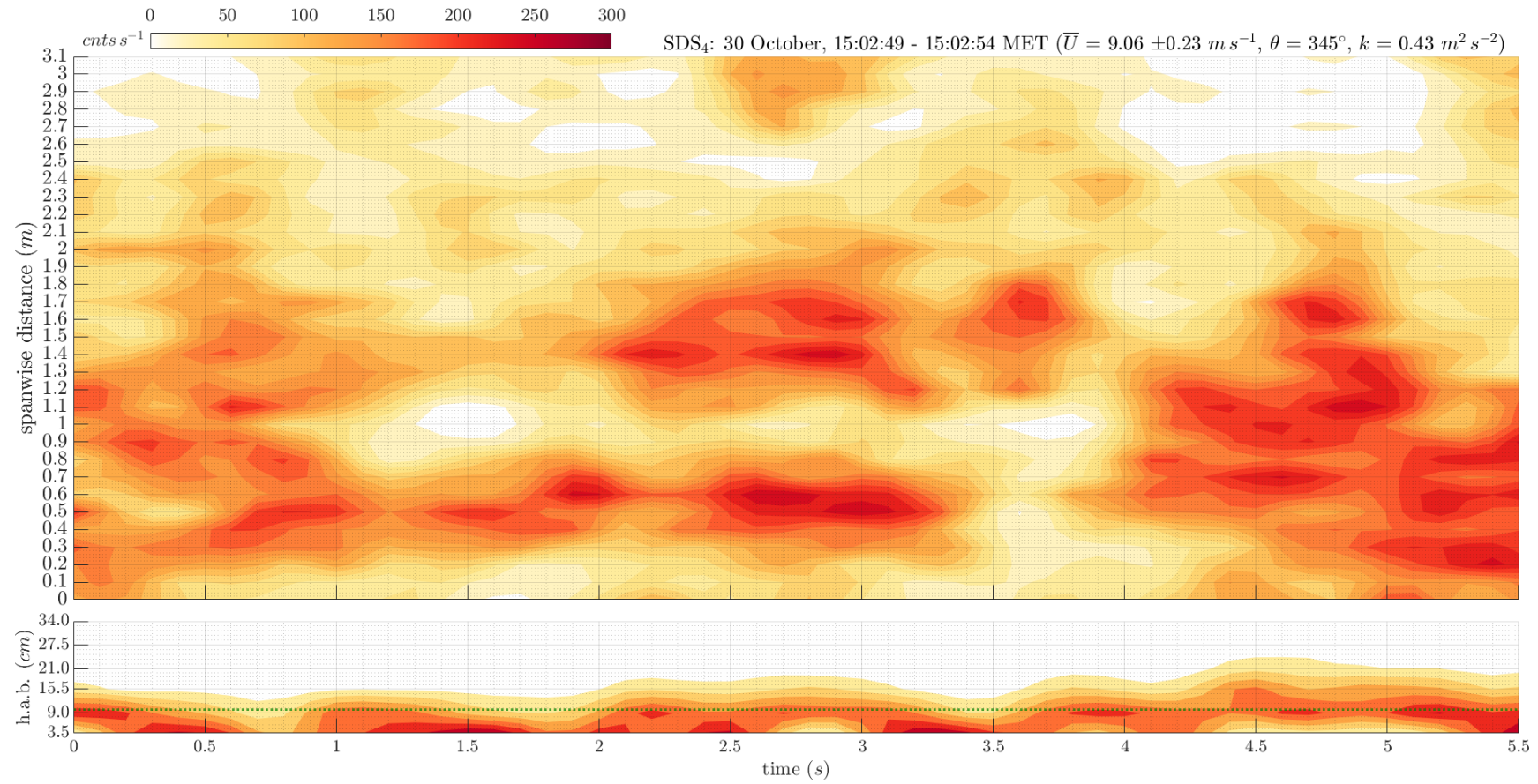


FIGURE 4.5: Contour maps of saltation intensity as recorded by the (top) horizontal and (bottom) vertical sensor arrays of SDS₄. Maps have been smoothed using a Gaussian filter (*window* = 5) in the time domain. Horizontal green dotted line in the lower panel denotes the lower detection-height limit of the impact sensors of the horizontal array. Metadata and UA data are listed on top. Mean saltation values: $\mu = 96 \text{ cnts s}^{-1}$, $\sigma = 55 \text{ cnts s}^{-1}$ and $\sigma_y = 68 \text{ cnts s}^{-1}$.

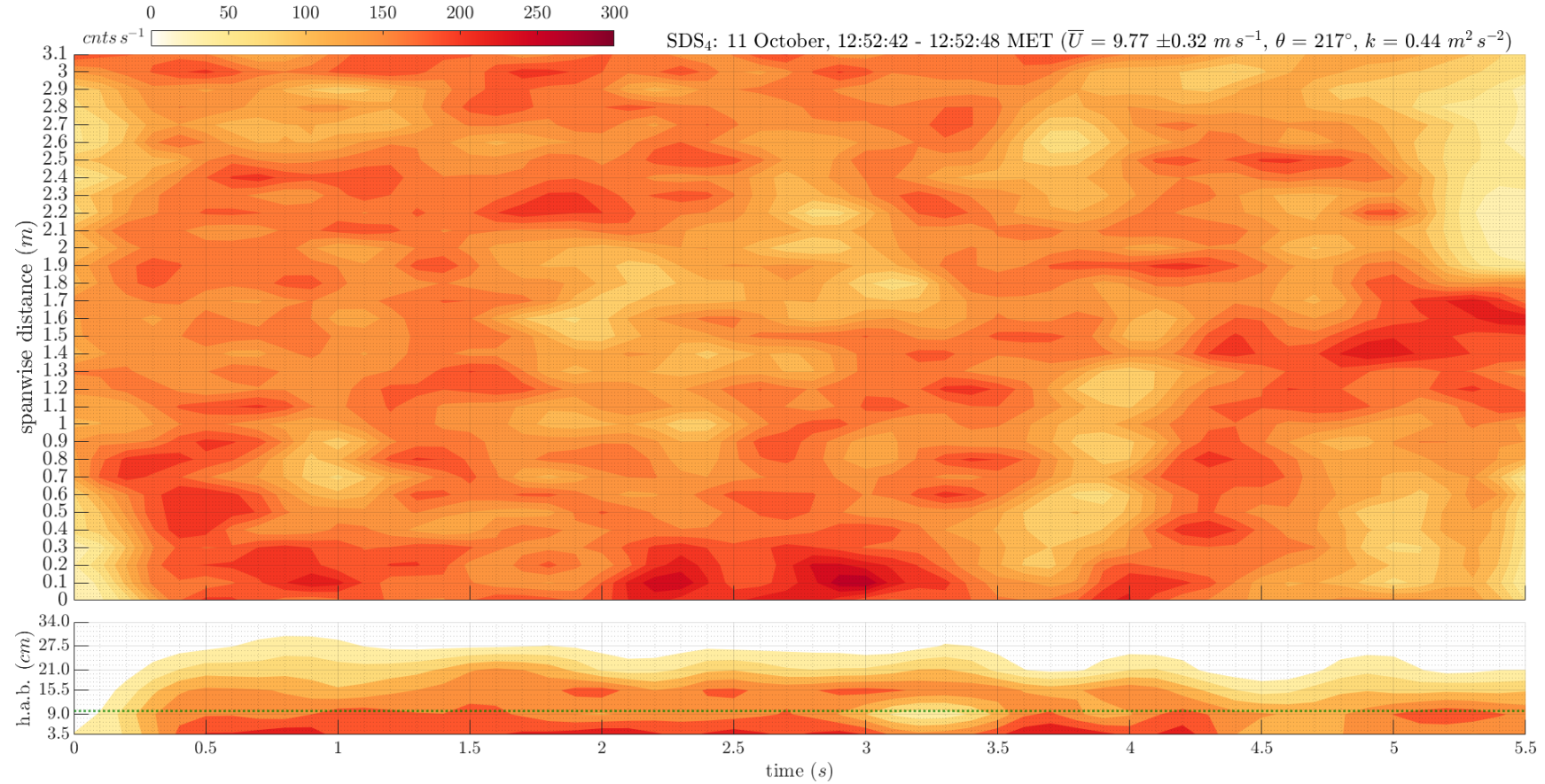


FIGURE 4.6: Contour maps of saltation intensity as recorded by the (top) horizontal and (bottom) vertical sensor arrays of SDS₄. Maps have been smoothed using a Gaussian filter (*window* = 5) in the time domain. Horizontal green dotted line in the lower panel denotes the lower detection-height limit of the impact sensors of the horizontal array. Metadata and UA data are listed on top. Mean saltation values: $\mu = 153 \text{ cnts s}^{-1}$, $\sigma = 47 \text{ cnts s}^{-1}$ and $\sigma_y = 43 \text{ cnts s}^{-1}$.

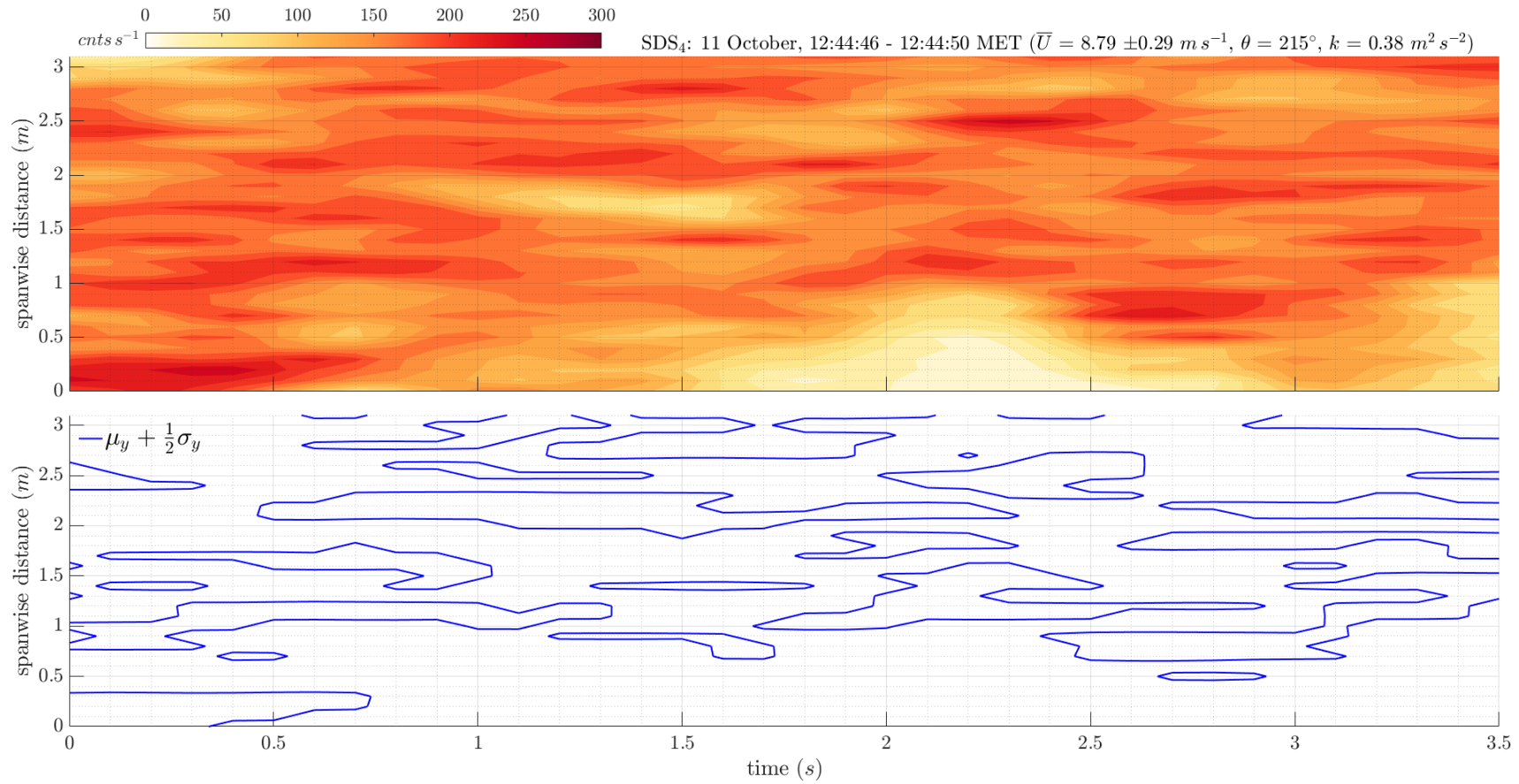


FIGURE 4.7: (top) Contour map of saltation intensity as recorded by the horizontal sensor array of SDS₄. Map has been smoothed using a Gaussian filter ($window = 5$) in the time domain. Metadata and UA data are listed on top. (bottom) Detrended version of the upper map using threshold $(\mu_y + \frac{1}{2}\sigma_y)$ in order to obtain a better visual outline of the streamers embedded in the extensive saltation cloud. Mean saltation values: $\mu = 157 \text{ cnts s}^{-1}$, $\sigma = 47 \text{ cnts s}^{-1}$ and $\sigma_y = 51 \text{ cnts s}^{-1}$.

4.1.2 Saltation and airflow coupling

Figure 4.8 presents yet another set of saltation-intensity contour maps but this time considering a much longer time interval of 40 s. In addition to the horizontal (top) and vertical (middle) saltation profiles, it also provides the horizontal wind speed (both instantaneous and a 3-s average) and direction in a third (bottom) panel. Consequently, even though the figure loses the level of detail required to discern individual streamers, it instead provides insight into the larger-scale behaviour of saltation transport (manifested as streamers) with respect to the contemporaneous wind characteristics.

The depicted ‘events’ were driven by transport conditions similar to those underlying Fig. 4.6, even though the level of turbulence intensity (k) was considerably greater ($1.04 \text{ m}^2 \text{ s}^{-2}$ v. $0.44 \text{ m}^2 \text{ s}^{-2}$). The top panel displays the passage of two waves of continuous heavy saltation transport separated by a brief period of about 7 s of virtually no transport, roughly coinciding with a momentary change in wind direction and reduction in wind speed, hence shear velocity. The small but inevitable rotation of the angle of wind incidence (black dotted line) probably also led to the SDS not being perfectly aligned perpendicularly to the transport direction any longer, which is reflected in the ~ 2.5 -s time discrepancy between the arrival of the second oncoming saltation wave front at either ends of the horizontal sensor array.

At $t = 8.7$ s the 3-s running mean (blue solid line) of u commenced a gradual decline from a high of roughly 9.06 m s^{-1} to a low of 6.21 m s^{-1} over the course of about 8.6 s, which was accompanied —or actually even preceded— by a likewise gradual drop in the height of the saltation layer (middle panel). The latter completely dropped below the minimum detection height of the vertical sensor array (i.e., 0.035 m from the bed) at $t = 14.6$ s, which also roughly marks the point at which the entire horizontal sensor array stopped detecting saltating grains altogether (save for a few ‘lost’ streamers). Interestingly, no evident gradual decline in mean saltation intensity over the horizontal span (μ_y) at 0.1 m from the bed was observed mirroring the ongoing decline in height of the saltation layer. Instead, it remained relatively constant (e.g., Fig. 4.9a) at a level of $\sim 170 \text{ cnts s}^{-1}$ up to 0.7 s before the transport break. Note that the mentioned fall in saltation-layer height here is fundamentally different from the dwindling passage of a single saltation pulse discussed earlier in 4.1.1, since the current example instead represents a series of such pulses closely following/attached to one another (i.e., on a larger scale).

The moment streamers along the horizontal span started to collectively fall below the detection range ($t = 14.6$ s), defined here as the point where $\mu_y < 45 \text{ cnts s}^{-1}$, the co-located UA measured a u of 7.60 m s^{-1} (blue solid line). Using the instantaneous version of Eq. 3.19, this wind speed translates to a shear velocity (u_*) of 0.45 m s^{-1} . The moment streamers emerged again within the detection range array-wide ($t = 22.0$ s), u had a value of 7.84 m s^{-1} , which in turn translates to a u_* of 0.46 m s^{-1} . Thus, there appears no substantial difference between the computed shear velocities associated with the sudden break and subsequent resumption of the continuous heavy saltation transport. Moreover, the saltation layer seemingly responded without delay to the rapid recovery of u (commencing at $t \approx 20.5$ s) and even approached its former high ($t = 7.1$ s) within the course of just 2 s.

Moving away from the larger-scale patterns, the wavy shape of the saltation layer could be arguably said to roughly mirror the instantaneous u (red solid line), which is perhaps most apparent in the last 5 s. In particular during that time interval the instantaneous time series seems to give a much better reflection of what happened to the saltation layer than does the smoothed time series.

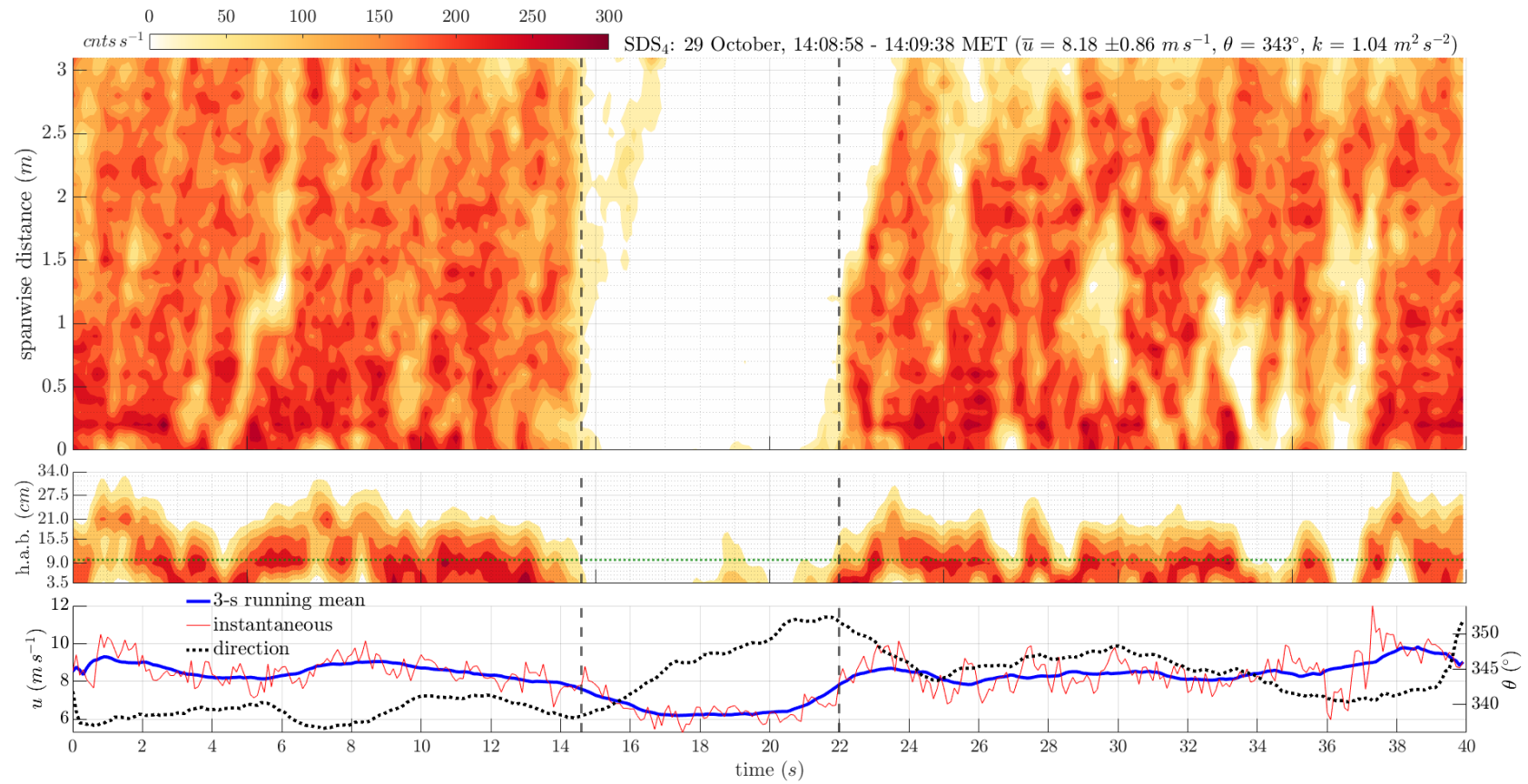


FIGURE 4.8: Contour maps of saltation intensity as recorded by the (top) horizontal and (middle) vertical sensor arrays of SDS4. Maps have been smoothed using a Gaussian filter ($window = 5$) in the time domain. Vertical dashed lines delineate the considered transport gap. Horizontal green dotted line denotes the lower detection-height limit of the impact sensors of the horizontal array. Bottom panel shows the concurrent time series of horizontal wind speed and direction measured by UA4. Metadata and UA data are listed on top.

4.2 Wavelet transform

The previous section concluded with a short case study, in which the coupling between saltation intensity and airflow was briefly examined on the basis of contour maps and simple time-history graphs. This section will delve further into this particular coupling by means of a technique based on wavelets (see Appx. C for more details), which may provide new insights into both independent and common time-varying fluctuations (or patterns) of the two signals (or variables) of interest.

4.2.1 Short timescale

Figure 4.9 shows the normalised time series of instantaneous saltation intensity (I) and (unsmoothed) horizontal wind speed (u) of the same time interval as in Fig. 4.8 together with the results generated after application of the continuous wavelet transform (CWT). To ensure the highest degree of association, hence greatest explanatory power, the measured airflow fluctuations were compared with the saltation-intensity fluctuations averaged over the three closest contiguous impact sensors upwind of the UA (i.e., $I = \mu_{p=5:7}$). The CWT results are presented in so-called scalograms, which depict the energy-density (or power-density) distribution over a range of scales through time. In each scalogram, time (t) is represented on the x -axis and the effective (pseudo-)period (λ), converted from the scale of the fitted daughter wavelet, on the logarithmic y -axis, while the corresponding colour bar indicates the magnitude scaling of the CWT coefficients.

Remarkably, none of the CWT scalograms reveal any continuous high-energy bands. Virtually no long-lived, strongly representative periodicity was detected in either of the signals by the range of applied wavelet functions, which indicates a high degree of 'non-stationarity' or 'randomness' in both their behaviours. For instance, in the CWT scalogram of saltation intensity (Fig. 4.9b) the very small and short-lived energy elevations at temporal scales of <1 s are probably reflections of incidental streamers. Nonetheless, a number of short-lived spikes in magnitude of the CWT coefficient indicate fluctuations in I of ~ 1 s that lasted for about 5 s (Fig. 4.9b) and fluctuations in u of ~ 0.5 s that lasted for about 2 s (Fig. 4.9d), which roughly coincide with the time interval pointed out previously in the last paragraph of 4.1.2. Both CWT scalograms further show longer-lived bands of higher energy in fluctuations of ~ 5 s, which seem to roughly coincide with the moment of, and hence may be associated to, the transport break (see Figs. 4.9a and 4.9c).

The scalogram in Fig. 4.10 shows the wavelet transform coherence (WTC) generated from the two CWT scalograms. Note that the colour bar now indicates the magnitude-squared coherence, a measure of how well the two signals are correlated. At the 'locations' of significance (i.e., $R^2(a, b) > 0.75$), black arrows signify the phase relation between the two signals. In addition, provided that $R^2 > 0.75$ and the concerning area lies outside the CoI, time series of coherence phase difference (CPD) are given for three selected values of λ , together with their corresponding average time lag converted from the average circular phase.

Despite the lack of any strongly representative periodicities in either of the corresponding CWT scalograms, the WTC scalogram identifies a large band covering the entire observation interval and comprising a range of periods (>10 s) at which I and u appear to be highly coherent. The uniform direction in which the phase arrows are pointing substantiate the suspicion of coherent oscillatory behaviour at these timescales. Two time series of CPD corresponding to values of λ that lie within the coherent range reveal that u led I by almost 0.5 s in the case of fluctuations of 10 s,

whereas this decreased to a mere 0.15 s for fluctuations of 17 s. Disregarding any of the very short-lived areas, there is one more relatively small area within the last 10 s indicating coherent oscillatory behaviour (see also phase arrows) lasting for about 7 s, and which roughly coincided with the energy spikes in the CWT scalograms. The time series of CPD corresponding to a period intersecting this area ($\lambda = 4$ s) reveals that on this timescale I lagged about 0.58 s behind u (see Figs. 4.10c).

The observed lags for $\lambda \leq 10$ s are in accordance with the lags found by additionally conducted simple cross-correlation analysis, which revealed an average (median) lag of 0.5 s corresponding to the highest correlation coefficients found between (unsmoothed) u and μ_y for all three SD systems (see Table B.1). It must, however, be noted that the overall mean of the correlation coefficient ($R_{mean} = 0.63$) did not score convincingly high, while values of R also varied substantially across the various measurement runs.

4.2.2 Long timescale

Figure 4.11 shows the WTC scalogram generated from the CWT scalograms in Fig. A.7, which are from a time interval that extends from half an hour before the events depicted back in Fig. 4.3 up to half an hour afterwards. It teaches that I - u coupling at periods of the order of 10 s of seconds, as established in Fig. 4.10, may still be considered incidental on timescales of an hour (e.g., Fig. 4.11c). Only at periods greater than, say, 300 s the coupling appears truly long-lived. Remarkably, the CPD time series in Figs. 4.11b and 4.11a show u to lag behind I with about 1 s. However, relative to the timescales these lags can be considered negligible, as u and I are practically in phase. These findings show that, at least for the combination of measuring set-up and study site in this study, the coupling between I and u is best studied using a time-averaging scale greater than 300 s or, in the case of much shorter timescales and if checked beforehand, greater than 10 s.

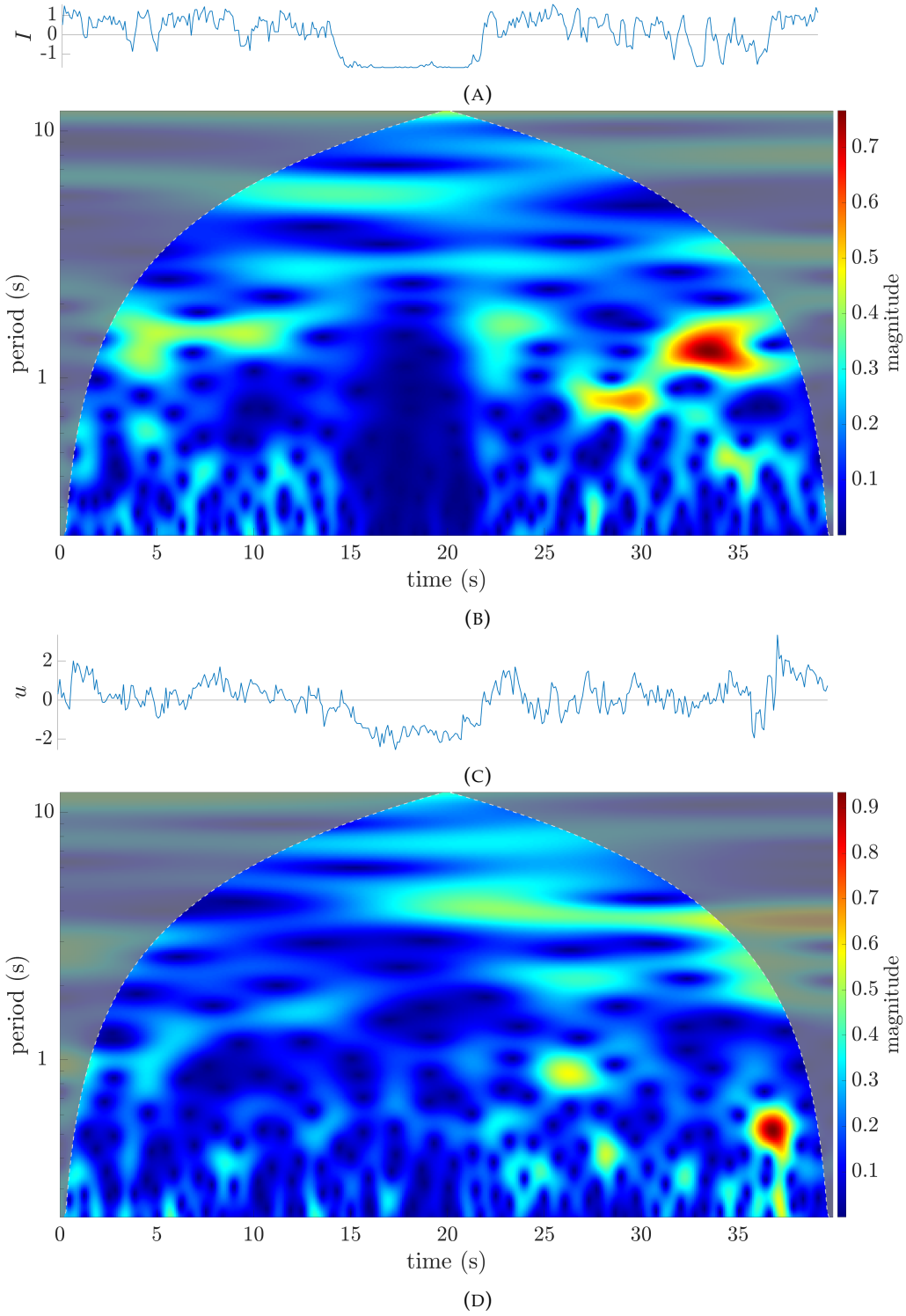


FIGURE 4.9: Time series of normalised (A) saltation intensity and (B) horizontal wind speed, and respective CWT scalograms (B) and (D). Time period: 29 October from 14:08:58 to 14:09:38 MET. Mother: analytic Morse wavelet with $\gamma = 3$ and $P^2 = 60$. Instruments: SDS₄ and UA₄. Conditions: $\bar{u} = 8.18 \pm 0.86 \text{ m s}^{-1}$, $\theta = 343^\circ$, $k = 1.04 \text{ m}^2 \text{ s}^{-2}$.

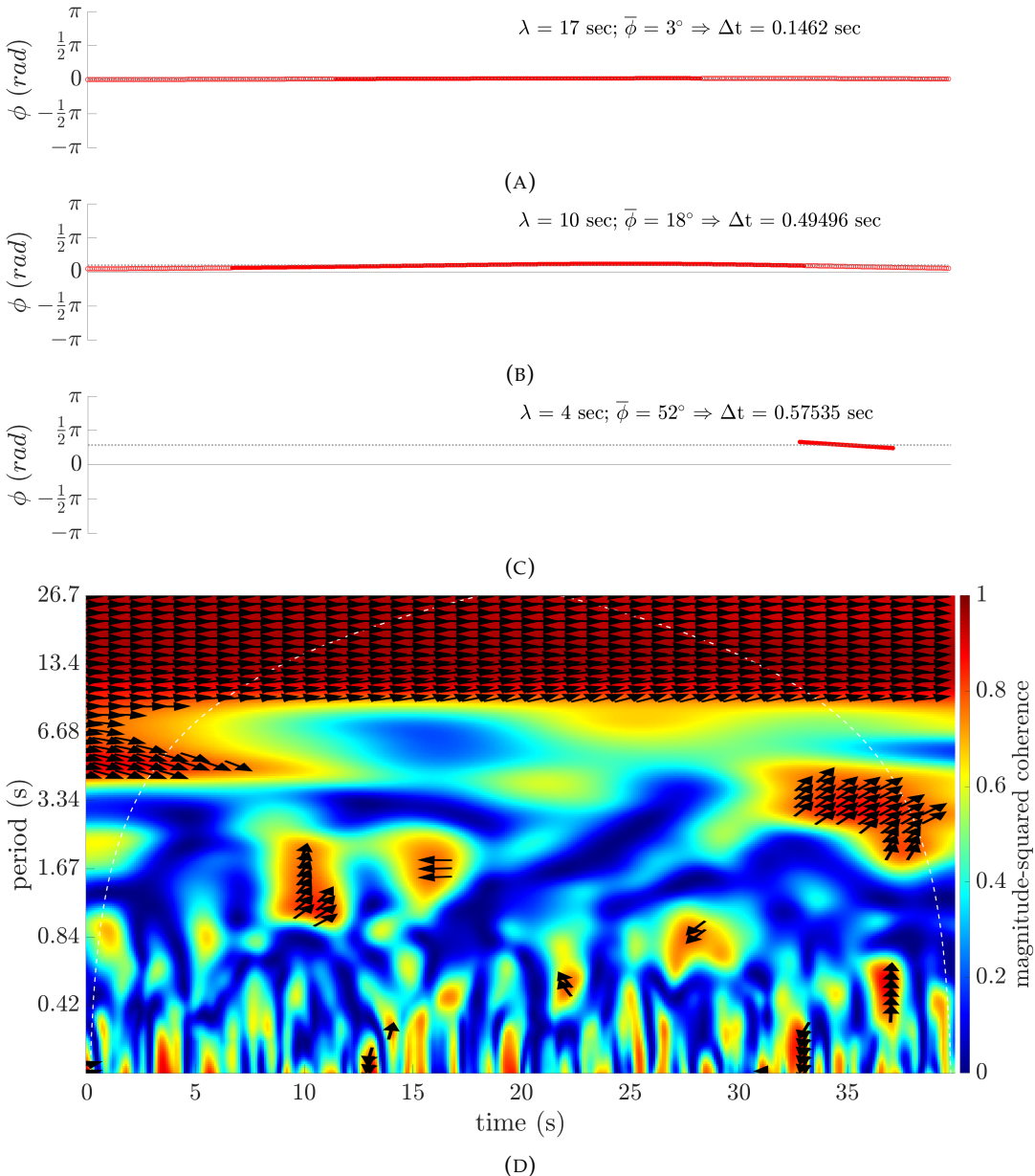


FIGURE 4.10: (D) WTC scalogram corresponding to Fig. 4.9. Mother: analytic Morlet wavelet. White dashed line delineates the CoI. Black arrows signify the local relative phase on the unit circle in areas for which $R^2(a, b) > 0.75$, where an upward-pointing arrow indicates a quarter-cycle lag of I with respect to u . Following the same criterion, time series of CPD are displayed for $\lambda =$ (A) 17 s, (B) 10 s and (C) 4 s. Red (blue) colour indicates that I (u) lags behind. Filled (unfilled) data markers are outside (inside) the CoI. Information is given on the time-averaged relative phase (grey dotted line), which is also converted to a time lag.

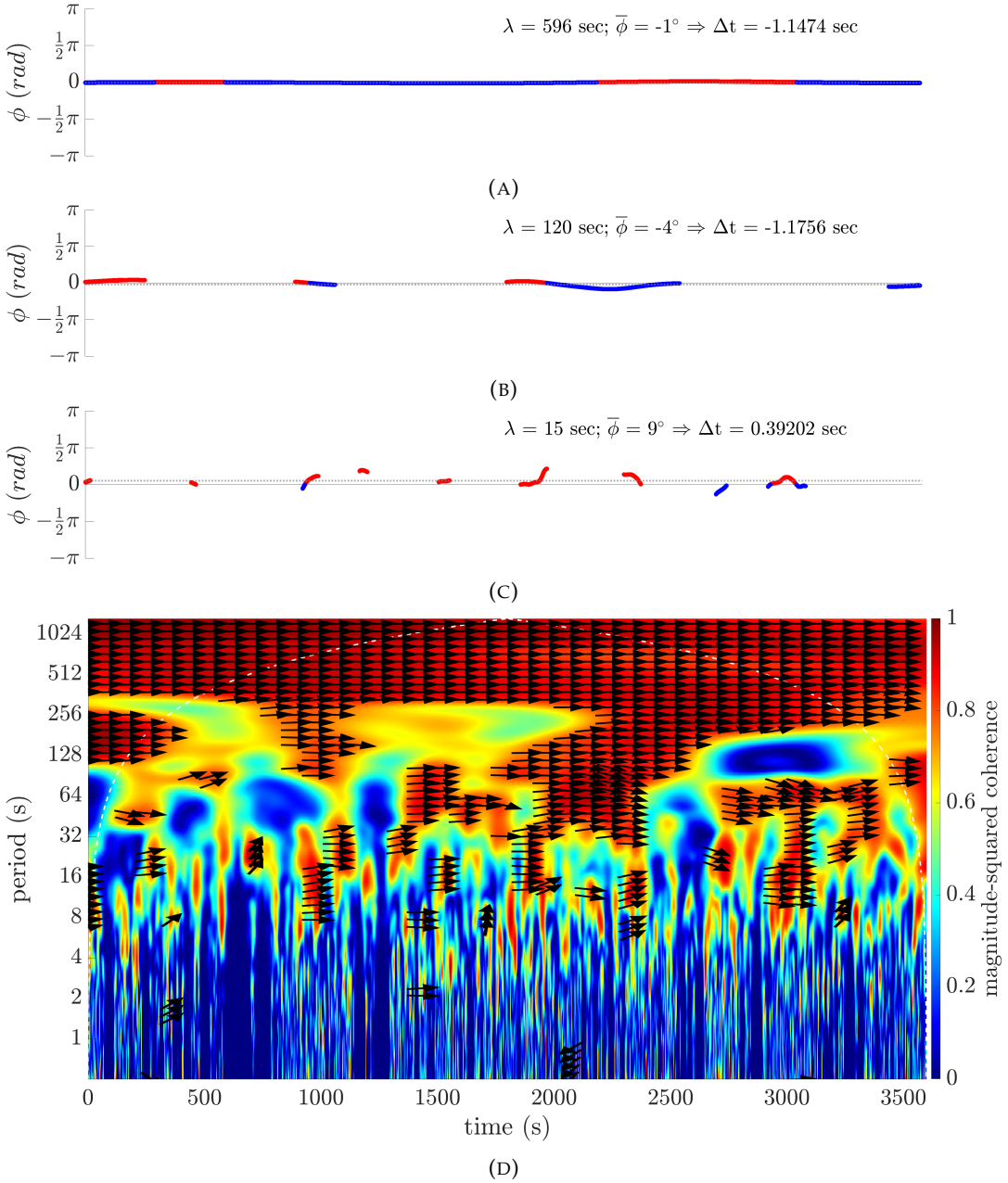


FIGURE 4.11: (D) WTC scalogram corresponding to Fig. A.7. Mother: analytic Morlet wavelet. White dashed line delineates the CoI. Black arrows signify the local relative phase on the unit circle in areas for which $R^2(a, b) > 0.75$, where an upward-pointing arrow indicates a quarter-cycle lag of I with respect to u . Following the same criterion, time series of CPD are displayed for $\lambda =$ (A) 596 s, (B) 120 s and (C) 15 s. Red (blue) colour indicates that I (u) lags behind. Filled (unfilled) data markers are outside (inside) the CoI. Information is given on the time-averaged relative phase (grey dotted line), which is also converted to a time lag.

4.3 Trend analysis

Up to now the focus has been mainly on comparing instantaneous measurements. In this section the focus will shift to comparing time-averaged measurements in order to find trends and patterns that exist on longer timescales and may therefore be of higher relevance to conventional long-term sediment transport modelling. Temporal means of saltation intensity were computed according to Eq. 3.1. Adopting the findings from the WTC scalograms in 4.2 regarding the strongest coherence between I and u , the majority of cases in this section will consider 10-min temporal means, which were generated using bin size $N = 600$. Subsequently, these temporal means were often averaged over the horizontal span (Eq. 3.4), which will be represented by the symbol $\bar{\mu}_y$.

4.3.1 Conditional statements

In an effort to cope with the complexity of the physical interrelationships inherent in aeolian sediment transport in beach-dune systems, conditional statements have been implemented in a selection of the figures presented below. These allow for easier recognition of potentially present coherent patterns within the data-point distributions due to the possibly modulating properties of the extra parameter, which are otherwise easily overlooked. In each concerning figure up to two extra variables (i.e., potential modulators) are included, which are discernible by difference in either shape or colour of the plotted data points.

Incident wind angle

One series of implemented conditional statements contains a distinction based on wind direction, as recorded by the ultrasonic anemometer (UA), and should provide insight into the effect of fetch on the saltation process. Recalling that the orientation of the shoreline and the shore normal are 7.2° and 277.2° from due north, respectively, three broad categories were defined as

- alongshore: $347.2^\circ \leq \theta \leq 007.2^\circ \mid 187.2^\circ \leq \theta \leq 207.2^\circ$
- oblique: $207.2^\circ < \theta < 257.2^\circ \mid 297.2^\circ < \theta < 347.2^\circ$
- cross-shore: $257.2^\circ \leq \theta \leq 297.2^\circ$

where θ is the angle of wind incidence measured in (azimuth) degrees clockwise from due north. For the purpose of ease, the alongshore and cross-shore categories also cover highly oblique and slightly oblique winds, respectively. Note that there is no category involving offshore winds, as these do not positively contribute to the sediment transport into the dunes, and no distinction is made between northerly and southerly winds.

Time-averaged water level

The second distinction is based on the time-averaged water level just off the beach (ζ_{tide}). Like with the incident wind angle, this variable is a reflection of the fetch and, to a lesser extent, also the soil moisture content of the beach surface. Note that the water levels are with respect to the Amsterdam Ordnance Datum (NAP) and that the OSSI surfaced at water levels below approximately 0 m +NAP, imposing a lower limit to ζ_{tide} at that level.

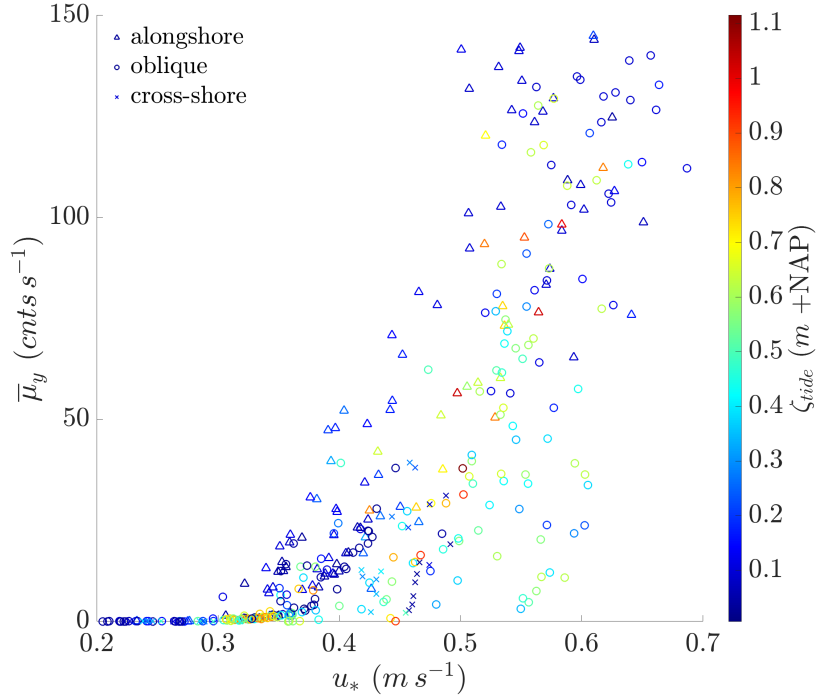


FIGURE 4.12: Scattergram of spanwise-mean saltation intensity versus shear velocity. Data markers represent 10-min temporal means from all measuring days. Symbols and colours indicate the mean wind-direction category and mean water level just off the beach, respectively.

4.3.2 Saltation and shear velocity

The wide range of wind speeds during the field campaign (see Fig. 3.4) allowed for proper assessment of how saltation intensity responds to the shear velocity (u_*). For instance, Fig. 4.12 shows that on a time-averaging scale of 10 min, the threshold of motion was exceeded one time only at $u_* = 0.30 m s^{-1}$. However, the much stronger collective response signal occurred from about $0.34 m s^{-1}$. According to Eq. 3.19, this translates to a wind speed of about $5.7 m s^{-1}$ at $0.90 m$ above the surface or $7.2 m s^{-1}$ at the conventional reference height of $10 m$. Mean saltation intensity further exhibits a steep increase with increasing shear velocity, but it goes along with considerable scatter.

More evident is the differentiation between measurements that were taken during low-water conditions (blue end of the colour spectrum) and those taken during higher-water conditions (red end of the colour spectrum), as for equal values of u_* the former were often associated with higher values of $\bar{\mu}_y$. This observation indicates a trend in which lower water levels permit an earlier onset and higher levels of saltation transport than do higher water levels. Yet, a number of measurements collected during high water of around $1 m +NAP$ plot relatively high up the scattergram, but these are generally also marked as having been collected during periods with dominant alongshore-directed winds (triangles). Thus, similar to the distinction based on ζ_{tide} , higher saltation intensities were more common during alongshore winds compared to oblique winds. The scarce moments the wind was cross-shore directed, consistently resulted in low values of $\bar{\mu}_y$, even at relatively high shear velocities in

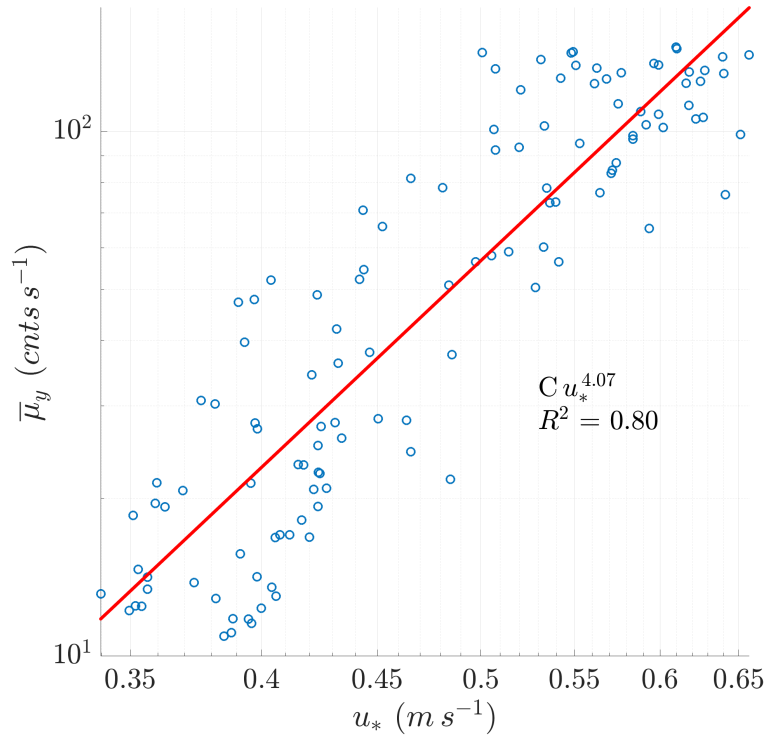


FIGURE 4.13: Log-log scattergram of spanwise-mean saltation intensity versus shear velocity. Data markers represent 10-min temporal means from all measuring days, but conform to the specified criteria. Dashed red line is a fitted model derived from a linear regression through log-transformed equivalents of the displayed data.

conjunction with low water levels. For instance, this is the case for the series of cross-shore data markers at $u_* \approx 0.45 \text{ m s}^{-1}$, which were acquired relatively high up the mid beach on a day (4 October) without rain.

Regression analysis

Figure 4.13 shows a log-log plot of $\bar{\mu}_y$ v. u_* and their linear regression (red dashed line) in an attempt to quantify their relationship. Measurements that were in some way affected by the large number of environmental factors capable of modulating this relationship are hard to recognise and subsequently isolate. Nevertheless, by going for quantity by including time averages from the complete data set, but also implementing a series of criteria to exclude outliers, it was attempted to obtain a model with reasonable accuracy for situations approximating equilibrium state. The criteria by which the data were selected were:

- $\bar{\mu}_y \geq 10 \text{ cnts s}^{-1}$;
- $\theta = \text{alongshore}$;
- $\theta = \text{oblique} \& \zeta_{\text{tide}} \leq 0.1 \text{ m +NAP}$.

The first of the criteria listed above helped suppress the inherently large dispersion near the threshold. The second and third criteria were to ensure a large enough fetch, so that any potential inhibition of transport due to excessive moisture levels could

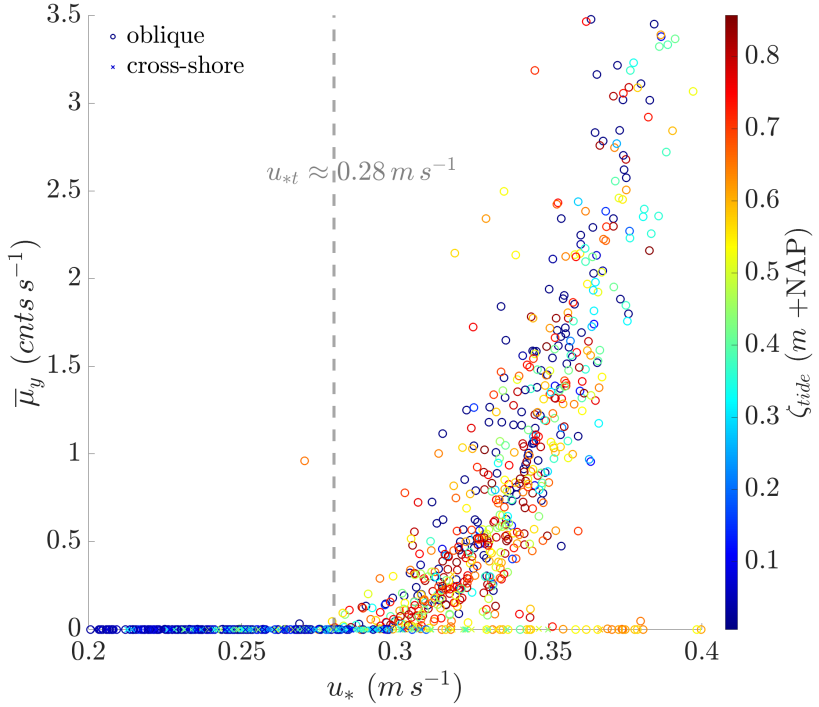


FIGURE 4.14: Scattergram of spanwise-mean saltation intensity versus shear velocity. Data markers represent 1-min temporal means of the time series collected on the 17th and 25th. Symbols and colours indicate the mean wind-direction category and mean water level just off the beach, respectively. Grey dashed vertical line marks the observed threshold shear velocity (u_{*t}).

be kept to a minimum. Note that no distinction was made based on rain activity during/before measuring.

Linear regression through the log-transformed data revealed the following relationship with *goodness of fit* (R^2) = 0.80:

$$\bar{\mu}_y = C u_*^{4.07} \quad (4.1)$$

where $\bar{\mu}_y$ has unit cnts s^{-1} , and C is some constant with (an on itself meaningless) unit cnts m^{-1} that converts the unit of shear velocity to that of saltation intensity. The obtained formula's exponent indicates a strong dependency of $\bar{\mu}_y$ upon u_* and even exceeds the classic 3rd-power-law relationship between wind forcing and sediment transport introduced by Bagnold (1941).

Threshold shear velocity

Similar to Fig. 4.12, Fig. 4.14 shows a scattergram of $\bar{\mu}_y$ against u_* , but instead uses an averaging time of 1 min and only includes data that were collected on 17 and 25 October. As mentioned in 3.3, the threshold-transport conditions on these days allowed for a more accurate approximation of the threshold shear velocity (u_{*t}) at the study site. The grey dashed vertical line in Fig. 4.14 marks the point from which the primary response in $\bar{\mu}_y$ was observed (disregarding the two outliers). On a temporal scale of 1 min, the u_{*t} was found to be approximately 0.28 m s^{-1} . The 1-s temporal scale (not displayed) revealed even lower threshold values, but the

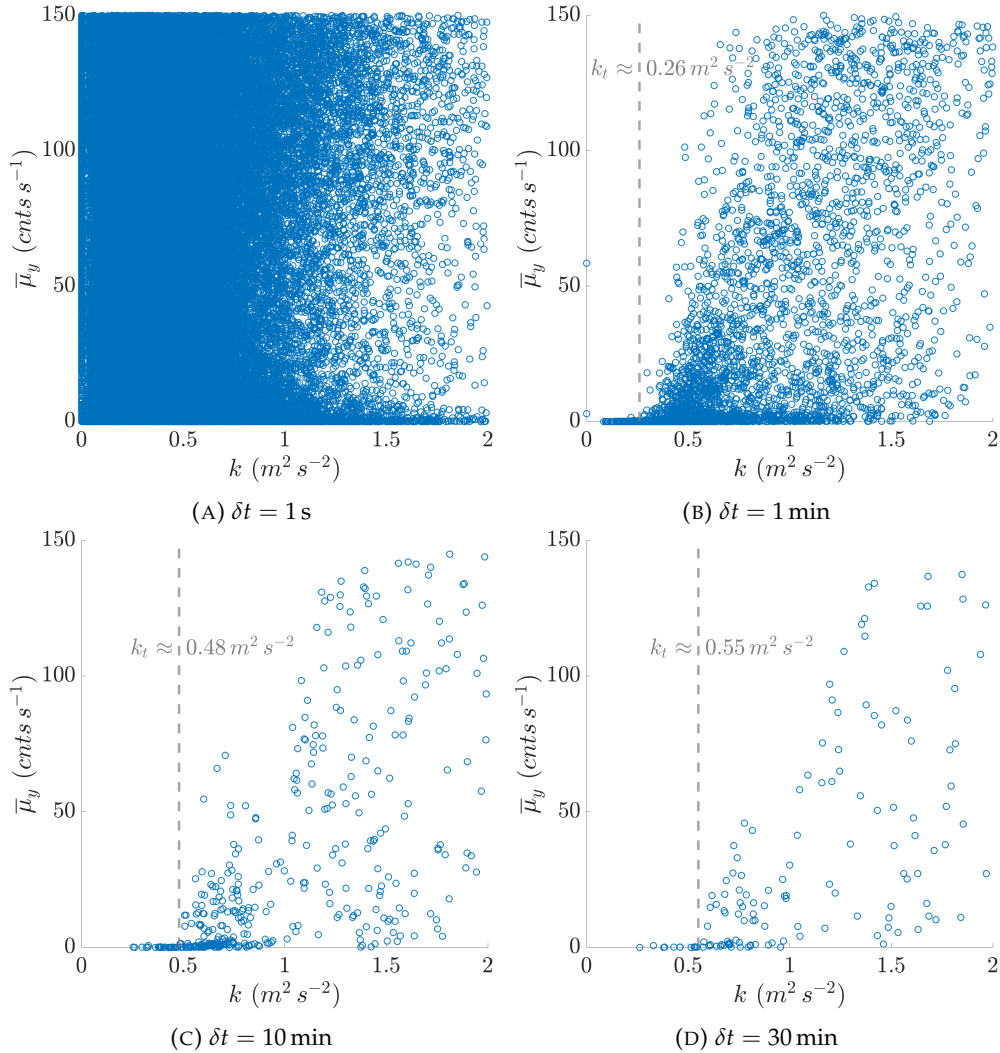


FIGURE 4.15: Scattergrams of spanwise-mean saltation intensity versus turbulence kinetic energy, where δt indicates the time interval over which the data were averaged.

probability of a deceptive representation of data due to the dissimilarity in both measuring height and location (leading to slightly out-of-sync records; e.g., see Table B.1) becomes significant on such short temporal scales. Figure 4.14 further gives the impression that higher saltation rates corresponded with larger values of ζ_{tide} , but a comparison between time series of ζ_{tide} and u revealed that on the 25th the tide was (coincidentally) falling at the same time the wind died down. During approximately two-thirds of the measuring time the wind was categorised as 'cross-shore' and none of the data collected within this time period showed signs of saltation.

4.3.3 Saltation and turbulence

In addition to the shear velocity, also the relationship between saltation intensity and turbulence kinetic energy k is investigated. Figure 4.15 shows four scattergrams of $\bar{\mu}_y$ v. k for different time-averaging scales (δt). There is a clear discrepancy between panel (A), which depicts the 1-s temporal scale, and the three other panels, which depict longer temporal scales. Multiple attempts to achieve a better correlation between the two variables at the shortest temporal scale through realignment of their

records by introducing a (anti-)lag did not result in any notable improvements. The complete loss of correlation between k and $\bar{\mu}_y$ for $\delta t = 1\text{ s}$ (Fig. 4.15a) may be in part ascribed to the fact that none of the CWT scalograms of saltation intensity (Figs. 4.9b and A.7b) reveal any respectable amounts of energy distributed over such small periods ($\lambda \leq 1\text{ s}$).

Threshold turbulence

As δt increases the kinetic-energy threshold at which saltation commenced shifts towards larger values of k , which could reflect the increase in TKE required to sustain the larger-scale fluctuations in $\bar{\mu}_y$. At the same time, the shift towards the right appears slow down and stabilise from $\delta t > 10\text{ min}$, as can be inferred from the only small difference between panels (C) and (D). Considering time-averaging scales of the order of 10 min, the amount of TKE that coincided with the initiation of saltation (k_t) is found to be about $0.5\text{ m}^2\text{ s}^{-2}$. From that point onward no evident relation could be established between $\bar{\mu}_y$ and k . Falling back on the saltation-intensity contour maps in 4.1, their corresponding values of k also do not show a consistent relation with the intensity of saltation transport. For instance, Figs. 4.3 and 4.7 have the same value for $k (= 0.38\text{ m}^2\text{ s}^{-2})$, but display considerably different levels of saltation intensity. Moreover, their k , which was averaged over 3.5 s and 5.5 s, is well below the just determined k_t for $\delta t = 10\text{ min}$, but clearly above the one for $\delta t = 1\text{ min}$.

4.3.4 Spatiotemporal variability

In order to obtain an unbiased impression of the effects of wind gustiness on the spatiotemporal variability in saltation intensity, Fig. 4.16 presents two panels that show the (A) temporal coefficient of variation of saltation intensity (CV ; see Eq. 3.3) and (B) spanwise coefficient of variation of saltation intensity (CV_y ; see Eq. 3.6) plotted against the coefficient of variation of wind speed or relative TKE (CV_k ; see Eq. 3.21). For the same reason as mentioned before in 4.2, CV represents the mean over impact sensors 5 to 7 (i.e., $CV_{p=5:7}$), as these were generally situated closest in front of the UA. Note that transport-related coefficients of variation are prone to giving excessively large values during periods of threshold transport (i.e., $I \approx 0$), which is an artefact of its computation. Furthermore, directly below panels (A) and (B) are similar panels in which relative TKE is replaced by the shear velocity, which allows for convenient comparison between their relative contributions to the spatiotemporal variability in saltation intensity.

In contrast to the two bottom panels, neither of the two upper panels in Fig. 4.16 reveals a directly evident relationship. Panel (B) displays a more or less horizontally configured distribution of the data, which indicates little to no correlation between the variables CV_y and CV_k . This implies that the gustiness of the wind had very little effect on the relative spanwise variability in saltation intensity and thus the distribution of streamers along the horizontal span of the SDS. The distribution of data in panel (A) tends more towards a positive relationship between CV and CV_k , although it also exhibits a high degree of scatter. A positive relationship between these two variables implies that an increase in wind gustiness will result in an increase in relative temporal variability in saltation intensity, or from a streamer perspective, in the temporal intermittency of passing streamers.

The effects of the shear velocity on the spatiotemporal variability in saltation intensity are much more pronounced. Even though exhibiting a fair amount of scatter, panel (C) in Fig. 4.16 reveals an evident relationship between CV and u_* , in

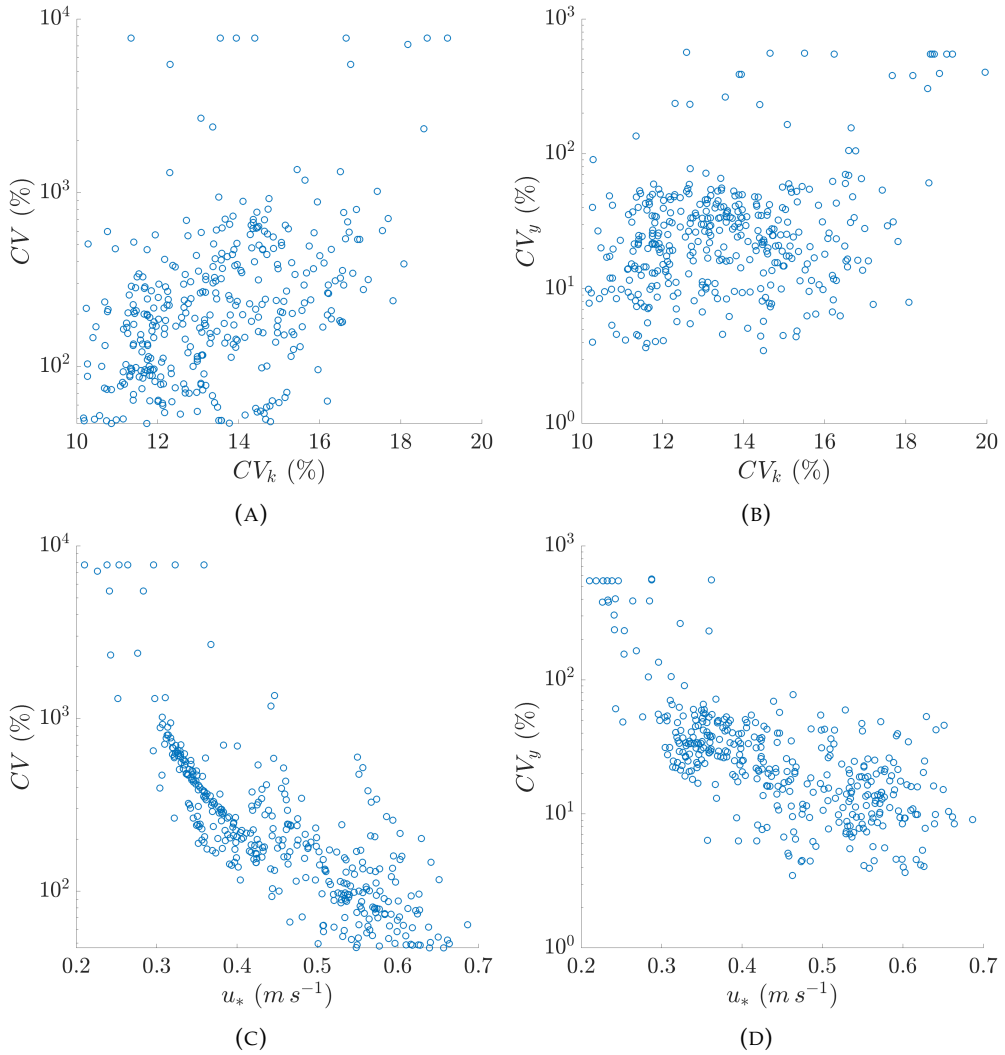


FIGURE 4.16: Scattergrams of relative temporal variability in saltation intensity versus (A) relative TKE and (C) shear velocity, and relative spanwise variability in saltation intensity versus (B) relative TKE and (D) shear velocity. Data markers represent 10-min temporal means from all measuring days. Note that the CV - and CV_y -axes are logarithmic.

which relative temporal variability in saltation intensity strongly reduces with increasing shear velocity. This relationship is perhaps best seen within the domain $0.3 \text{ m s}^{-1} < u_* < 0.4 \text{ m s}^{-1}$, which exhibits a strongly concentrated distribution of data. Values of CV reached their maximum when u_* fell below about 0.3 m s^{-1} , which corresponds well to the threshold shear velocity observed in Fig. 4.12. By contrast, CV reached its minimum of 47 % at values of u_* of about 0.6 m s^{-1} , which indicates that streamers remain temporally unsteady even for high values of u_* .

Similar, although slightly less evident, is the effect of the shear velocity on the relative spanwise variability in saltation intensity as is shown in panel (D). Even though CV_y clearly decreased with increasing u_* in the lower half of the depicted range of u_* , it appears that it stabilised for $u_* > 0.45 \text{ m s}^{-1}$ at a value of around 15 %. This observation could indicate a lower limit of CV_y on a temporal averaging scale of 10 min and a spanwise length scale of 3.1 m, which rules out the possibility of a perfectly uniform saltation sheet ($CV_y = 0$) to occur at any given value of u_* .

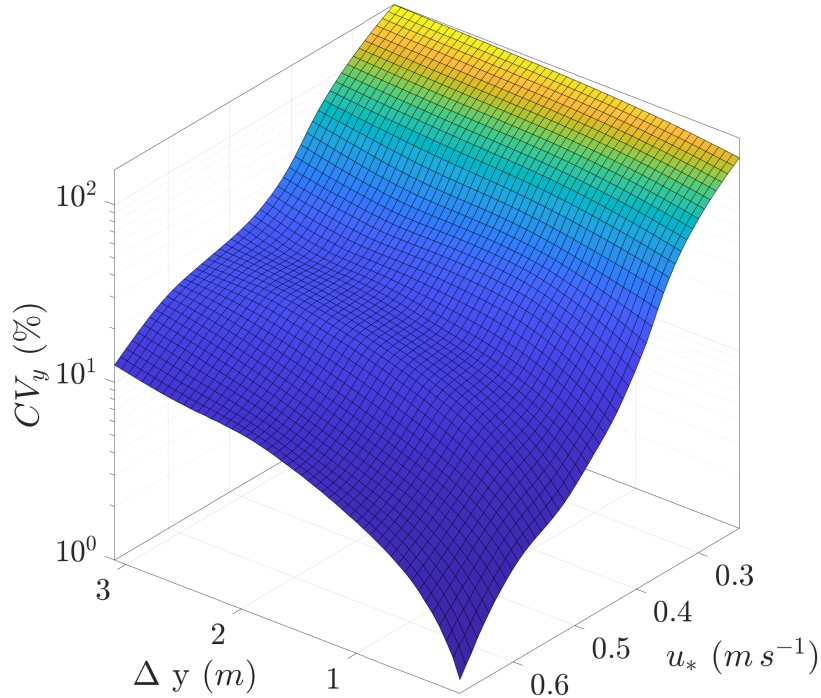


FIGURE 4.17: Locally-weighted-smoothing linear regression through 10-min temporal means of mean spanwise variability (CV_y) as a function of spanwise (i.e., transport-perpendicular) distance (Δy) and shear velocity (u_*). The plane is computed solely from data collected with SDS-UA₄. Note that the CV_y -axis is logarithmic.

Spanwise variability

So far the (relative) spanwise variability in saltation intensity has been systematically expressed in the variability over the complete horizontal (3.1-m) span of the SDS. However, the effect of streamer transport on this variability on smaller scales and its corresponding dependency on the shear velocity has as of yet remained unresolved. Following the computation procedure described in 3.6.3, the plane in Fig. 4.17 depicts a multivariate regression in 3-D space through (the mean of all permutations of) relative spanwise variability (CV_y) as a function of spanwise distance (Δy) and shear velocity (u_*). Only data collected with SDS-UA₄ were included in the computation, as its impact sensors suffered the least malfunctioning symptoms of all three SDSs.

The regression in Fig. 4.17 shows there was a logarithmic increase in CV_y with increasing Δy , which likely reached its optimum somewhere just beyond the lateral scope of measurement (i.e., $\Delta y > 3.1$ m). This observation implies that the degree of spanwise intermittency in saltation transport induced by streamers increased with the number of contiguous impact sensors included in the calculation (i.e., the farther away from approximating a uniform saltation sheet). One of the contour maps, e.g., Fig. 4.5, could help to illustrate this, as it barely contains any timestep for which more than a couple of impact sensors along the horizontal span received an equal number of grain impacts. However, the logarithmic function also implies that saltation transport in the shape and behaviour of streamers can only cause up to a certain degree of spanwise intermittency, as their relative contributions to this spanwise

variability reduces when considering larger spanwise scales (i.e., it approaches a statistical optimum). For instance, when considering two contiguous impact sensors (i.e., $\Delta y = 0.1$ m) the chance of a streamer being detected by only one of the two impact sensors is relatively small due to the width and possibly sideways-undulating movement of the streamer. Now, when considering a few more impact sensors the chance of some impact sensors detecting no streamers, whereas others do increases, which will eventually result in an increase in CV_y . However, the more impact sensors are included (i.e., the larger the spanwise scale considered), statistically also the chance of streamers passing through the horizontal span increases, which in turn negatively contributes to the increase in CV_y .

By contrast, increasing values of u_* accompanied progressively reduced values of CV_y , which complies with the trend seen previously in Fig. 4.16d. This reduction in CV_y is seen for all values of Δy , but is most pronounced for the smallest values of Δy . Following on what is said above, the lower the shear velocity, the more sporadically streamers are being formed, which is also reflected in the temporal variability (see Fig. 4.16c). This effectively reduces the chance of streamers passing through the considered horizontal span at the same time, hence positively contributes to CV_y . Again, the contour maps in 4.1 could help to illustrate this, as intensified transport conditions following an increase in u_* clearly result in more sheet-flow-like patterns (e.g., Fig. 4.6) in which at any given timestep there is a large group of impact sensors detecting similar saltation rates, whereas that is not the case for a low u_* (e.g., Fig. 4.3).

Maximum values of CV_y amounted up to about 16 % of the magnitude of \bar{u}_y for the largest spanwise distance (i.e., $\Delta y = 3.1$ m) during periods of highest measured u_* , whereas this amount increased up to about 155 % when u_* was lowest. For the smallest spanwise distance (i.e., $\Delta y = 0.1$ m) these two values reduced to approximately 2 % and 123 %, respectively. These percentages are an indication of the streamer-induced error margins that may have to be incorporated in traditional saltation transport models that rely on spanwise extrapolation on temporal scales of 10 min.

4.3.5 Fetch and surface moisture

The following figures present data acquired on two measuring days on which the three SDSs were aligned in a streamwise fashion (i.e., in the direction of transport). Deployment details and weather conditions are described in 3.3.2 and visualised in Fig. 3.6. The main purpose of these figures is to illustrate the importance of relative location on the beach within the saltation system and, specifically, the result of fetch and surface moisture content on streamers, hence the saltation intensity.

Fetch

Both panels in Fig. 4.18 demonstrate a clear dissimilarity in saltation response to u_* as a function of relative location, which is especially evident from the fitted power functions in panel (B). Although on both days the total range of detected \bar{u}_y was not that different amongst the contemporary deployments, disregarding the few outliers measured by SDS-UA₂ in panel (B), the range of measured u_* differed substantially. Figure 4.18a shows that within the same time span u_* varied between 0.43 m s^{-1} and 0.64 m s^{-1} near the dune foot (SDS-UA₂), whereas between 0.51 m s^{-1} and 0.69 m s^{-1} on the mid beach (SDS-UA₄). The fact that the data from SDS-UA₃, which occupied the middle position, plots well in between, indicates there was a consistent reduction

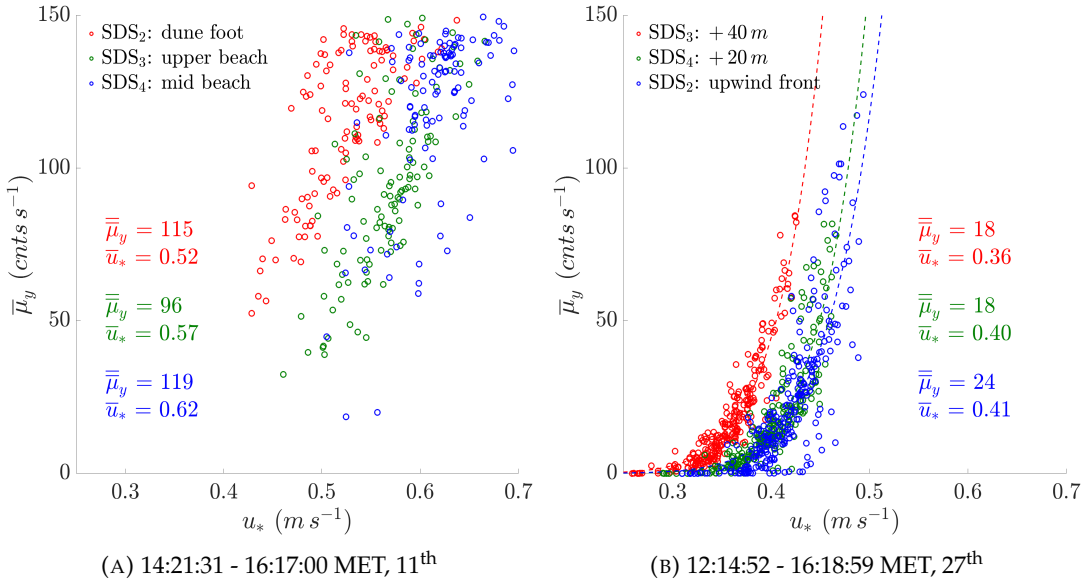


FIGURE 4.18: Scattergrams of saltation intensity versus shear velocity on (A) 11 October and (B) 27 October. Data markers represent 1-min temporal means. Only data are displayed from the time periods when all SDSs, positioned in a streamwise fashion behind one another, were actively measuring. Colours indicate relative positions. Mean values are given in corresponding colour. Dashed lines in panel (B) are fitted power functions. Note that for the legend in (B) the '+ length scale' is positive in downwind direction.

in u_* with downwind distance. Such a trend, which is also recognised in panel (B), is indicative of the airflow slowing down due to blockage by the tall foredune and, probably to a lesser extent, a developing internal boundary layer (IBL). Recalling that $\bar{\mu}_y$ is strongly controlled by u_* (see Fig. 4.13 and Eq. 4.1), it may be expected that this reduction in u_* will also be strongly reflected in the value of $\bar{\mu}_y$. However, as is indicated by the mean values included inside each panel, this effect is not directly evident. Panel (A) even shows that the mean saltation rate measured by SDS-UA₂ near the dune foot ($\bar{\mu}_y = 115 \text{ cnts s}^{-1}$) was practically equal to the one measured by SDS-UA₄ on the mid beach ($\bar{\mu}_y = 119 \text{ cnts s}^{-1}$), even though the measured mean shear velocity was a significant 0.10 m s^{-1} lower. The fact that SDS-UA₄, on the other hand, did meet the above expectations by actually detecting less saltation ($\bar{\mu}_y = 96 \text{ cnts s}^{-1}$) with a lower u_* might be suggestive of a point somewhere between the locations of SDS-UA₃ and SDS-UA₂ from where the fetch effect started to overcome the effect of a lower u_* .

Furthermore, the separation of the data distributions appears slightly more pronounced within the lower range of $\bar{\mu}_y$, while they become more intermixed as the energy in the system increases. For instance, panel (A) shows that for $u_* \approx 0.52 \text{ m s}^{-1}$, there were cases when SDS-UA₂ (dune foot) detected nearly twice as many counts (112 v. 62 cnts s^{-1}) as SDS-UA₃ (upper beach) and about three times as many (62 v. 19 cnts s^{-1}) as SDS-UA₄ (mid beach). By contrast, focusing on where the data are most concentrated, for $u_* > 0.61 \text{ m s}^{-1}$ all three deployments consistently yielded more or less similar count rates. Something similar can be said for the front two deployments (SDS-UA₂ and SDS-UA₄) in panel (B). These observations suggest that the higher the wind speed (i.e., the more energy contained in the system), the smaller

the differentiation across the beach in terms of saltation intensity, hence the more accurate traditional saltation transport models are likely to be. This could be ascribed to the faster airflow effectively reducing the time for the saltation system to adapt towards a newly set equilibrium between two streamwise-distanced locations.

Surface moisture

Figure 4.19 displays gravimetric soil moisture profiles generated from soil moisture measurements taken along transects upwind of SDS-UA₄ (mid beach; left panel) and SDS-UA₃ (upper beach; right panel) during the time both were measuring (more specifics on the exact procedure are given in 3.3.2). The profile sequence in the left panel reveals a steady increase in soil moisture content when moving along the transect away from SDS-UA₄ (right end). This gradient remained practically unchanged as the profiles commenced a mainly downward trend through time. On the seaward end of the profiles soil moisture levels started well above the threshold moisture content ($\theta_{g,t}$) of 10 % (grey dashed line) as proposed by, amongst others, Davidson-Arnott et al. (2005), but by approximately 16:06 MET soil moisture levels dropped (just) below it along the whole transect. Surface moisture probably played only a minor role during the time interval depicted in Fig. 4.18a (14:21:31 - 16:17:00 MET), as for a considerable length of beach upwind of SDS-UA₄ soil moisture levels were already below threshold for most of the time (see left panel in Fig. 4.19). This demonstrates that the wind and fetch were the most important factors controlling $\bar{\mu}_y$ at that particular time interval. In contrast to the situation on the mid beach, the profiles in the right panel reveal that no significant changes occurred in soil moisture levels on the upper beach (SDS-UA₃) as they remained at a constant level well below the threshold, not exceeding 4 %, which indicates that the monitored stretch of beach directly in front of SDS-UA₃ was 'dry' for the entire measurement run. The discrepancy between the two panels can be explained by the kink in the profiles at $d_x = 101.5$ m, which indicates the position of the high-water line, hence puts SDS-UA₃ outside the zone influenced by the tide, as opposed to SDS-UA₄.

Figure 4.20 shows the time series of $\bar{\mu}_y$ (solid lines) and u_* (dashed lines) corresponding to the deployments in Fig. 4.19 and, in addition, provides the time series of ζ_{tide} . All time series have been smoothed through robust local regression using weighted linear least squares and a 2nd degree polynomial model (*rloess*) with a span of 20 % in order to expose the larger-scale evolution of the variables through time. The lower panel directly provides a logical explanation for the observed drying at the mid beach (Fig. 4.19: left panel), as it coincided with a drop in ζ_{tide} , which reflects a falling tide. Before the effects of the receding tide became apparent, saltation rates were substantially lower on the mid beach (SDS-UA₄) compared to the upper beach (SDS-UA₃), even though u_* was consistently higher throughout the measurement run. Environmental factors responsible for this discrepancy were likely a combination of above-threshold surface moisture levels upwind of SDS-UA₄, a smaller fetch and the fact that the difference in u_* was generally only less than 0.5 m s⁻¹. However, from about 14:00 MET (i.e., ~1.5 h after the tide started receding) SDS-UA₄ experienced a rapid increase in saltation rate, which coincided with strong surface drying and about half of the transect below threshold (Fig. 4.19: purple profile in left panel) following the falling tide (lower panel in Fig. 4.20). This rapid increase in $\bar{\mu}_y$ reflects the sudden formation of streamers upwind of SDS-UA₄. Since at 14:07 MET (purple profile) θ_g was below threshold until the sixth moisture marker, and knowing that these markers were spaced by approximately 2-m intervals with the first marker in

line with the SDS's horizontal span, it follows that the majority of these streamers were formed within $(6 - 1) \times 2 = 10$ m of beach length from SDS-UA₄.

Furthermore, in about half an hour after the onset of the increased streamer formation on the mid beach ($\sim 14:30$ MET) saltation rates even surpassed those on the upper beach by substantial amounts (>30 cnts s⁻¹), which indicates that after the drying phase of the beach the slightly higher u_* on the mid beach was sufficient to make up for the smaller fetch. The fact that these observations stand in stark contrast to those back in Fig. 4.18a when comparing SDS-UA₄ (mid beach) with SDS-UA₂ (dune foot) supports the idea of an imaginary downwind threshold point beyond which fetch overcomes the slowing of the wind speed (or shear velocity) and vice versa. These results show that across the beach there is a complex interplay between fetch, surface moisture and shear velocity that ultimately determines the local formation of streamers, and accounts for their variability on spatial scales of metres to tens of metres and timescales of minutes to hours.

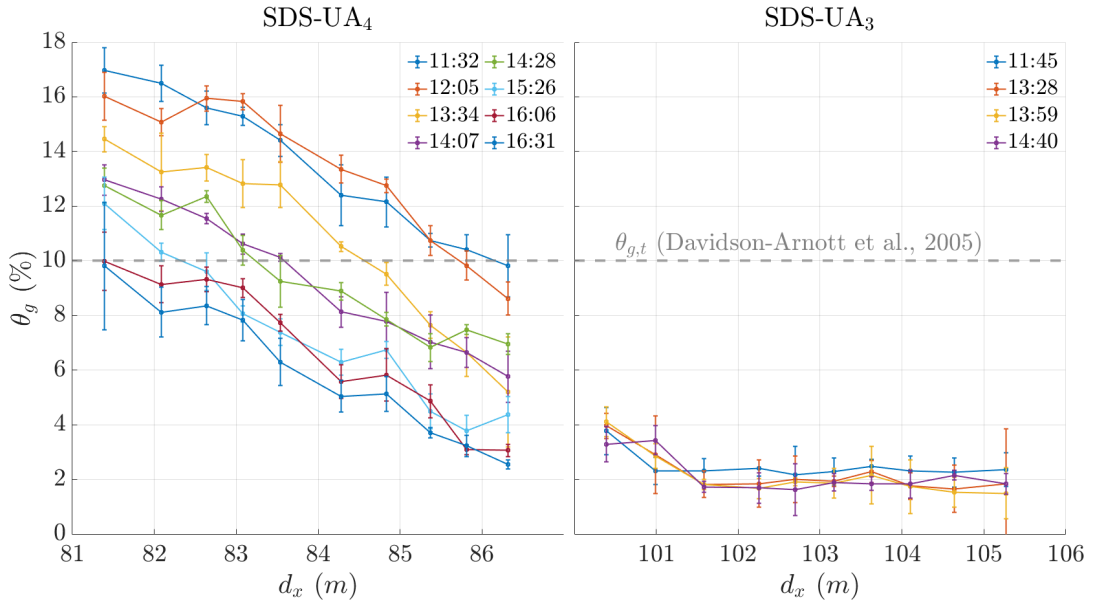


FIGURE 4.19: Soil moisture profiles (including standard deviations) along the saltation field (in wind-normal direction) in front of SDS-UA₃ and SDS-UA₄ on 11 October. Horizontal grey dashed line denotes the threshold moisture content ($\theta_{g,t}$) proposed in literature. Cross-shore distance d_x is the horizontal distance to the OSSI (\approx low-water line), i.e., left is seawards. The right limit of the profiles roughly corresponds to the location of one end of the SDS's horizontal span.

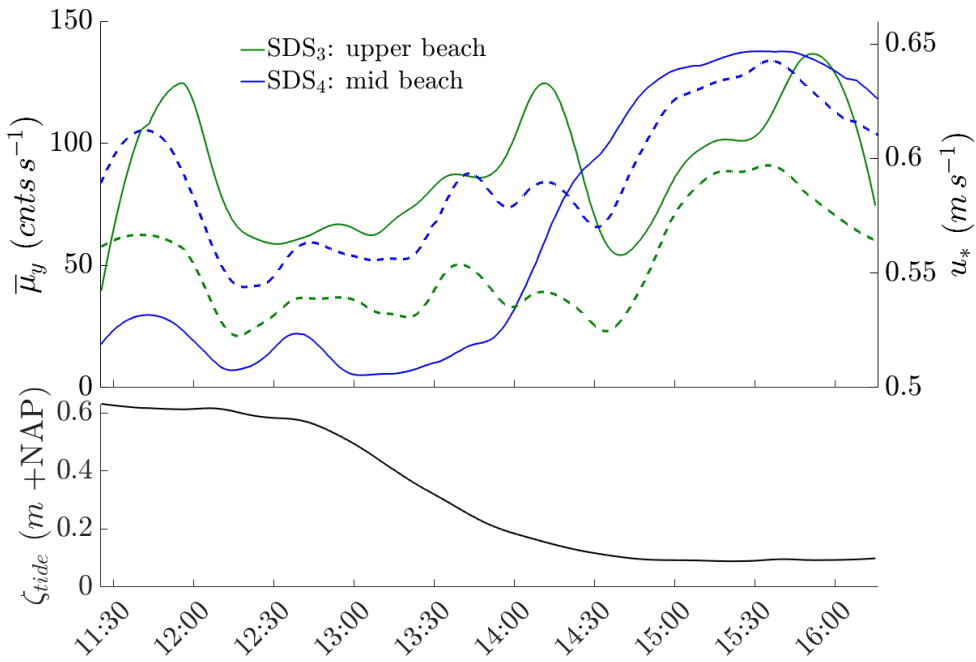


FIGURE 4.20: Time series of (upper panel) spanwise-mean saltation intensity (solid lines) and shear velocity (dashed lines) from SDS-UA₄ (green) and SDS-UA₃ (blue), and (lower panel) time-averaged water level just off the beach. Data are smoothed (*rloess*, span = 0.2) 1-min temporal means collected on 11 October.

5 Discussion

5.1 Mapped streamers

The series of spatiotemporal maps of saltation intensity in 4.1 have provided a number of insights into the typical patterns adopted by streamers for a range of transport conditions. From the observation height of 0.1 m and starting from threshold, the first perceived signs of streamers are that of a scattered pattern consisting of very low-intensity patches of saltation (Fig. 4.3). As transport conditions are incrementally increased, the first pattern that follows is that of more elongated clusters of more pronounced saltation that are also locally interlinked (Fig. 4.4). Further intensification of transport is seen to result in multiple elongated clusters of high saltation intensity, which are all largely connected through an underlying sheet of much lower saltation intensity (Fig. 4.5). Moving on to heavy transport conditions, the underlying saltation sheet has fully developed and now covers the full map. Embedded in the saltation sheet are many individual elongated clusters of pronounced saltation of which many are also partly interconnected on a higher intensity level (Fig. 4.6). Important here is that, the streamer pattern is systematically taken as a function of the transport conditions, the latter are defined mainly by the wind speed and not necessarily the overall mean saltation intensity as became evident after comparing Figs. 4.6 with A.5. Nonetheless, these maps reveal the possible evolution of the streamer pattern under intensifying transport conditions and are broadly comparable to the patterns recognised by Baas and Sherman (2005) (Fig. 2.5). For instance, the streamer patterns displayed in the upper panels of Figs. 4.3 and 4.4 would possibly fit into the category of 'streamer families', those in Fig. 4.5 into the category of 'nested streamers', while those in Fig. 4.6 best fit the description for 'clouds with embedded streamers'. Their resemblance to each other is also supporting evidence for the ubiquity of streamers and the way they migrate under various transport conditions, regardless of, e.g., morphology and grain size. Moreover, the perceived evolution of the streamer pattern towards more dominantly sheet-flow-like (i.e., $\sigma = \sigma_y = 0$) is also reflected by the consistent drop in variability relative to the mean (captions Figs. 4.3—4.6). Thus, for traditional saltation transport models dealing with more intense transport conditions would logically result more accurate predictions, as it more closely resembles their often (over)simplified approach to the sediment transport system.

Important to realise here is that the above statements are based on horizontal cross sections taken in this study at a height of 0.1 m from the bed, whereas at 0.04 m in the study by Baas (2003). The vertical profile in the lower panel of Fig. 4.3 clearly shows that what is observed as small saltation patches in the upper panel may actually be only the very tip (or head) of each streamer passing through. Since with intensifying transport conditions also the height of the saltation layer increases (Figs. 4.3–4.6), it might be said that the only real difference between certain streamer patterns observed at different heights is the intensity of transport conditions under which they occur. For instance, for equal transport conditions one may observe

'clouds with embedded streamers' very close to surface, whereas another only observes 'streamer families' but farther from the bed (Fig. 2.4). However, the earlier mentioned flattening of the saltation-layer height under intense transport conditions indicates the existence of a height limit for which this is true.

Further focusing on the vertical saltation profiles in Figs. 4.3 and 4.2, streamers are seen to exhibit another typical behaviour: they tend to arrive head first after which they diffusively collapse. The head part is recognised by a short but steep positive gradient in the saltation-layer height, and is followed by a much shallower negative gradient, the tail, until completely solved. Since this behaviour is observed for both the smallest (Fig. 4.3) and largest (Fig. 4.2) of streamers, it would be expected to return under all sorts of transport conditions. However, in the vertical profiles in Figs. 4.4, 4.5 and 4.6 this behaviour is seldom recognised, with a possible explanation that the individual streamers succeeded each other at such a fast pace that the gradients had effectively become flattened out.

It has proven difficult to isolate individual from the generated contour maps, which would be required to quantify their typical length scales. However, following the example of Baas and Sherman (2005) by applying a filter to obtain spatiotemporal maps in which only the relative intense clusters are outlined, has provided an opportunity to gain a better insight into their typical length scales. The observed range of widths of 0.1 to 0.3 m and centre-to-centre spacings of 0 to 0.5 m of the outlined (embedded) streamers in Fig. 4.7 are comparable in order of magnitude to those reported by Baas and Sherman (2005) and Sherman et al. (2013). The probably most common width in Fig. 4.7 was substantially greater than the one found by Baas and Sherman (2005) (0.2 m v. 0.12 m). At most, 0.39 embedded streamers were detected every spanwise metre, which is considerably more than the 1.11 streamers per spanwise metre reported in Baas (2003). However, there are many factors such as the intensity of the saltation transport, sediment composition and, not the least, the applied filter that may have contributed to any discrepancies between the various studies. In addition, in theory, the spatial resolution of the horizontal sensor array in this study limited the minimum width of a streamer that could be discerned with absolute certainty to slightly less than 0.2 m, viz., when a single streamer is picked up by one impact sensor but just not quite yet by the two neighbouring ones. For the same reason, it cannot be said for certain whether it might also be common for two neighbouring (embedded) streamers to travel at less than 0.2 m apart from each other. One would need a more closely spaced array of impact sensors to gain insight into that particular matter.

Furthermore, the streamer lengths of up to 0.5 m found at 0.1 m from the bed (Fig. 4.7) are similar to the ones found by Baas and Sherman (2005), but an order of magnitude smaller than those reported by Sherman et al. (2013). The migration speed of 2.73 m s^{-1} , derived from footage of a passing streamer (Fig. 4.1) and used to convert the streamer durations into lengths scales, is also similar to the 3.6 m s^{-1} proposed by Baas and Sherman (2005), which is comforting. However, taking into account the typical shape factor of streamers (Fig. 4.2), it is very likely that the actual streamer lengths were much greater at lower heights, and may in the end more closely resemble the numbers given by Sherman et al. (2013).

5.2 Streamers and wind

In the last remaining set of spatiotemporal maps of saltation intensity (Fig. 4.8) it was clearly shown that a sudden momentary drop in horizontal wind speed, albeit by a small change in wind direction, can easily mean the difference between an intense continuous saltation cloud (with embedded streamers) and no transport at all. On the other hand, a quick recovery of the wind speed appeared to be able to completely resume saltation transport to levels prior to the break just as fast. Such transitory events within the saltation system may not be that surprising considering the generally strong dependence of the saltation intensity on the wind speed (Fig. 4.13), for which a relationship (Eq. 4.1) was established that even exceeds the classic Bagnold-type 3rd-power-law relationship (Bagnold, 1936) in terms of its exponent. However, it must be noted here that the relationship in Eq. 4.1 was determined from saltation data collected during (close to) equilibrium conditions. During times of dominant cross-shore winds, the dependency might as well be reduced to a more linear relationship due to the possibly resulting supply-limited conditions (De Vries et al., 2014). However, during the ‘events’ depicted in Fig. 4.8 the wind was highly oblique ($\theta = 343^\circ$) making such situation highly unlikely, despite the beach at the study site being relatively narrow.

The rapid resumption of large-scale saltation following the transport break in Fig. 4.8 coincided with a u_* of 0.45 m s^{-1} , which is considerably higher than the threshold shear velocity found in Fig. 4.14 ($u_{*t} \approx 0.28 \text{ m s}^{-1}$). It must, however, be noted that this threshold is biased to some degree, as it is derived from 1-min temporal means, which means that any instantaneous spikes in u_* were suppressed. Theoretically, the total number of grain impacts corresponding to the lowest found value of u_* might have entirely resulted from the passage of a single transient gust within the 1-min time interval. This effect is illustrated by comparing the observed thresholds in Figs. 4.12 and 4.14. Moreover, another factor compromising any direct comparisons between potential values of u_{*t} is the dynamic nature of the roughness length (z_0) under transport conditions (Hsu, 1971; Sherman, 1992). Yet, the correctness of the established u_{*t} is also substantiated by its close resemblance to the theoretical fluid threshold shear velocity (Bagnold, 1941) (e.g., 0.29 m s^{-1} for $D_{50} = 400 \mu\text{m}$ (Baas and Sherman, 2006)). In the case of Fig. 4.8, it seems likely that surface moisture effectively raised u_{*t} (Davidson-Arnott et al., 2005), of which the effects are well illustrated by the series of cross-shore data markers (unrelated to the current case study) in Fig. 4.12 at $u_* \approx 0.45 \text{ m s}^{-1}$. In addition, by showing a relatively steep gradient, these same markers also reveal that once the raised u_{*t} is exceeded, the increase in saltation rate with increasing u_* beyond that point is not necessarily inhibited and may even be encouraged, which is in line with the observations in Fig. 4.8.

Interestingly, given that the values of u_* marking the start and end of the transport break depicted in Fig. 4.8 were practically the same ($\sim 0.45 \text{ m s}^{-1}$), there is no sign of any hysteresis, which is generally considered inherent in the saltation response (Spies, McEwan, and Butterfield, 2000; Mayaud et al., 2017). Nonetheless, some delay is visible when closely eyeballing the height of the saltation layer (middle panel) as it follows the small-scale changes in wind speed (red solid line). For the purpose of providing insight into the phase relationships, hence time delays, between I and u at different temporal scales, the WTC scalograms (Figs. 4.10 and 4.11), be it from different measuring days, have proven particularly suitable. They reveal common (time-varying) oscillations (i.e., strong coherence + phase-locked behaviour) for a range of temporal scales, which is in line with the expectations (e.g.,

Ellis et al., 2012; Spies, McEwan, and Butterfield, 2000). The (mean) time lags of ~ 0.5 s for $\lambda \leq 10$ s (Figs. 4.10b and 4.10c) fall well within the commonly proposed range of response lags of < 2 s (e.g., Butterfield, 1993), and are likely attributed to saltation inertia (Mayaud et al., 2017). However, it is noteworthy here that the WTC scalograms' phase arrows and CPDs are biased to some degree, as a result of the distance between the sensitive parts of the SDS and UA in both the horizontal and vertical. By way of illustration, the vertical wind profile (Figs. 2.3 or A.4) demonstrates how different velocities are reached at different heights from the bed, thereby effectively compromising the accuracy of the phase-related results, even though the slightly faster moving air at the measuring height of the UA with respect to that of the impact sensors might partially make up for the extra downwind distance. Moreover, since there were no statistical procedures undertaken –the official MATLAB package offered none– such as contours that may help indicating statistical significance, the presented results must be interpreted with caution.

All the same, the strong coherence found between the signals of I and u for $\lambda \geq 10$ s (Fig. 4.10) corresponds well to the 'integral timescale' (Fig. 2.11b: $T \leq 10$ s) recognised by Baas (2006). His associated description of 'distinct episodes' of saltation also fits the two individual 'saltation waves' observed in Fig. 4.8. In addition, the far more persistent range of temporal scales ($\lambda \geq 300$ s) revealing strong coherence (Fig. 4.10) in turn corresponds well to the 'external range' (Fig. 2.11b: $T \geq 60$ s), which relates the time-averaged u_* to the long-term transport conditions (Baas, 2006). The lengths of these dominant periods are also a direct reflection of the sizes of the most important turbulent eddies (Hunt and Morrison, 2000) in the saltation system. Thus, it follows that it are predominantly the large-scale eddies with periods of the order of tens of seconds to minutes that are responsible for the streamer formation (Fig. 2.10) in this study. From Fig. 4.15 it may, perhaps, also be concluded that the minimum amount of TKE (k_t) associated with these eddies is of the order of $0.5 \text{ m}^2 \text{ s}^{-2}$.

5.3 Streamers and variability

Aeolian streamers are probably most renowned for their impact on the spatiotemporal variability of sand transport (Baas, 2008). The evolution of the streamer pattern with intensifying transport conditions as demonstrated by the sequence of contour maps in Figs. 4.3–4.6 was accompanied by a consistent relative decrease in the mean of both temporal and spanwise variability in saltation intensity. Increasing transport conditions implies moving away from the threshold of motion, which inherently reflects in a decrease in variability over time (Ellis et al., 2012). As streamers are being formed more quickly and massively, they will automatically have more neighbours and follow each other up more quickly. The decrease in relative temporal variability is also evident from Fig. 4.16c, as CV shows to strongly decrease with increasing u . In addition, consistent with findings by Davidson-Arnott and Bauer (2009), CV also tends to reduce with decreasing gustiness (Fig. 4.16a), as was also the case for the sequence of spatiotemporal maps (see corresponding k relative to \bar{U}).

Gustiness, however, barely contributes to the relative spanwise variability (Fig. 4.16b), whereas the shear velocity clearly does (Fig. 4.16d). As for the spanwise variability on different spanwise scales, the trends seen in Fig. 4.17 show strong resemblance to those presented in Baas and Sherman (2005) and Baas and Sherman (2006) (Fig. 2.7), which is indicative of the consistency of streamer behaviour, be it (1) on a narrow sandy beach, (2) on top of a coastal sand dune or (3) on an arid sand

mound. The generally smaller values found for CV_y compared with those reported in Baas and Sherman (2005) can be attributed to the larger time-averaging scale used in this study, enabling the lateral migration of streamers to smooth the variability through time (Ellis et al., 2012).

Furthermore, besides wind gustiness and shear velocity, there are other factors that may further contribute to the spatiotemporal variability in saltation transport by controlling streamer formation. For instance, local variability in drying rates of the beach surface (Bauer et al., 2009) may also create preferential flow paths for streamers (Gares et al., 1996), which might have played a role in the events depicted in Figs. 4.4 and 4.5.

5.4 Streamers across the beach

Moisture and fetch are widely recognised as important parameters controlling sediment transport (Davidson-Arnott et al., 2005; Bauer et al., 2009; Delgado-Fernandez, 2010; Ellis and Sherman, 2013). If searched for, their effects are often easily recognised in diagrams such as Fig. 4.12. General trends visible in this figure are a less pronounced saltation response for (1) oblique and in particular cross-shore directed winds, and (2) higher time-averaged water levels (ζ_{tide}). The first trend highlights the importance of fetch, as it determines whether the saltation cascade (Chepil, 1957; Baas, 2003) and Owen effect (Gillette, Hardebeck, and Parker, 1997) are able to sufficiently develop. The second trend underlines the importance of fetch in combination with surface moisture, in this case reflected by tide level. As the tide rises it effectively immobilises the top layer (Chepil, 1958) of an increasingly large stretch of beach by locally increasing the threshold shear velocity (Bauer et al., 2009). The latter is well illustrated in Fig. 4.8, which shows u_{*t} to be raised by a factor 1.6 (with respect to 0.28 m s^{-1}). Parts of the beach where moisture levels exceed the threshold moisture content (e.g., near the water line), transport shuts down completely (Davidson-Arnott et al., 2005) and the beach is effectively narrowed down, hence the maximum fetch (Fig. 2.2) is shortened for all but alongshore winds. Deviations from these general trends in Figs. 4.12 and 4.14 often have easily identifiable origins, for example, the saltation field upwind of an SDS located at the dune foot would not so quickly be compromised by the upcoming tide.

Bauer et al. (2009) usually measured the highest saltation rates on the mid beach rather than the upper beach (i.e., farther downwind) and ascribed it to the downwind reduction in shear velocity as a function of IBL depth (Fig. 2.3), which in turn reduces the transport competency of the near-surface wind. In this study a similar trend across the beach was found in shear velocity (Fig. 4.18), but not entirely in saltation rate (Fig. 4.18a). Although from mid towards upper beach the reduction in shear velocity, which may be attributed to a combination of deepening of the IBL and airflow blockage by the foredune, was indeed accompanied by a reduction in saltation rate, an almost complete recovery in saltation rate was observed at the dune foot (Fig. 4.18a). The discrepancy between the observations on the upper beach and at the dune foot is not easily explained. First of all, the critical fetch was probably not yet reached, given the relatively high shear velocities (e.g., Fig. 4.13) and the fact that the much lower shear velocity at the dune foot was able to entrain nearly as much grains as on the mid beach and even more than on the upper beach. The fact that during the time interval depicted in Fig. 4.18a the upper beach was practically dry (Fig. 4.19: right panel) rules out that surface moisture was likely (completely) responsible

for the discrepancy, unless the very low surface moisture levels ($\theta_g < 4\%$) were indeed capable of raising the threshold shear velocity sufficiently (Delgado-Fernandez and Davidson-Arnott, 2011). Naturally, the location at the dune foot benefited from a greater fetch, which was probably also lengthened due to the alongshore deflection of the wind by the foredune (i.e., topographic steering) (Donker, Maarseveen, and Ruessink, 2018). Thus, given that the moisture effect was indeed negligible (except for the mid beach), it is most likely that from a certain fetch between the upper beach and the dune foot the fetch effect is able to make up for the reduction in shear velocity. However, caution is needed, as there are many other factors with potential mediating qualities. The steep foredune may have promoted increased sand fluxes by accumulating the streamers as they arrive at its foot, which would in turn result in an increase in roughness length (Gillette et al., 1996). In addition, there are factors such as the turbulence intensity and the proximity of small-scale topography (e.g., embryo dunes), of which the effects have not been thoroughly examined in this case study.

The complexity of the study site (i.e., narrow beach-dune system) is once again highlighted by the fact that immediately prior to the events discussed above away from the foredune (i.e., lower down the beach) a fundamentally different 'competition' took place, which mainly involved surface moisture due to tidal inundation (Fig. 4.20). At first (11:30 MET), streamer formation on the mid beach was severely constrained by the largely above-threshold moisture levels (Fig. 4.19: left panel), but following the onset of the receding tide (12:30 MET), saltation rates were able to fully recover over the course of just 2 h (14:30 MET). Given that the value of $\theta_{g,t}$ was indeed approximately 10% (Davidson-Arnott et al., 2005), highly productive streamer formation appears to be achieved over a relatively short effective fetch of no more than 10 m, regardless of still reasonable levels of surface moisture ($\theta_g \sim 7\%$). Possibly did eddy-induced flow accelerations (Hunt and Carlotti, 2001) superimposed on the already high mean shear velocity ($\sim 0.6 \text{ m s}^{-1}$) still frequently exceed the threshold shear velocity, despite its moisture-induced raise (Arens, 1996; Bauer et al., 2009). Besides, Delgado-Fernandez (2010) recognised the increasing importance of the fetch effect during strong wind events, which would at the same time account for the observed discrepancy between the mid and upper beach by increasing the relative value of the (shorter) fetch on the mid beach due to the locally higher shear velocities.

5.5 Saltation detection systems

For quality assessment, the spatiotemporal maps of saltation intensity generated in this study were compared to Fig. 2.5 (Baas and Sherman, 2005), which had served as a source of inspiration. Visual examination confirmed the various maps to be qualitatively comparable, despite some fundamental differences in measuring set-up and instrumentation: as opposed to the impact sensors of the SDS, the Safire impact sensors

- were much less sensitive (minimum grain size detectable = 0.4 mm);
- had smaller frontal areas (4 cm^2);
- were spaced twice as finely (0.05 m);
- recorded at twice the frequency (20 Hz) and
- were positioned at only 0.04 m above the bed.

Disregarding some of the inherent flaws of the Safires, the spacing and sampling frequency enabled a higher spatiotemporal resolution of the maps and would result in higher-resolution representations of distinct streamer patterns. Baas and Sherman (2005) argued that a 0.1-m spacing of impact sensors does not provide sufficient resolution to be able to properly capture streamer patterns in transport maps, as they found streamers to have typical widths on the order of 0.1 m to 0.2 m (at 0.04 m above the bed). On the other hand, a sensor spacing closer than 0.1 m could lead to serious modification of the airflow due to blockage, effectively altering saltation patterns upwind of the instrumentation. Ideally, for the particular purpose of reliably mapping streamers, the measurement set-up should likely have an even smaller sensor spacing ($\leq 0.05\text{ m}$), which can only be achieved by using smaller and thinner sensors. In combination with a higher sampling frequency, this would allow for sufficient spatiotemporal resolution required in order to more easily discern between individual streamers and larger patterns, and to visually determine streamer length scales with less uncertainty. At the same time, a sufficient spatial resolution would also allow for application of the CWT technique to the spanwise record instead of the time series (similar to Ruessink et al. (2007), which could potentially help elucidate on the typical width of streamers. Furthermore, it would also be favourable if the instrument was more robust to high-intensity transport conditions, as the SDSs often suffered saturation symptoms (Table 3.2). Unfortunately, these high demands are likely to undermine the beneficial quality of being a budget solution. Perhaps salvation should be sought in the Lagrangian approach once more, as it already produced promising results in a study by Sherman et al. (2013), and should this be further explored and developed.

6 Conclusion

This study has provided several new insights and substantiated existing ideas regarding the properties and behaviour of aeolian sand streamers in a typical Dutch beach-dune system and how these depend on the transport conditions.

What streamer patterns and length scales occur under which transport conditions?

Spatiotemporal maps of saltation intensity have demonstrated the evolution of the streamer transport pattern at 0.1 m from the bed under intensifying transport conditions. From threshold transport conditions towards heavy transport conditions: (1) a scattered pattern of isolated low-intensity streamers, (2) more elongated streamers sometimes locally interlinked, (3) intensified version of the previous pattern partially underlain with a low-intensity saltation cloud, (4) high density of locally-interlinked, high-intensity streamers fully embedded in a moderate-intensity saltation cloud. Embedded streamers were found to have typical lengths of up to 0.5 m, widths of the order of 0.2 m, centre-to-centre spacings of up to 0.5 m and to occur at most every 0.4 m spanwise metre. Furthermore, streamers typically exhibit a head-tail structure, a relatively short steep frontal part followed by a much more gradual rear part, but which may smooth out under heavy transport conditions. Mainly due to this shape, the above length scales must be regarded a function of the observation height.

How are streamers related to the wind?

Aeolian streamers strongly respond to an increase in shear velocity, which may even approach a 4th-power-law relationship under (near-)equilibrium conditions. However, beyond the threshold shear velocity, which was found to be about 0.28 m s^{-1} under the most favourable conditions, the relationship becomes subject to a high degree of uncertainty. Streamer response lags approximately 0.5 s behind fluctuations in shear velocity on temporal scales of the order of 10 s and below, whereas they are practically in phase on temporal scales of minutes and above. The coupling between streamer intensity and horizontal wind speed was found strongest on temporal scales of the order of 10 s to minutes, which indicates that large-sized eddies with similar periods are best associated with streamers formation. Although a functional relationship between saltation intensity turbulence kinetic energy was not found, a threshold value of $0.5 \text{ m}^2 \text{ s}^{-2}$ established at temporal scales $\geq 10 \text{ s}$ could be indicative of a lower limit associated with the turbulent eddies.

How are streamers reflected in the spatiotemporal variability of the saltation system?

As the streamer pattern evolves under intensifying transport conditions, both temporal and spanwise intermittency are reduced, and it more and more closely resembles a steady, uniform saltation sheet. However, on a temporal scale of 10 min and

a spanwise scale of 3.1 m, lower bounds were found for relative temporal and spanwise variability of 47 % and 15 %, respectively, which are a reflection of the inherent turbulent nature of aeolian streamers. Relative spanwise variability shows to increase when considering greater spanwise scales, but stabilises somewhere beyond 3 m. Unlike shear velocity, wind gustiness was found to have no pronounced effect on the spanwise distribution of streamers and only slightly contribute to the temporal intermittency of streamer transport.

How do fetch and surface moisture content control streamer formation across the beach?

Fetch and surface moisture have important implications for the formation and continuation of streamers. Near the water line, tidal inundation periodically brings streamer formation to a complete halt by increasing the soil moisture content to well above the threshold moisture content. However, following the receding tide, surface drying may again quickly reduce surface moisture levels, enabling streamer formation to rapidly recover once an upwind below-threshold fetch of at least 10 m is provided. During low tide, streamer formation tends to be greatest on the mid beach and then reduce downwind due to the decreasing shear velocity as the result of deepening of the IBL and blockage by the foredune. This process continues up to a point high up the beach from where the fetch effect, possibly together with other factors, (over)compensates for the reduced shear velocity, which is reflected by more (intense) streamers being formed.

Recommendations

Future research should focus on quantifying the effective time reduction in sand transport caused by the variable streamer pattern for a range of different transport conditions in order to translate these findings into algorithms implementable in sediment transport models. A more Lagrangian-based approach could be instrumental for such purpose. Furthermore, this study did not assess streamer-pattern evolution as a function of more specific parameters such as surface moisture content, which might yield a different outcome than when solely based on the shear velocity.

A Supplementary figures

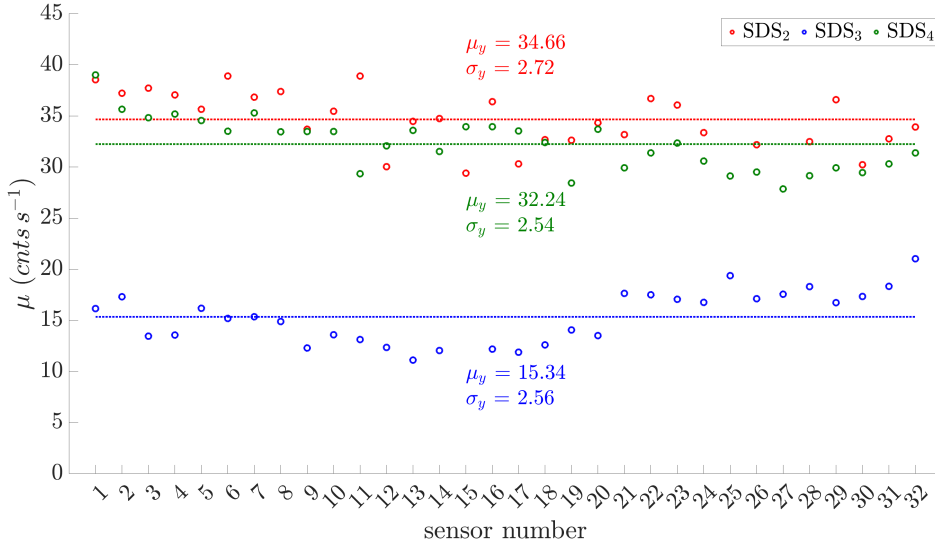


FIGURE A.1: Saltation intensity per sensor averaged over the entire data set. Also provided are the mean and standard deviation over all 32 sensors per SDS. Computations are based on 10-min temporal means. Measurement runs with only partially functioning impact sensors were excluded from the computation.

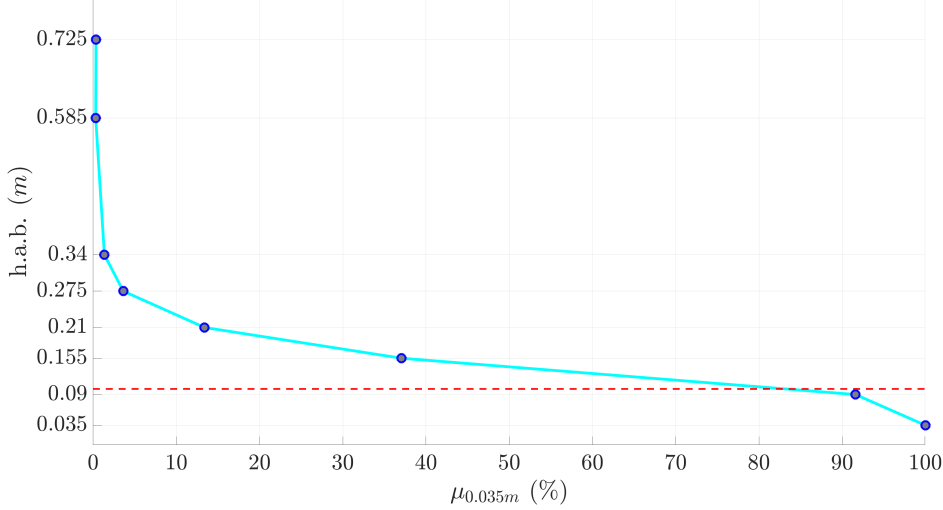


FIGURE A.2: Vertical saltation profile based on the mean saltation intensity (blue circles) measured by each impact sensor constituting the vertical array. The x -axis represents the percentage with respect to the mean saltation intensity measured at the lowest impact sensor. Red dashed line indicates the lower detection-height limit of the impact sensors constituting the horizontal array. Computations are based on 10-minute time averages of the whole data set.

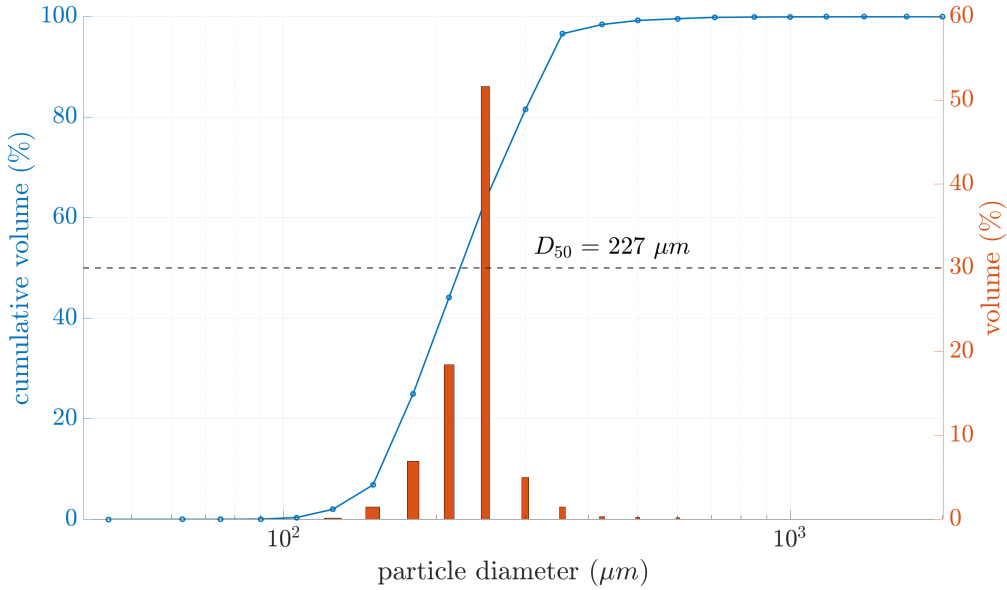


FIGURE A.3: Grain-size distribution based on grain samples taken across the beach from the low-water line to the dune foot on 11 October. Samples were first oven-dried and then sieved using a mechanical shaker, after which the various grain-size fractions were weighted. The mass-median diameter (D_{50}) is computed from the point where the fitted curve crosses the 50%-line.

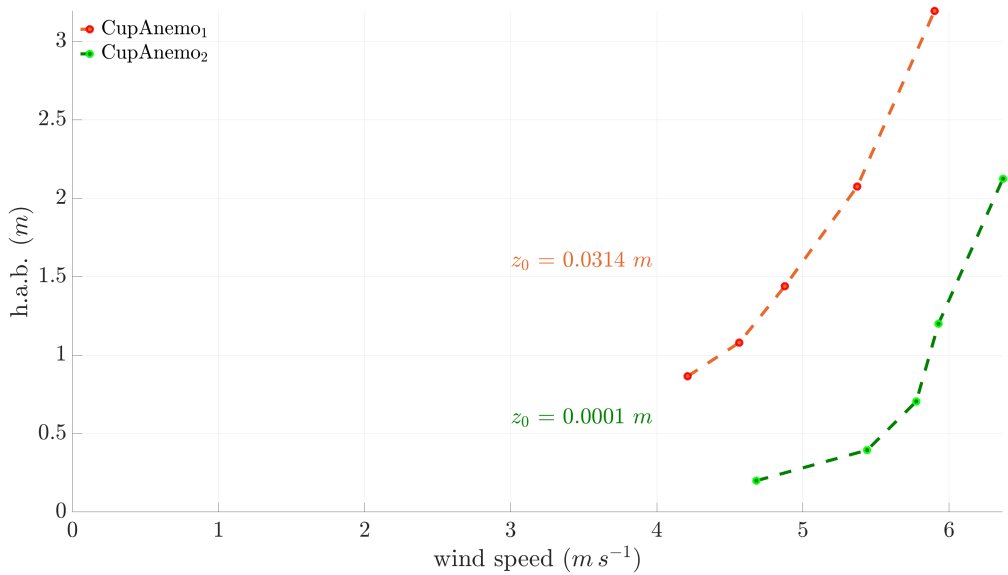


FIGURE A.4: Log wind profiles based on data collected by two on-site cup-anemometer towers. CupAnemo₁ was located close to the dune foot and had been full-time operational, whereas CupAnemo₂ stood on the foreshore and had to be removed and installed periodically because of the tide. Both set-ups measured at 1-min time intervals. Roughness lengths (z_0) were derived from the zero-velocity plane estimates using law-of-the-wall regressions.

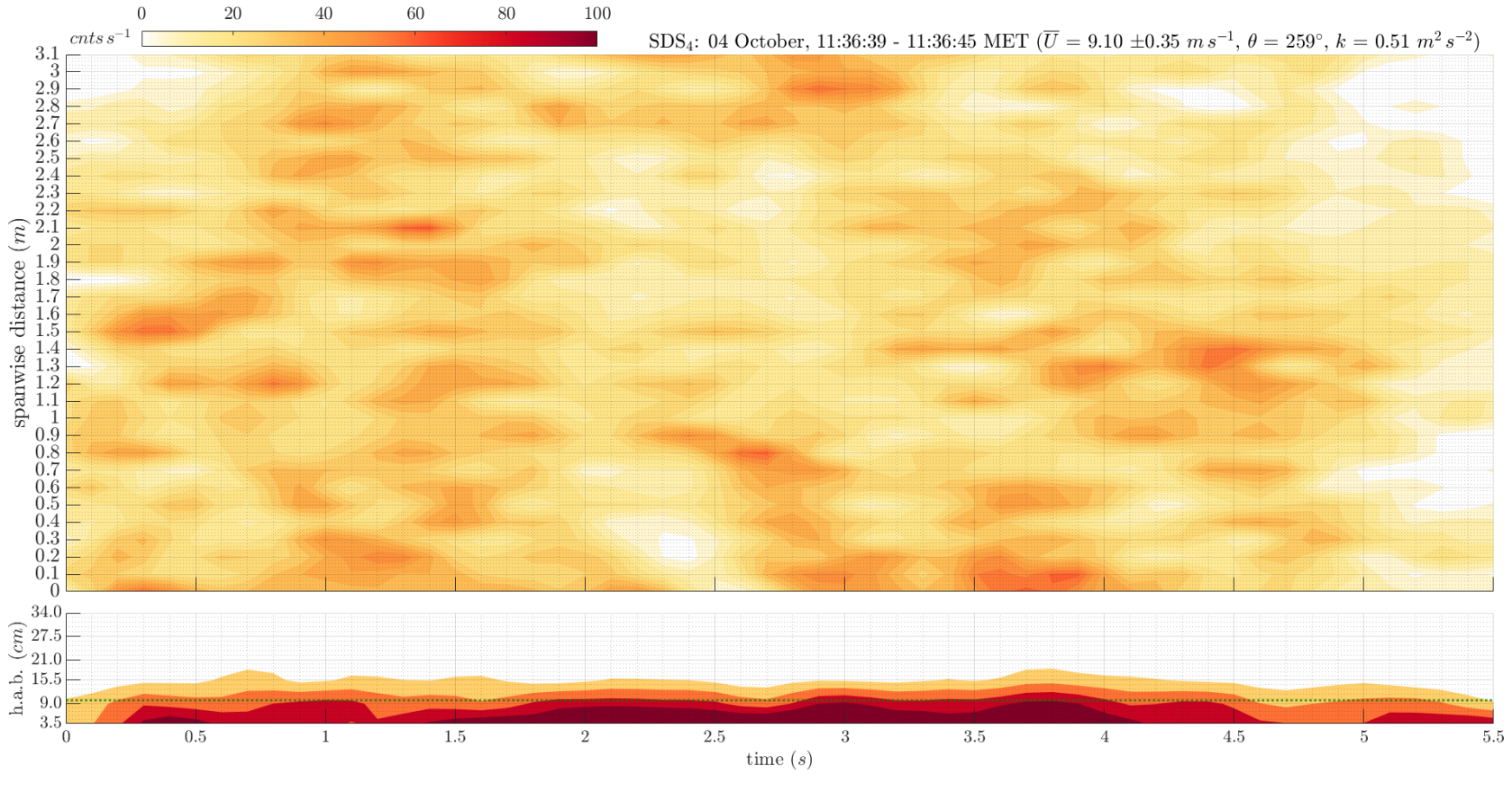


FIGURE A.5: Contour maps of saltation intensity as recorded by the (top) horizontal and (bottom) vertical sensor arrays of SDS₄. Maps have been smoothed using a Gaussian filter ($window = 5$) in the time domain. Horizontal green dotted line in the lower panel denotes the lower detection-height limit of the impact sensors of the horizontal array. Metadata and conditions regarding the considered time period are listed on top. Mean saltation values: $\mu = 24 \text{ cnts s}^{-1}$, $\sigma = 17 \text{ cnts s}^{-1}$ and $\sigma_y = 16 \text{ cnts s}^{-1}$. Note the difference in colour scaling compared to the other contour maps.

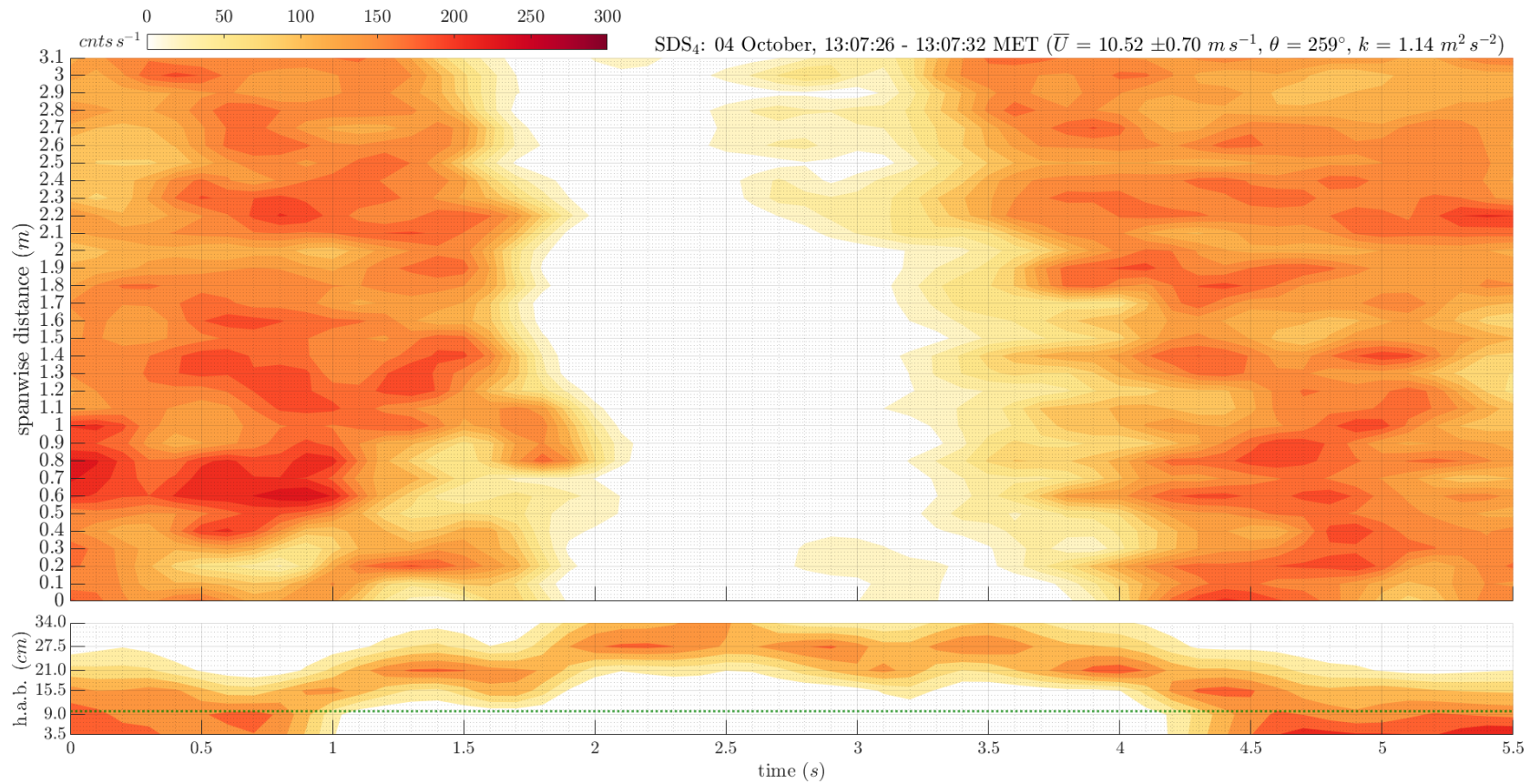


FIGURE A.6: Contour maps of saltation intensity as recorded by the (top) horizontal and (bottom) vertical sensor arrays of SDS4. Maps have been smoothed using a Gaussian filter (*window* = 5) in the time domain. Horizontal green dotted line in the lower panel denotes the lower detection-height limit of the impact sensors of the horizontal array. Metadata and conditions regarding the considered time period are listed on top. Note the temporal impact overload at all low-positioned sensors during the passage of an intense saltation cluster.

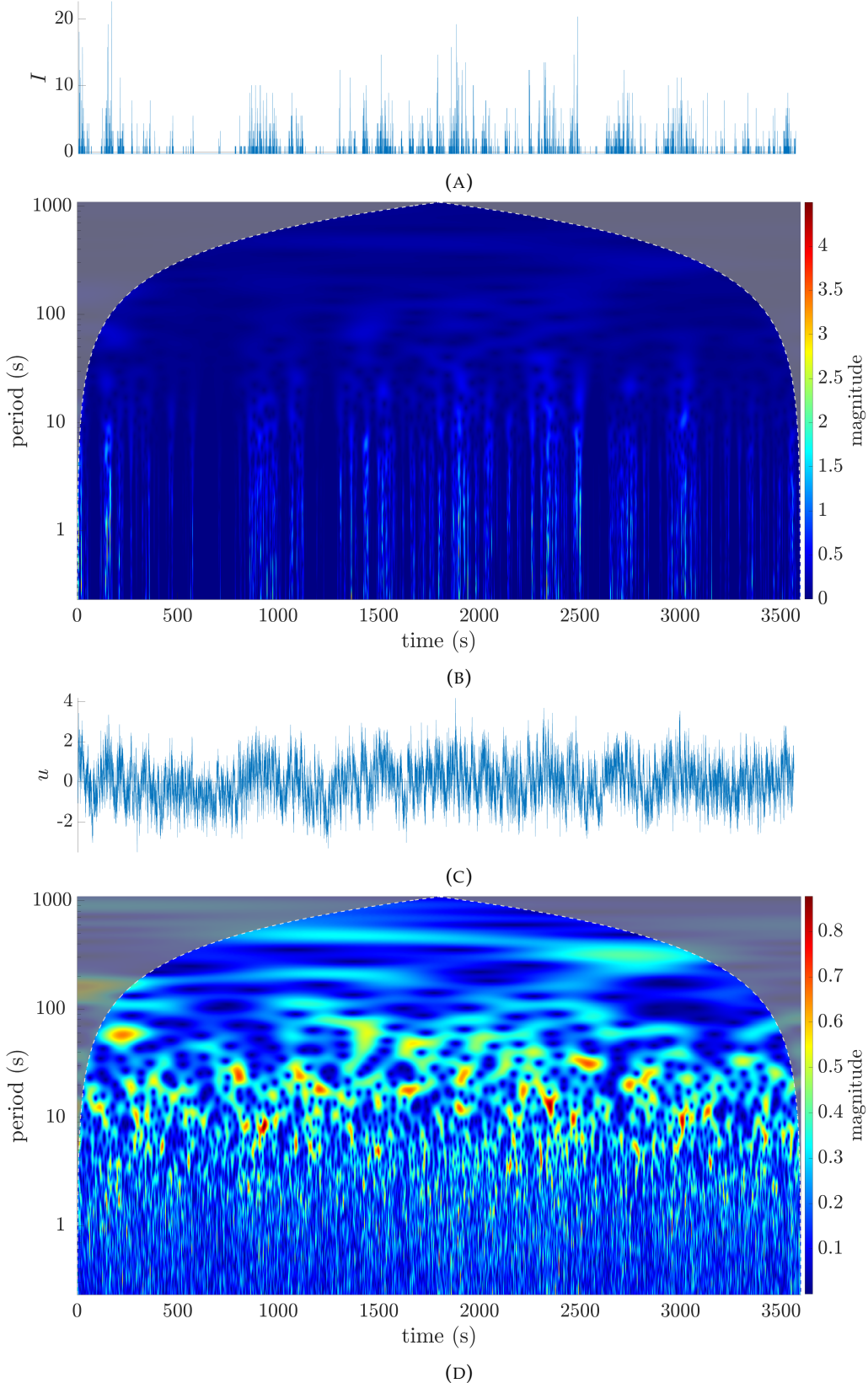


FIGURE A.7: Time series of normalised (A) saltation intensity and (B) horizontal wind speed, and respective CWT scalograms (B) and (D). Time period: 17 October from 13:23:08 to 14:23:08 MET. Mother: analytic Morse wavelet with $\gamma = 3$ and $P^2 = 60$. Instruments: SDS₃ and UA₃. Conditions: $\bar{u} = 5.71 \pm 0.67 \text{ m s}^{-1}$, $\theta = 231^\circ$, $k = 0.63 \text{ m}^2 \text{s}^{-2}$.

B Supplementary tables

TABLE B.1: The coefficient of correlation (R) and corresponding lag at which it is computed of spanwise-average saltation intensity (μ_y) and horizontal wind speed (u) for the three SDSs used. For this purpose the original (i.e., 10 Hz) data records were used. Note that on 25 October SDS₄ measured virtually no transport.

Day	Lag (s)	R (-)	Day	Lag (s)	R (-)	Day	Lag (s)	R (-)
11	0.3	0.96	11	0.0	0.87	4	0.6	0.40
17	0.0	0.42	17	0.4	0.49	5	0.5	0.62
20	0.3	0.85	20	2.2	0.82	6	0.4	0.66
25	0.4	0.19	22	0.6	0.51	11	4.7	0.67
27	0.6	0.60	24	0.6	0.89	25	-	-
			27	0.5	0.62	27	0.6	0.54
						29	0.4	0.86
						30	0.5	0.46

(A) SDS₂
(B) SDS₃
(C) SDS₄

TABLE B.2: The coefficient of correlation (R) and corresponding lag at which it is computed of saltation intensity ($\mu_{p=5:9}$) and instantaneous TKE (k) for the three SDSs used. Calculations only involved sensors 5 to 9, as typically these stood located closest to the SA. For this purpose the original (i.e., 10 Hz) data records were used. Note that on 25 October SDS₄ measured virtually no transport.

Day	Lag (s)	R (-)	Day	Lag (s)	R (-)	Day	Lag (s)	R (-)
11	0.3	0.66	11	0.4	0.63	4	0.7	0.30
17	0.4	0.34	17	0.4	0.42	5	2.5	0.49
20	4.8	0.52	20	-1.2	0.51	6	0.8	0.52
25	0.5	0.29	22	0.7	0.43	11	5.0	0.46
27	0.5	0.51	24	2.2	0.60	25	-	-
			27	0.5	0.54	27	0.5	0.48
						29	0.3	0.60
						30	0.5	0.61

(A) SDS₂
(B) SDS₃
(C) SDS₄

C Supplementary theory

C.1 Wavelet theory

For the purpose of signal analysis, when dealing with intermittent, aperiodic behaviour and non-Gaussian distributions, inherent in saltation events (Baas, 2006), the traditional Fourier transform generally falls short. Another technique that has quickly gained popularity over the past couple of decades is the so-called wavelet transform. This tool outperforms Fourier analysis in that it not only determines the dominant frequency components of a time series, but it also shows how these change over time (Torrence and Compo, 1998). In the process of decomposing a time series in time-frequency space (or rather time-scale space), however, one has to give up some resolution in the frequency domain according to Heisenberg's uncertainty principle (Grinsted, Moore, and Jevrejeva, 2004). In other words: a broader support of a signal in time comes at the expense of its support in frequency, and vice versa. Nonetheless, this method may still prove very useful to a wide variety of use cases, as will be further explored in this study.

C.1.1 Continuous wavelet transform

Similar to the Fourier transform, the continuous wavelet transform (CWT) computes inner products to reveal similarities between a signal and some analysing function. However, instead of using simple sinusoids that traditionally extend the full length of the signal, it utilises a series of scaled (either *contracted* or *dilated*) versions of a specific analysing (or *mother*) wavelet ψ , which are then each shifted (or *translated*) along the length of the signal in a stepwise fashion. This method has the major advantage that it also helps localising transients/discontinuities/singularities, information that would otherwise be lost when conducting a Fourier transform (The Mathworks Inc., 2019).

The CWT is essentially a convolution of the signal data with a set of functions generated by the mother wavelet and can be expressed as

$$C(a, b; f(t), \psi(t)) = \int_{-\infty}^{\infty} f(t) \frac{1}{a} \psi^* \left(\frac{t - b}{a} \right) dt \quad (\text{C.1})$$

where $a (> 0)$ and b are scale and translation parameters, respectively, and $*$ denotes the complex conjugate of ψ . A comparison routine, in which the values of the scale and translation parameters are varied continuously, yields the CWT coefficients $C(a, b)$. For convenience sake, their dependence on the signal and mother wavelet functions are, hereinafter, suppressed. The constituent wavelets of the original signal are obtained by multiplying each coefficient by the appropriately dilated and translated (i.e., daughter) wavelet (The Mathworks Inc., 2019).

Large values of $C(a, b)$ are produced close to abrupt changes in the signal under consideration. Such transients are best localised at smaller wavelet scales, for their smaller support in the time domain precludes large sets of wavelet coefficients from being affected by the anomaly.

A drawback of the CWT is that it is not an orthonormal transform, but rather a linearly dependent set (technical term: *frame*). A benefit, however, is that the CWT is shift-invariant, meaning that a shift in the input signal does not cause a significant realignment of signal energy in the CWT coefficients by scale.

C.1.2 Mother wavelet function

In essence, wavelets are brief oscillations that both start and end at zero with an average value of zero and a non-zero (vector) norm, and whose structure enables efficient computational algorithms. In time-frequency analysis the choice of mother (or *analysing*) wavelet function is not trivial, since it also significantly affects the CWT coefficients. Selection must be based on the signal feature of interest, for one wavelet may facilitate its detection much better than the other.

Generalised Morse wavelets, a family of exactly analytic wavelets (i.e., complex-valued with zero leakage to negative frequencies (Lilly and Olhede, 2009)), are particularly useful for analysing signals with time-varying amplitude and frequency (i.e., modulated signals). Moreover, they effectively encompass all other types of commonly used analytic wavelets because of their computational malleability (Lilly, 2017). In the frequency (or Fourier) domain the Morse wavelet can be expressed as

$$\Psi_{\beta,\gamma}(\omega) = U(\omega)a_{\beta,\gamma}\omega^{\beta}e^{-\omega^{\gamma}} \quad (\text{C.2})$$

where $U(\omega)$ is the Heaviside (or unit) step function and where

$$a_{\beta,\gamma} \equiv 2(e\gamma/\beta)^{\beta/\gamma} \quad (\text{C.3})$$

is a normalising constant (Lilly and Olhede, 2009), γ characterises the symmetry (or degree of deviation from Gaussianity) of the Morse wavelet and β functions as a decay or compactness parameter. In the time domain the Morse wavelet is expressed by the inverse Fourier transform:

$$\Psi_{\beta,\gamma}(t) = \frac{1}{2\pi} \int_0^\infty a_{\beta,\gamma}\omega^{\beta}e^{-\omega^{\gamma}}e^{i\omega t} d\omega \quad (\text{C.4})$$

The properties of the daughter Morse wavelet and subsequent behaviour of the transform depend on a combination of time-bandwidth product $P^2 = \beta\gamma$ and γ . In principle, the product P^2 determines the number of oscillations (fewer cycles = better temporal precision; more cycles = better frequency precision), while γ alone controls the shape (skewness) of the wavelet (Lilly and Olhede, 2012).

C.1.3 Wavelet coherence

There are two bivariate extensions of the previously discussed wavelet analysis technique. One of these is the cross-wavelet transform (XWT), which is defined as

$$C_{xy}(a, b) = S(C_x^*(a, b)C_y(a, b)) \quad (\text{C.5})$$

where the cross-wavelet coefficient $C_{xy}(a, b)$ serves as a measure of common power of the two signals, x and y , and $C_x(a, b)$ and $C_y(a, b)$ signify their CWT coefficients at scales a and translations b . Again, the superscript * denotes complex conjugation and S is a smoothing operator in time and scale, all of which is explained in more detail in Grinsted, Moore, and Jevrejeva (2004).

The other extension is the wavelet transform coherence (WTC), which enables characterisation of correlated behaviour in two non-stationary time series. The WTC is defined as

$$R^2(a, b) = \frac{|S(C_x^*(a, b) C_y(a, b))|^2}{S|C_x(a, b)|^2 S|C_y(a, b)|^2} \quad (\text{C.6})$$

where $R^2(a, b)$ is the magnitude-squared coherence. As its definition closely resembles that of the more familiar coefficient of determination, it may be regarded as a localised version of that in time-scale space (Chunying, Haifeng, and Lin, 2017).

It is important to be aware that common behaviour of two variables can be either explained by one variable controlling the other, or by some other mechanism affecting both variables simultaneously and similarly. This can be further examined by acquiring the coherence phase difference (CPD), which is computed as

$$\phi(a, b) = \tan^{-1} \left[\frac{\Im\{S(C_x^*(a, b) C_y(a, b))\}}{\Re\{S(C_x^*(a, b) C_y(a, b))\}} \right] \quad (\text{C.7})$$

where \Im and \Re denote the imaginary and real part, respectively (Ruessink et al., 2007). If the oscillations in the two time series indeed show phase-locked behaviour, that greatly supports the existence of a mutual cause-and-effect relationship (Grinsted, Moore, and Jevrejeva, 2004). Once some form of causality has been established between the variables under consideration, their local relative time lag can be inferred from the phase angles obtained from the complex-valued wavelet cross spectrum (The Mathworks Inc., 2019).

C.1.4 Cone of influence

Any of the above-mentioned analysis techniques utilising wavelets will inevitably encounter edge-effect artefacts. These artefacts result from the scaled wavelets extending beyond the length of the observed signal, consequently compromising the accuracy of the time-scale representation of the data. The term *cone of influence* (CoI) refers to the width (or duration) of the detection field of a scaled wavelet, which is larger for increasingly dilated versions (The Mathworks Inc., 2019).

Bibliography

- Anthony, E. J. (2008). *Shore Processes and their Palaeoenvironmental Applications*. Elsevier. DOI: [10.1016/s1572-5480\(08\)00417-x](https://doi.org/10.1016/s1572-5480(08)00417-x).
- Arens, S. M. (1996). "Rates of aeolian transport on a beach in a temperate humid climate". In: *Geomorphology* 17, pp. 3–18. ISSN: 0169555X. DOI: [10.1016/0169-555X\(95\)00089-N](https://doi.org/10.1016/0169-555X(95)00089-N).
- Baas, Andreas C. W. (2003). "The formation and behavior of aeolian streamers". PhD thesis. University of Southern California.
- (2004). "Evaluation of saltation flux impact responders (Safires) for measuring instantaneous aeolian sand transport intensity". In: *Geomorphology* 59.1-4, pp. 99–118. ISSN: 0169555X. DOI: [10.1016/j.geomorph.2003.09.009](https://doi.org/10.1016/j.geomorph.2003.09.009).
- (2006). "Wavelet power spectra of aeolian sand transport by boundary layer turbulence". In: *Geophysical Research Letters* 33.5, pp. 1–4. ISSN: 00948276. DOI: [10.1029/2005GL025547](https://doi.org/10.1029/2005GL025547).
- (2008). "Challenges in aeolian geomorphology: Investigating aeolian streamers". In: *Geomorphology* 93.1-2, pp. 3–16. ISSN: 0169555X. DOI: [10.1016/j.geomorph.2006.12.015](https://doi.org/10.1016/j.geomorph.2006.12.015).
- Baas, Andreas C. W. and Douglas. J. Sherman (2005). "Formation and behavior of aeolian streamers". In: *Journal of Geophysical Research: Earth Surface* 110.3, pp. 1–15. ISSN: 21699011. DOI: [10.1029/2004JF000270](https://doi.org/10.1029/2004JF000270).
- (2006). "Spatiotemporal Variability of Aeolian Sand Transport in a Coastal Dune Environment". In: *Journal of Coastal Research* 225, pp. 1198–1205. ISSN: 0749-0208. DOI: [10.2112/06-0002.1](https://doi.org/10.2112/06-0002.1). URL: <http://www.bioone.org/doi/abs/10.2112/06-0002.1>.
- Bagnold, R. A. (1936). "The Movement of Desert Sand". In: *Proceedings of the Royal Society A: Mathematical, Physical and Engineering Sciences* 157.892, pp. 594–620. ISSN: 1364-5021. DOI: [10.1098/rspa.1936.0218](https://doi.org/10.1098/rspa.1936.0218). URL: <http://rspa.royalsocietypublishing.org/cgi/doi/10.1098/rspa.1936.0218>.
- (1941). *The Physics of Blown Sand and Desert Dunes*. London: Methuen, p. 265.
- Barchyn, Thomas E. and Chris H. Hugenholtz (2010). "Field comparison of four piezoelectric sensors for detecting aeolian sediment transport". In: *Geomorphology* 120.3-4, pp. 368–371. ISSN: 0169555X. DOI: [10.1016/j.geomorph.2010.03.034](https://doi.org/10.1016/j.geomorph.2010.03.034). URL: <http://dx.doi.org/10.1016/j.geomorph.2010.03.034>.
- Bauer, B. O. and R. G. D. Davidson-Arnott (2003). "A general framework for modeling sediment supply to coastal dunes including wind angle, beach geometry, and fetch effects". In: *Geomorphology* 49.1, pp. 89–108. ISSN: 0169555X. DOI: [10.1016/S0169-555X\(02\)00165-4](https://doi.org/10.1016/S0169-555X(02)00165-4).
- Bauer, B. O. et al. (1990). "Aeolian transport measurement and prediction across a beach and dune at Castroville, California". In: *Coastal Dunes, Form and Process*. John Wiley, Chichester, pp. 39–55. ISBN: 0-471-91842-3.
- Bauer, B. O. et al. (1998). "Event detection and conditional averaging in unsteady aeolian systems". In: *Journal of Arid Environments* 39.3, pp. 345–375. ISSN: 01401963. DOI: [10.1006/jare.1998.0380](https://doi.org/10.1006/jare.1998.0380).

- Bauer, B. O. et al. (2009). "Aeolian sediment transport on a beach: Surface moisture, wind fetch, and mean transport". In: *Geomorphology* 105.1-2, pp. 106–116. ISSN: 0169555X. DOI: [10.1016/j.geomorph.2008.02.016](https://doi.org/10.1016/j.geomorph.2008.02.016). URL: <http://dx.doi.org/10.1016/j.geomorph.2008.02.016>.
- Bauer, B. O. et al. (2013). "Critical Reflections on the Coherent Flow Structures Paradigm in Aeolian Geomorphology". In: *Coherent Flow Structures at Earth's Surface*. Ed. by Jeremy G. Venditti et al. 1st ed. 1. John Wiley & Sons, Ltd, pp. 111–134.
- Boxel, J. H. van, G. Sterk, and S. M. Arens (2004). "Sonic anemometers in aeolian sediment transport research". In: *Geomorphology* 59.1-4, pp. 131–147. ISSN: 0169555X. DOI: [10.1016/j.geomorph.2003.09.011](https://doi.org/10.1016/j.geomorph.2003.09.011).
- Butterfield, G. R. (1993). "Sand transport response to fluctuating wind velocity". In: *Turbulence: perspectives on flow and sediment transfer*.
- Chapman, Connie A. et al. (2012). "Turbulent Reynolds stress and quadrant event activity in wind flow over a coastal foredune". In: *Geomorphology* 151-152, pp. 1–12. ISSN: 0169555X. DOI: [10.1016/j.geomorph.2011.11.015](https://doi.org/10.1016/j.geomorph.2011.11.015). URL: <http://dx.doi.org/10.1016/j.geomorph.2011.11.015>.
- Cepil, W. S. (1957). "Width of field strips to control wind erosion". In: — (1958). *Soil Conditions That Influence Wind Erosion*. Vol. 1185. US Dept. of Agriculture, p. 40. ISBN: 3663537137.
- Chunying, Fang, Li Haifeng, and Ma Lin (2017). "The research of constructing dynamic cognition model based on brain network". In: *Saudi Journal of Biological Sciences* 24.3, pp. 548–555. ISSN: 1319562X. DOI: [10.1016/j.sjbs.2017.01.025](https://doi.org/10.1016/j.sjbs.2017.01.025). URL: <http://dx.doi.org/10.1016/j.sjbs.2017.01.025>.
- Davidson-Arnott, R. G. D. and B. O. Bauer (2009). "Aeolian sediment transport on a beach: Thresholds, intermittency, and high frequency variability". In: *Geomorphology* 105.1-2, pp. 117–126. ISSN: 0169555X. DOI: [10.1016/j.geomorph.2008.02.018](https://doi.org/10.1016/j.geomorph.2008.02.018). URL: <http://dx.doi.org/10.1016/j.geomorph.2008.02.018>.
- Davidson-Arnott, R.G.D. et al. (2005). "Moisture and fetch effects on aeolian sediment transport rates during a fall storm, Greenwich Dunes, Prince Edward Island". In:
- De Vries, S. et al. (2014). "Aeolian sediment transport in supply limited situations". In: *Aeolian Research* 12, pp. 75–85. ISSN: 18759637. DOI: [10.1016/j.aeolia.2013.11.005](https://doi.org/10.1016/j.aeolia.2013.11.005). URL: <http://dx.doi.org/10.1016/j.aeolia.2013.11.005>.
- Delgado-Fernandez, Irene (2010). "A review of the application of the fetch effect to modelling sand supply to coastal foredunes". In: *Aeolian Research* 2.2-3, pp. 61–70. ISSN: 18759637. DOI: [10.1016/j.aeolia.2010.04.001](https://doi.org/10.1016/j.aeolia.2010.04.001). URL: <http://dx.doi.org/10.1016/j.aeolia.2010.04.001>.
- Delgado-Fernandez, Irene and R. G. D. Davidson-Arnott (2011). "Meso-scale aeolian sediment input to coastal dunes: The nature of aeolian transport events". In: *Geomorphology* 126.1-2, pp. 217–232. ISSN: 0169555X. DOI: [10.1016/j.geomorph.2010.11.005](https://doi.org/10.1016/j.geomorph.2010.11.005). URL: <http://dx.doi.org/10.1016/j.geomorph.2010.11.005>.
- Donker, Jasper, Marcel van Maarseveen, and Gerben Ruessink (2018). "Spatio-temporal variations in foredune dynamics determined with Mobile Laser Scanning". In: *Journal of Marine Science and Engineering* 6.4. ISSN: 20771312. DOI: [10.3390/jmse6040126](https://doi.org/10.3390/jmse6040126).
- Ellis, J. T. and D. J. Sherman (2013). "Fundamentals of Aeolian Sediment Transport: Wind-Blown Sand". In: *Treatise on Geomorphology* 11.March, pp. 85–108. DOI: [10.1016/B978-0-12-374739-6.00299-2](https://doi.org/10.1016/B978-0-12-374739-6.00299-2).
- Ellis, Jean T. et al. (2012). "Temporal and spatial variability of aeolian sand transport: Implications for field measurements". In: *Aeolian Research* 3.4, pp. 379–387. ISSN: 18759637. DOI: [10.1016/j.aeolia.2011.06.001](https://doi.org/10.1016/j.aeolia.2011.06.001). URL: <http://dx.doi.org/10.1016/j.aeolia.2011.06.001>.

- Erpul, G., L. D. Norton, and D. Gabriels (2002). "Raindrop-induced and wind-driven soil particle transport". In: *Catena* 47.3, pp. 227–243. ISSN: 03418162. DOI: [10.1016/S0341-8162\(01\)00182-5](https://doi.org/10.1016/S0341-8162(01)00182-5).
- Gares, P. A. et al. (1996). "Alongshore variations in aeolian sediment transport: Carrick Finn Strand, Ireland". In: *Journal of Coastal Research* 12.3, pp. 673–682. ISSN: 07490208. DOI: [10.12795/revistafuentes](https://doi.org/10.12795/revistafuentes).
- Garratt, J. R. (1990). "The internal boundary layer - A review". In: *Boundary-Layer Meteorology* 50.1-4, pp. 171–203. ISSN: 00068314. DOI: [10.1007/BF00120524](https://doi.org/10.1007/BF00120524).
- Gillette, Dale A., Ellen Hardebeck, and Jim Parker (1997). "Large-scale variability of wind erosion mass flux rates at Owens Lake: 2. Role of roughness change, particle limitation, change of threshold friction velocity, and the Owen effect". In: *Journal of Geophysical Research* 102.D22, p. 25989. ISSN: 0148-0227. DOI: [10.1029/97jd00960](https://doi.org/10.1029/97jd00960).
- Gillette, Dale A. and Theodore R. Walker (1977). "Characteristics of airborne particles produced by wind erosion of sandy soil, high plains of west Texas". In: *Soil Science*. ISSN: 15389243. DOI: [10.1097/00010694-197702000-00004](https://doi.org/10.1097/00010694-197702000-00004).
- Gillette, Dale A. et al. (1996). "Causes of the fetch effect in wind erosion". In: *Earth Surface Processes and Landforms* 21.7, pp. 641–659. ISSN: 01979337. DOI: [10.1002/\(SICI\)1096-9837\(199607\)21:7<641::AID-ESP662>3.0.CO;2-9](https://doi.org/10.1002/(SICI)1096-9837(199607)21:7<641::AID-ESP662>3.0.CO;2-9).
- Grinsted, A., J. C. Moore, and S. Jevrejeva (2004). "Application of the cross wavelet transform and wavelet coherence to geophysical time series". In: *Nonlinear Processes in Geophysics* 11.5/6, pp. 561–566. ISSN: 1607-7946. DOI: [10.5194/npg-11-561-2004](https://doi.org/10.5194/npg-11-561-2004). URL: <http://www.nonlin-processes-geophys.net/11/561/2004/>.
- Hage, Pam, Gerben Ruessink, and Jasper Donker (2018). "Using argus video monitoring to determine limiting factors of aeolian sand transport on a narrow beach". In: *Journal of Marine Science and Engineering* 6.4. ISSN: 20771312. DOI: [10.3390/jmse6040138](https://doi.org/10.3390/jmse6040138).
- Hinze, J.O. (1975). *Turbulence*. 2nd. New York: NY: McGraw-Hill.
- Hsu, Shih-Ang (1971). "Measurement of Shear Stress and Roughness Length on a Beach". In: *Journal of Geophysical Research April* 76.20, pp. 2880–2885. ISSN: 01480227. DOI: [10.1029/JC076i012p02880](https://doi.org/10.1029/JC076i012p02880). URL: <https://agupubs.onlinelibrary.wiley.com/doi/pdf/10.1029/JC076i012p02880>.
- Hunt, J. C. R. and P. Carlotti (2001). "Statistical structure at the wall of the high reynolds number turbulent boundary layer". In: *Flow, Turbulence and Combustion* 66.4, pp. 453–475. ISSN: 13866184. DOI: [10.1023/A:1013519021030](https://doi.org/10.1023/A:1013519021030).
- Hunt, J. C. R. and J. F. Morrison (2000). "Eddy structure in turbulent boundary layers". In: *European Journal Of Mechanics B-Fluids* 19, pp. 673–694. ISSN: 09977546. DOI: [10.1016/S0997-7546\(00\)00129-1](https://doi.org/10.1016/S0997-7546(00)00129-1). URL: papers2://publication/uuid/04B24B61-B672-4452-8831-72055DDA8342.
- Kabat, Pavel et al. (2009). "Dutch coasts in transition". In: *Nature Geoscience* 2.7, pp. 450–452. ISSN: 1752-0894. DOI: [10.1038/ngeo572](https://doi.org/10.1038/ngeo572). URL: <http://www.nature.com/doifinder/10.1038/ngeo572>.
- Kaimal, J. C. and J. J. Finnigan (1994). *Atmospheric boundary layer flows: their structure and measurement*. Oxford university press.
- Kok, Jasper F. et al. (2012). "The physics of wind-blown sand and dust". In: *Reports on Progress in Physics* 75.10. ISSN: 00344885. DOI: [10.1088/0034-4885/75/10/106901](https://doi.org/10.1088/0034-4885/75/10/106901).
- Leenders, J. K., J. H. van Boxel, and G. Sterk (2005). "Wind forces and related saltation transport". In: *Geomorphology* 71.3-4, pp. 357–372. ISSN: 0169555X. DOI: [10.1016/j.geomorph.2005.04.008](https://doi.org/10.1016/j.geomorph.2005.04.008).

- Lilly, Jonathan M. (2017). "Element analysis: A wavelet-based method for analysing time-localized events in noisy time series". In: *Proceedings of the Royal Society A: Mathematical, Physical and Engineering Sciences* 473.2200. ISSN: 14712946. DOI: [10.1098/rspa.2016.0776](https://doi.org/10.1098/rspa.2016.0776). URL: <https://dx.doi.org/10.6084/m9.figshare.c.3741266>.
- Lilly, Jonathan M. and Sofia C. Olhede (2009). "Higher-order properties of analytic wavelets". In: *IEEE Transactions on Signal Processing* 57.1, pp. 146–160. ISSN: 1053587X. DOI: [10.1109/TSP.2008.2007607](https://doi.org/10.1109/TSP.2008.2007607).
- (2012). "Generalized morse wavelets as a superfamily of analytic wavelets". In: *IEEE Transactions on Signal Processing* 60.11, pp. 6036–6041. ISSN: 1053587X. DOI: [10.1109/TSP.2012.2210890](https://doi.org/10.1109/TSP.2012.2210890).
- Livingstone, I. and A. Warren, eds. (2019). *Aeolian Geomorphology: A New Introduction*. John Wiley & Sons, Ltd.
- Luijendijk, Arjen P. et al. (2017). "The initial morphological response of the Sand Engine: A process-based modelling study". In: *Coastal Engineering* 119.July 2011, pp. 1–14. ISSN: 03783839. DOI: [10.1016/j.coastaleng.2016.09.005](https://doi.org/10.1016/j.coastaleng.2016.09.005). URL: <http://dx.doi.org/10.1016/j.coastaleng.2016.09.005>.
- Mayaud, Jerome R. et al. (2017). "Modelling aeolian sand transport using a dynamic mass balancing approach". In: *Geomorphology* 280, pp. 108–121. ISSN: 0169555X. DOI: [10.1016/j.geomorph.2016.12.006](https://doi.org/10.1016/j.geomorph.2016.12.006). URL: <http://dx.doi.org/10.1016/j.geomorph.2016.12.006>.
- Mogeng, M. L. et al. (2018). "Recovery of a turbulent boundary layer following a rough-to-smooth step-change in the wall condition". In: *Proceedings of the 21st Australasian Fluid Mechanics Conference, AFMC 2018* December, pp. 2–5.
- Panofsky, H. A. and J. A. Dutton (1984). "Atmospheric Turbulence: Models and Methods for Engineering Applications". New York.
- Ruessink, B. G. et al. (2007). "Coupled and noncoupled behavior of three-dimensional morphological patterns in a double sandbar system". In: *Journal of Geophysical Research: Oceans* 112.7, pp. 1–11. ISSN: 21699291. DOI: [10.1029/2006JC003799](https://doi.org/10.1029/2006JC003799).
- Schlichting, Hermann and Klaus Gersten (2017). *Boundary-Layer Theory*. 9. ISBN: 978-3-662-52919-5. DOI: [10.1007/978-3-662-52919-5](https://doi.org/10.1007/978-3-662-52919-5). URL: <http://linkinghub.elsevier.com/retrieve/pii/S0997754600011018>.
- Schönenfeldt, Hans Jürgen and Sibylle von Löwisch (2003). "Turbulence-driven saltation in the atmospheric surface layer". In: *Meteorologische Zeitschrift* 12.5, pp. 257–268. ISSN: 09412948. DOI: [10.1127/0941-2948/2003/0012-0257](https://doi.org/10.1127/0941-2948/2003/0012-0257).
- Sherman, Douglas J. (1992). "An equilibrium relationship for shear velocity and apparent roughness lenght in aeolian saltation". In: *Geomorphology* 5.3-5, pp. 419–431.
- Sherman, Douglas J. et al. (2011). "Measuring Aeolian Saltation: A Comparison of Sensors". In: *Journal of Coastal Research* 59, pp. 280–290. ISSN: 0749-0208. DOI: [10.2112/SI59-030.1](https://doi.org/10.2112/SI59-030.1). URL: <http://www.bioone.org/doi/abs/10.2112/SI59-030.1>.
- Sherman, Douglas J. et al. (2013). "Characterization of aeolian streamers using time-average videography". In: *Journal of Coastal Research* 165.April, pp. 1331–1336. ISSN: 0749-0208. DOI: [10.2112/SI65-225.1](https://doi.org/10.2112/SI65-225.1). URL: <http://www.bioone.org/doi/10.2112/SI65-225.1>.
- Smits, Alexander J. and Ivan Marusic (2013). "Wall-bounded turbulence". In: *Physics Today* 66.9, pp. 25–30. ISSN: 00319228. DOI: [10.1063/PT.3.2114](https://doi.org/10.1063/PT.3.2114).
- Spies, Peter Jost, Ian K. McEwan, and Graeme R. Butterfield (2000). "One-dimensional transitional behaviour in saltation". In: *Earth Surface Processes and Landforms*. ISSN:

01979337. DOI: [10.1002/\(SICI\)1096-9837\(200005\)25:5<505::AID-ESP78>3.0.CO;2-D](https://doi.org/10.1002/(SICI)1096-9837(200005)25:5<505::AID-ESP78>3.0.CO;2-D).
- Sterk, G., A. F.G. Jacobs, and J. H. Van Boxel (1998). "The effect of turbulent flow structures on saltation sand transport in the atmospheric boundary layer". In: *Earth Surface Processes and Landforms* 23.10, pp. 877–887. ISSN: 01979337. DOI: [10.1002/\(SICI\)1096-9837\(199810\)23:10<877::AID-ESP905>3.0.CO;2-R](https://doi.org/10.1002/(SICI)1096-9837(199810)23:10<877::AID-ESP905>3.0.CO;2-R).
- Stout, J. E. and T. M. Zobeck (1997). "Intermittent saltation". In: *Sedimentology* 44.5, pp. 959–970. ISSN: 00370746. DOI: [10.1046/j.1365-3091.1997.d01-55.x](https://doi.org/10.1046/j.1365-3091.1997.d01-55.x).
- Stull, R. B. (1988). "An introduction to boundary layer meteorology". In: *An introduction to boundary layer meteorology*. DOI: [10.1007/978-94-009-3027-8](https://doi.org/10.1007/978-94-009-3027-8).
- Taylor, G. I. (1938). "The Spectrum of Turbulence". In: *Proceedings of the Royal Society of London. Series A, Mathematical and Physical Sciences* 164.919, pp. 476–490. URL: <https://www.jstor.org/stable/97077>.
- The Mathworks Inc. (2019). *MATLAB - MathWorks*. URL: <https://nl.mathworks.com/help/wavelet/gs/continuous-and-discrete-wavelet-transforms.html>.
- Torrence, Christopher and Gilbert P. Compo (1998). *A Practical Guide to Wavelet Analysis*. Tech. rep. 1. Boulder, Colorado: University of Colorado, pp. 61–78.
- Tuijnman, J. T. (2018). *Soil Moisture Dynamics and the Effects on Initiation of Aeolian Sand Transport (MSc thesis)*.
- Van Dijk, P. M., L. Stroosnijder, and J. L. M. P. De Lima (1996). "The influence of rainfall on transport of beach sand by wind". In: *Earth Surface Processes and Landforms* 21.4, pp. 341–352. ISSN: 01979337. DOI: [10.1002/\(SICI\)1096-9837\(199604\)21:4<341::AID-ESP542>3.0.CO;2-Z](https://doi.org/10.1002/(SICI)1096-9837(199604)21:4<341::AID-ESP542>3.0.CO;2-Z).
- Wallace, James M. (2016). "Quadrant Analysis in Turbulence Research: History and Evolution". In: *Annual Review of Fluid Mechanics* 48.1, pp. 131–158. ISSN: 0066-4189. DOI: [10.1146/annurev-fluid-122414-034550](https://doi.org/10.1146/annurev-fluid-122414-034550).
- Wang, Ping et al. (2019). "The Scale Characteristics and Formation Mechanism of Aeolian Sand Streamers Based on Large Eddy Simulation". In: *Journal of Geophysical Research: Atmospheres* 124.21, pp. 11372–11388. ISSN: 21698996. DOI: [10.1029/2019JD031081](https://doi.org/10.1029/2019JD031081).
- Wiggs, G. F.S. and C. M. Weaver (2012). "Turbulent flow structures and aeolian sediment transport over a barchan sand dune". In: *Geophysical Research Letters* 39.5, pp. 1–7. ISSN: 00948276. DOI: [10.1029/2012GL050847](https://doi.org/10.1029/2012GL050847).
- Winter, R. C. de, F. Gongrip, and B. G. Ruessink (2015). "Observations and modeling of alongshore variability in dune erosion at Egmond aan Zee, the Netherlands". In: *Coastal Engineering* 99, pp. 167–175. ISSN: 03783839. DOI: [10.1016/j.coastaleng.2015.02.005](https://doi.org/10.1016/j.coastaleng.2015.02.005). URL: <http://dx.doi.org/10.1016/j.coastaleng.2015.02.005>.
- Winter, W. de et al. (2018). "Measuring high spatiotemporal variability in saltation intensity using a low-cost Saltation Detection System: Wind tunnel and field experiments". In: *Aeolian Research* 31.February 2017, pp. 72–81. ISSN: 18759637. DOI: [10.1016/j.aeolia.2017.11.003](https://doi.org/10.1016/j.aeolia.2017.11.003). URL: <https://doi.org/10.1016/j.aeolia.2017.11.003>.
- Winter, Winnie de et al. (2020). "Regional versus local wind speed and direction at a narrow beach with a high and steep foredune". In: *PLoS ONE* 15.1, pp. 1–19. ISSN: 19326203. DOI: [10.1371/journal.pone.0226983](https://doi.org/10.1371/journal.pone.0226983). URL: <http://dx.doi.org/10.1371/journal.pone.0226983>.
- Wyngaard, John C. (1992). "Atmospheric Turbulence". In: *Annual Review of Fluid Mechanics* 24.1, pp. 205–234.